

Multi-wavelength Studies of Active Galactic Nuclei

A

THESIS SUBMITTED

To

PT. RAVISHANKAR SHUKLA UNIVERSITY RAIPUR

FOR

THE DEGREE OF DOCTOR OF PHILOSOPHY

IN

PHYSICS

UNDER THE FACULTY OF SCIENCE

MARCH 2016

INVESTIGATOR:

Jai Bhagwan

ARIES, MANORA PEAK

NAINITAL-263002

SUPERVISOR:

Dr. Alok C. Gupta

SCIENTIST-E

ARIES, Nainital

RESEARCH CENTER

ARYABHATTA RESEARCH INSTITUTE OF OBSERVATIONAL SCIENCES (ARIES)

MANORA PEAK, NAINITAL-263002, INDIA

Declaration by Candidate

I, declare that this thesis entitled ‘ ‘Multi-wavelength Studies of Active Galactic Nuclei" is my own work conducted under the supervision of Dr. Alok C. Gupta at Aryabhata Research Institute of observational sciences (ARIES), Nainital, Uttarakhand, India, approved by the Research Degree Committee. I have put in more than 200 days of attendance with the supervisor at the center.

I further declare that to the best of my knowledge the thesis does not contain any part of any work, which has been submitted for the award of any degree either in this University or in any other University/Deemed university without proper citation.

Dr. Alok C. Gupta

Signature of the Supervisor

Jai Bhagwan

Signature of the Candidate

Signature of the Chairman, DRC

Certificate by the Supervisor

This is to certify that the work entitled ‘‘Multi-wavelength Studies of Active Galactic Nuclei’’ is a piece of research work done by Mr. Jai Bhagwan under my guidance and supervision for the degree of Doctor of Philosophy in PHYSICS of Pt. Ravishankar Shukla University, Raipur (Chhattisgarh), India. That the candidate has put in an attendance of more than 200 days with me.

To the best of my knowledge and belief this thesis

1. Embodies the work of the candidate himself.
2. Has duly been completed.
3. Fulfills the requirements of the Ordinance relating to the Ph.D. degree of the University;
and
4. Is up to the standard both in respect of contents and language for being referred to the examiner.

Dr. Alok C. Gupta
Signature of the Supervisor

Forwarded

Signature of Chairman, DRC

Copy Right Transfer Approval Form

APPENDIX - 5

Copy Right Transfer Approval Form (Clause 14e of the Ordinance - 45)

Name of the Candidate: Jai Bhagwan
Department: School of Studies in Physics and Astrophysics
Degree : Doctor of Philosophy in Physics
University: Pt. Ravishankar Shukla University, Raipur
Supervisor: Dr. Alok C. Gupta
Thesis Title: Multi-wavelength Studies of Active Galactic Nuclei
Year of Award:

Agreement

1. I hereby declare that, if appropriate, I have obtained and attended hereto a written permission/statement from owner(s) of each third party copyrighted matter to be included in my thesis/dissertation, allowing distribution as specified below.
2. I hereby grant to the university and its agents the non-exclusive license to archive and make accessible, under the condition specified below, my thesis/dissertation, in whole or in part in all forms of media, now or hereafter known. I retain all other ownership rights to the copyright of the thesis/dissertation. I and my Supervisor, also retain the right to use in future works (such as articles or books) all or part of this thesis, dissertation, or project report.

Condition:

1. Release the entire work for access worldwide

Signature of the Candidate

Signature and Seal of the Supervisor

Place

Date

To

My Parents

(Mrs. Kamla Devi & Mr. Jagdish Chander)

and

All My Teachers

Astronomy is useful because it raises us above ourselves; it is useful because it is grand. It shows us how small is man's body, how great his mind, since his intelligence can embrace the whole of this dazzling immensity, where his body is only an obscure point, and enjoy its silent harmony.

Henri Poincare

Acknowledgements

My tenure as a Ph. D. student in the Arayabhatta Research Institute of of observational sciencES (ARIES) at Nainital has been a truly wonderful experience. I met some of the most amazing and intelligent people, and made some good friends. The dissertation work that I have done here would not be possible without the love and support of a myriad of people, and I am thankful of nature which provide me an opportunity to highlight their contributions.

First and foremost, I would like to thank my supervisor, Dr. Alok C. Gupta. It would be impossible to express, here or anywhere, the depth of my gratitude to him for all his support, his guidance, his encouragement, and his patience. He is an excellen scientist and a model supervisor, and it has been my great honour and privilege to be his student.

I would like to express my gratitude to Prof. Iossif Papadakis whose help as an unofficial “Co-supervisor” has consistently provided me thoughtful and interesting feedback and guidance, and who has helped me in shaping this work in important ways. I am thankful to Prof. Paul J. Wiita, Ms. Aditi Agarwal, Ms. Nibedita Kalita, and Dr. Haritma Gaur for collaborative work and scientific discussions. I am also very much thankful to Profs. A. Strigachev, R. Bachev, E. Semkov, G. Damljanovic, and O. Vince for doing extensive optical observations for the work presented in this dissertation.

I am grateful to ARIES former Director Prof. Ram Sagar, present Acting director Dr. Wahab Uddin for providing me the facilities of the Institute. I would like to thank Prof. S.K. Pandey, Vice Chancellor and Prof. R.N. Baghel, Head, School of Studies in Physics and Astrophysics, Pt. Ravishankar Shukla University, Raipur, India for their support during my thesis work. I am fortunate to have a wonderful group of friends (Rajesh, Ramkesh, Brajesh, Ravi, Krishana, Raman) at ARIES, and I want to thank them all for making my Ph. D. world exciting and rich. My special Thanks to ARIES Scientists Dr. J.C. Pandey and Dr. N. Singh for their valuable help and suggestions. I thankfully acknowledge all scientists, staff members and students in ARIES for their support.

Most importantly, thank you to my parents Mr. Jagdish Chander and Mrs. Kamla Devi. It is hard for me to express how much their tireless, selfless support, affection, and encouragement have sustained me throughout my whole career. They were always there to share my success or defeat with me, give me words of wisdom and advice.

And, of course, thank you to my wife, Sarita. We got married last year, and there was never a day that went by in between that I did not think myself the luckiest man in the world to have her as my life partner and best friend. Her love, tireless patience, and encouragement sustained and enriched me.

Jai Bhagwan

LIST OF PUBLICATIONS

Thesis Related Papers:

- Spectral energy distributions of the BL Lac PKS 2155–304 from XMM-Newton.
Jai Bhagwan, Alok C. Gupta, I.E. Papadakis and Paul J. Wiita
Monthly Notices of the Royal Astronomical Society, **444**, 3647–3656,
(2014)
- Flux and spectral variability of the blazar PKS 2155–304 with XMM-Newton:
Evidence of particle acceleration and synchrotron cooling.
Jai Bhagwan, Alok C. Gupta, I.E. Papadakis and Paul J. Wiita
New Astronomy, **44**, 21–28 (2016).
- Multi-band optical variability of three TeV Blazars on Diverse Timescales.
Alok C. Gupta, A. Agarwal, **Jai Bhagwan**, A. Strigachev, R. Bachev, E. Semkov,
H. Gaur , G. Damjanovic, O. Vince, Paul J. Wiita
Monthly Notices of the Royal Astronomical Society (DOI: 10.1093/mnras/stw377), (2016) (in press) ([arXiv:1602.04200](https://arxiv.org/abs/1602.04200)).

Other Papers in Refereed Journals:

- Search for TeV γ -ray emission from blazar 1ES1218+304 with TACTIC telescope during March-April 2013.
K.K. Singh, K.K. Yadav, A.K. Tickoo, R.C. Rannot, P. Chandra, N.K. Agarwal,
K.K. Gaur, A. Goyal, H.C. Goyal, N. Kumar, P. Marandi, M. Kothari, H. Bhatt,
K. Chanchalani, N. Chouhan, V.K. Dhar, B. Ghosal, S.R. Kaul, M.K. Koul, R.
Koul, K. Venugopal, C.K. Bhat, C. Borwankar **Jai Bhagwan**, A.C. Gupta
New Astronomy, **36**, 1–8 (2015).

- Multiband variability in the blazar 3C 273 with XMM-Newton.

Nibedita Kalita, Alok C. Gupta¹, Paul J. Wiita, [Jai Bhagwan](#) and Kalpana Duorah

Monthly Notices of the Royal Astronomical Society, **451**, 5874–5883 (2015).

Abbreviations and Notations

Å	Angstrom
AD	Accretion Disk
AGN	Active Galactic Nuclei
BBB	Big Blue Bump
BL Lac	BL Lacertae objects
BLR	Broad Line Region
BPL	Broken Power Law
c	Velocity of light
CCD	Charge Coupled Device
DCF	Discrete Correlation Function
EC	External Compton
FR I	Fanaroff-Riley type I
FR II	Fanaroff-Riley type II
FSRQ	Flat Spectrum Radio Quasars
HSP	High synchrotron peaked blazar
HBL	High energy peaked blazar
IC	Inverse Compton
IDV	Intra-Day variability
ISP	Intermediate synchrotron peaked blazar
keV	Kiloelectronvolt
kpc	Kilo-parsec
λ	Wavelength
LBL	Low energy peaked blazar
LSP	Low synchrotron peaked blazar
LC	Light Curve

LP	Log-parabolic
LTV	Long Term Variability
M_{BH}	Black hole mass
MeV	Megaelectronvolt
MJD	Modified Julian Date
MW	Multi-wavelength
NED	Nasa Extragalactic Database
N_H	H_I column density
PL	Power Law
QPO	Quasi-Periodic Oscillation
QSO	Quasi Stellar Object
RL	Radio-loud
RQ	Radio-quiet
SNR	signal-to-noise ratio
SED	Spectral Energy Distribution
SMBH	Super Massive Black Hole
SSC	Synchrotron Self Compton
STV	Short Term Variability
UV	ultraviolet
XMM	X-ray Multi Mirror
z	redshift

ABSTRACT

Blazars comprise a subclass of radio loud Active Galactic Nuclei (AGN) that consist of BL Lacertae objects (BL Lacs) and Flat Spectrum Radio Quasars (FSRQs). They display large amplitude flux and polarization variability on diverse time-scales across the entire electromagnetic (EM) spectrum. According to the current paradigm, blazars have a Super Massive Black Holes (SMBHs) at their centre that accretes matter and produce relativistic jets pointing almost in the direction of our line of sight. The emission from blazars is predominated by non-thermal radiation produced by relativistic electrons spiralling around the magnetic field in relativistic jets. The spectral energy distributions (SEDs) of the blazars have two humps in $\log(\nu F_\nu)$ vs $\log(\nu)$ representation. The low energy SED hump peaks in the frequency ranging from sub-mm to soft X-ray bands and is well explained by synchrotron emission from an ultra-relativistic electron population residing in the magnetic field of the approaching relativistic jet. The high energy SED hump that peaks in MeV–TeV γ -ray bands, is usually attributed to inverse Compton (IC) scattering of photons of those relativistic electrons.

Multi-wavelength studies of blazars is an interesting topic in current astrophysics research. The launch of XMM-Newton space observatory on 10 December 1999 has opened an exciting new era of blazar astrophysics. Also the quasi-simultaneous optical ground based observations in multi-band can give important information to understand the blazars properties and emission mechanism.

In this thesis we have studied a sample of four TeV blazars. We have presented the multi-wavelength (X-ray, UV, and optical bands) study of the blazar PKS 2155–304 with XMM-Newton data and optical variability study of three TeV blazars with ground based optical observations. PKS 2155–304 is the brightest object in UV to TeV energies in Southern hemisphere. We have used all multi-wavelength observations of PKS 2155–304 taken with XMM-Newton space observatory in 2000–2012 period for long term flux and spectral variability study of the source. We find significant flux variation, in all bands, on time-scale of years with rms amplitude of ~ 35 -45%, through the optical/UV variation are correlated with those in the X-rays. We construct spectral energy

distributions (SEDs) that span more than three order of magnitude in frequency. We have fitted all SEDs with a combined power law and log-parabolic model. The model fitting indicate that the optical/UV and X-ray flux variations are mainly driven by model normalization variations, but the X-ray band flux is also affect by spectral variations. The energy at which the emitted power is maximum is positively correlated with the total flux. When source spectrum shift toward the high frequencies, the spectral ‘curvature’ increases, in contrast to what is expected if a single log-parabolic model were an acceptable representation of the broad band SEDs. On the basis of this analysis we have suggested that the optical/UV and X-ray emission in this source may arise from different lepton populations.

PKS 2155–304 is one of the best X-ray source for intra day variability study. We have analyzed one XMM-Newton observation of the blazar PKS 2155–304, made on 24 May 2002 in 0.3- 10 keV X-ray band. The light curve of this observation shows the high amplitude flux variability. We performed a time-resolved spectral study of the data, by dividing the data into eight segments. We fitted the data with a power-law and a broken power-law model, and in some of the segments we found a noticeable spectral flattening of the source’s spectrum below 10 keV. We also performed “time-resolved” cross-correlation analyses and detected significant hard and soft lags (for the first time in a single observation of this source) during the first and last parts of the observation, respectively. Our analysis of the spectra, the variations of photon-index with flux as well as the correlation and lags between the harder and softer X-ray bands indicate that both the particle acceleration and synchrotron cooling processes make an important contribution to the emission from this blazar. The hard lags indicate a variable acceleration process. We also estimated the magnetic field value using the soft lags. The value of the magnetic field is consistent with the values derived from the broad-band SED modeling of this source.

The optical variability study of three TeV blazars, PKS 1510-089, PG 1553+113 and Mrk 501 is also done in this thesis. The optical photometric observations of these TeV blazars are taken with two telescopes in india, one in Bulgaria, one in Greece and one in Serbia during 2012 June - 2014 September period. These observations covered a

total of 95 nights with a total of 202 B filter frames, 247 images in V band, 817 in R band while 229 images were taken in the I filter. This work is focused on multi-band flux and colour variability studies of these blazars on diverse time-scales which are useful in understanding the emission mechanisms. We searched for flux and colour variability on few months to few years time-scales. We found significant flux variations on these short/long time-scales with moderate colour variations. We also studied the correlation between the V magnitude of the source and corresponding variations in the (B-I), (B-V), (R-I), and (V-R) colour indices. Our observations for PG 1553+113 and Mrk 501 revealed mild BWB changes while the opposite (i.e., RWB) trend was found dominant in PKS 1510-089. The presence of both BWB and RWB trends in blazars can be explained by superposition of both blue and red emission components where the redder one is attributed to the synchrotron radiation from the relativistic jet while the blue component could come from the thermal emission from the accretion disk.

Contents

Declaration by Candidate	iii
Certificate by the Supervisor	v
Copy Right Transfer Approval Form	vii
Acknowledgements	xiii
List of Publications	xvi
Abbreviations and Notations	xix
Abstract	xxii
List of Figures	xxix
List of Tables	xxxii
1 Introduction	1
1.1 Active Galactic Nuclei (AGN)	1
1.2 AGN Classification and Unification Model	3
1.2.1 Radio Quiet AGNs	3
1.2.1.1 Radio Quiet QSOs (RQQSOs)	3
1.2.1.2 Seyfert 1 Galaxies (Sy1)	4
1.2.1.3 Seyfert 2 Galaxies (Sy2)	4
1.2.2 Radio Loud AGNs (RLAGNs)	5
1.2.2.1 Radio Loud QSOs (RLQSOs)	5
1.2.2.2 Broad Line Radio Galaxies (BLRGs)	6
1.2.2.3 Narrow Line Radio Galaxies (NLRGs)	6
1.2.2.4 Blazars	7
1.2.3 Variability of Blazars	9
1.3 Emission Mechanism	10
1.3.1 Thermal (Black Body) Radiation	10
1.3.2 Synchrotron Radiation	11

1.3.3	Inverse Compton Scattering	12
1.3.3.1	Synchrotron Self-Compton (SSC)	13
1.3.3.2	External Compton (EC)	13
1.4	Emission Models	13
1.4.1	Accretion Disk Based Models	13
1.4.2	Jet Based Models	14
1.4.2.1	Shock-in-Jet Model	14
1.4.2.2	Turbulent Jet Model	16
1.4.2.3	Swinging Jet Model	17
1.4.3	Some Other Possibilities	17
1.5	Motivation of the Thesis	18
1.6	Organization of Thesis	19
2	Multi-wavelength Data, Observation and Analysis Technique	21
2.1	Part 1.	
XMM-Newton	Observations and Data Reduction	21
2.1.1	XMM-Newton Telescope	21
2.1.2	X-ray Telescope	23
2.1.3	The European Photon Imaging Camera (EPIC)	25
2.1.4	The Optical Monitor(OM)	28
2.1.5	XMM-Newton data reduction procedure	32
2.1.5.1	XMM-Newton Science Archive	33
2.1.5.2	Standard data reduction procedure	33
2.1.5.3	XMM-Newton OM data reduction procedure	40
2.2	Part 2.	
Ground Based	Optical Observations and Data Reduction	41
2.2.1	Optical Telescopes	41
2.2.2	Optical Photometric Data Reduction	43
3	Multi-wavelength Flux Variability and Spectral Energy Distribution of the Blazar PKS 2155-304 from XMM-Newton	51
3.1	Introduction	51
3.2	The XMM-Newton Observations and data reduction	53
3.3	The observed long-term light curves	56
3.4	SED Modeling	57
3.4.1	Log-parabolic fits	58
3.4.2	Power-law plus log-parabolic (PLLP) fits	67
3.5	Discussion and Conclusions	71
4	Flux and Spectral Variability of the Blazar PKS 2155–304 with XMM-Newton: Evidence of Particle Acceleration and Synchrotron Cooling	77
4.1	Introduction	77
4.2	Data and Reduction	79
4.3	Excess Variance	80
4.4	Results	83
4.4.1	Light Curves	83
4.4.2	Spectral Variability	84

4.4.3	Correlation Analysis	88
4.5	Discussion and Conclusions	91
4.5.1	The spectral variability results	91
4.5.2	The cross-correlation results	93
4.5.3	Implications of the hard lags	94
4.5.4	Implications of the soft lags	95
4.5.5	Summary	96
5	Multi-band Optical Variability of Three TeV Blazars on Diverse Timescales	99
5.1	Introduction	99
5.2	Observations and Data Reductions	100
5.2.1	Telescopes and Data Reduction	101
5.3	Variability detection criterion	104
5.3.0.1	F-Test	105
5.3.0.2	χ^2 -test	105
5.3.0.3	Percentage amplitude variation	106
5.4	Results	106
5.4.1	PKS 1510–089	106
5.4.1.1	Flux and colour variability	108
5.4.2	PG 1553+113	110
5.4.2.1	Flux and colour variability	110
5.4.3	Mrk 501	111
5.4.4	Mrk 501	115
5.4.4.1	Flux and colour variability	115
5.4.5	Correlated variations between colour and magnitude?	118
5.5	Discussion and Conclusion	121
6	Summary and Future Plan	125
6.1	Summary	125
6.1.1	Long Term SED of the Blazar PKS 2155–304	125
6.1.2	Study X-ray Spectral behaviour of the Blazar PKS 2155–304 on IDV Timescale	126
6.1.3	Studies of Variability Timescales in X-ray, UV and Optical Bands	127
6.2	Future Plans	128

List of Figures

1.1	Schematic diagram of AGN structure	2
1.2	Example of AGN spectra	4
1.3	AGN classification on the basis of viewing angle	5
1.4	Picture of FR I and FR II type radio galaxies	6
1.5	Blazars classification on the basis of synchrotron peak position	7
1.6	The contribution of various emission mechanisms in broadband SED of Blazars	9
2.1	Artist's impression of XMM-Newton space observatory	22
2.2	Diagram of XMM-Newton space observatory	23
2.3	Technical drawing of one of the XMM-Newton X-ray telescope	25
2.4	The XMM-Newton mirror modules	25
2.5	Schematic of X-rays path in XMM-Newton telescope	26
2.6	Image of EPIC MOS and pn CCDs	27
2.7	Schematic diagram of Optical Monitor(OM) telescope	30
2.8	XMM-Newton PN Small Window(SW) mode image	34
2.9	Image of with and without pile-up source spectra	38
2.10	Picture of Five ground based optical telescopes	44
3.1	Long term variability light curves	57
3.2	UV versus soft (0.6-2.0 keV) and hard (2.0-10 keV) X-ray band plot	58
3.3	Best-fit SED model curves for three different observations	59
3.4	Best-fit SED model curves for three different observations	60
3.5	Best-fit SED model curves for three different observations	61
3.6	Best-fit SED model curves for three different observations	62
3.7	Best-fit SED model curves for three different observations	63
3.8	Best-fit SED model curves for three different observations	64
3.9	Best-fit SED model curves for two different observations	65
3.10	Plots of the best-fit model parameters as a function of the UVW2 and the 0.6–2 keV count rates	69
3.11	SED model parameters vs turn over frequency and peak frequency plot	73
4.1	The background subtracted X-ray light curve of PKS 2155–304 in different energy bands	81
4.2	The pn count rate spectra corresponding to the various segments of observation ID 0124930501	87
4.3	Photon-index versus the 2.0-10.0 keV flux plot	89

4.4	Time lag plot between the 0.3–0.5 keV band light curve and the 0.5–2, 2–4 and 4–10 keV band light curves	90
5.1	Short-term through long-term variability LCs and colour indices of PKS 1510–089	107
5.2	Zoom view of variability seen in figure 5.1	108
5.3	Light curves for PG 1553+113	112
5.4	Long-term variability LCs and colour indices of PG 1553+113	113
5.5	Long-term variability LCs and colour indices of Mrk 501	116
5.6	Zoom view of variability seen in figure 5.5	117
5.7	Colour magnitude plots on short timescales for blazars	119

List of Tables

2.1	Parameter details of an XMM-Newton X-ray telescope	24
2.2	Parameters detail of EPIC-pn and EPIC-MOS CCDs	27
2.3	Parameters of the six standard readout modes as implemented in-orbit	29
2.4	The OM filter table with their wavelength bands in nanometre(nm) and the preliminary zero points	31
2.5	Details of ground based telescopes and instruments	42
2.6	The details about broad band filters	43
3.1	Observation log of PKS 2155-304 with XMM-Newton	55
3.2	The SED best-fitting model parameter values for the LP model	66
3.3	The SED best-fit model parameter values for the power-law+log-parabolic model	72
4.1	Results of X-ray spectral fits to PKS 2155–304	85
5.1	Observation log of optical photometric observations of PKS 1510-089	101
5.2	Observation log of optical photometric observations of PG 1553+113	102
5.3	Observation log of optical photometric observations of Mrk 501	103
5.4	Results of IDV observations of PG 1553+113	114
5.5	Results of STV/LTV studies for magnitude changes in each band	118
5.6	Color–magnitude diagram on short timescale for PKS 1510-089	119
5.7	Color–magnitude diagram on short timescale for PG 1553+113	120
5.8	Color–magnitude diagram on short timescale for Mrk 501	120

Chapter 1

Introduction

1.1 Active Galactic Nuclei (AGN)

AGN, refers to the existence of energetic phenomena in the nuclei, or central regions, of galaxies which can not be attributed to stars. An AGN has a super-massive black hole at its center which accretes matter. In some AGN, this is accompanied by the acceleration of ultra relativistic particles along collimated jets. They are the most luminous persistent sources of electromagnetic (EM) radiation in the Universe and their evolution as a function of cosmic time provides constraints on models of the cosmos.

For about a decade it has been well established that super massive black holes (SMBHs, with masses between $10^6 - 10^{10} M_{\odot}$) are present in the nuclei of all galaxies with stellar bulges. At any given time a few percent of these SMBHs are fed a sufficient amount of gas that they will possess significant accretion disks. These disks can emit more radiation than all of the stars in the entire host galaxy because of the general relativistic effects that yield a very high efficiency for the conversion of matter into radiation as it spirals into a BH. This is the fundamental mechanism underlying “active galactic nucleus”, or AGN. A simplified version of a radio-loud AGN is presented as a cartoon in Fig. 1.1. Radio-quiet AGN can also be presented by the same figure if we remove both sided jets from it.

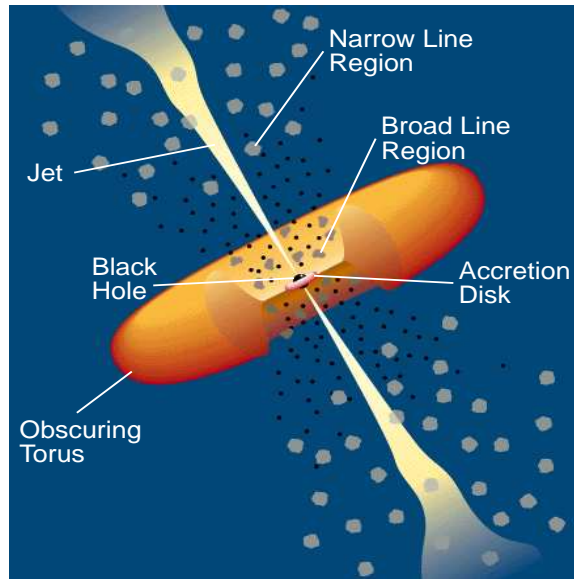


Figure 1.1 A schematic diagram of radio loud AGN (Figure courtesy : [Urry & Padovani \(1995\)](#)). The SMBH is surrounded by accretion disk. Broad emission lines are produced by the clouds orbiting above the disk. A thick and dusty torus obscures the broad-line region and several features of AGN activity from transverse line of sight. Narrow lines are produced by the clouds much farther from the central source.

Fig. 1.1 show a SMBH at AGN center which is surrounded by an accretion disk, both sided relativistic charged particle jets (in radio-loud AGN), no jets (in radio-quiet AGN), cloud of dust and gas (thick dusty torus) which is responsible for infra-red emission, and region for broad and narrow lines emission. In the cartoon a front portion of thick dusty torus is removed to show the central region of AGNs. The emission line region with the line widths (equivalent width EW) upto the order of $\sim 10,000 \text{ km s}^{-1}$ is known as broad line region (BLR) of emission zone and it is believed to be caused by photo-ionization due to hot accretion disk. BLR region lies up to a distance of ~ 1 parsec from the SMBH. Beyond the dusty torus, there are clouds of slower moving gas and dust which produces narrow emission lines with EW of around $1,000 \text{ km s}^{-1}$. This emission region is known as narrow-line region (NLR). It lies at a distance of $\sim 10\text{pc}$ to 1 kpc from the central engine of AGNs.

It is well accepted that accretion onto a SMBH powers AGN. In the case of accretion onto a SMBH, the produced jets are extreme, with matter in such jets moving with relativistic speed. Jets carry a fraction of in-falling matter and its angular momentum

away from the central object. The emission mechanisms which convert the energy of in-falling gas into the extreme EM radiation, we observe are still not very well understood. AGNs emit radiation in the complete EM spectrum (i.e. from radio to γ -rays). The overall shape of multi-wavelength (MW) spectral energy distribution (SED) follow roughly a power law form and can be describe as follows

$$F_\nu = A\nu^{-\alpha} \quad (1.1)$$

Here F_ν is flux at the frequency ν , and α represents the spectral index.

1.2 AGN Classification and Unification Model

It has long been known that there are two major classes of AGNs. Roughly 85–90 % of these have very little radio emission (loudness parameter $R = F_{5GHz}/F_B \leq 10$, here F_{5GHz} = flux at radio 5 GHz and F_B = flux at optical B band 4400Å) and are therefore called radio-quiet AGNs (RQAGNs). The remaining ~ 10 –15 % of AGNs are radio-loud AGNs (RLAGNs). Based on AGNs unification model which is an orientation based scheme, different sub-classes of RQAGNs and RLAGNs are displayed in Fig. 1.3. The figure is divided into 2 parts, upper and lower part of figure present different subclasses of RLAGNs and RQAGNs, respectively. Different subclasses of AGNs show different optical spectral lines which we described below and represented in Fig. 1.2.

1.2.1 Radio Quiet AGNs

1.2.1.1 Radio Quiet QSOs (RQQSOs)

RQQSOs are more luminous than other objects in RQAGNs class. In general the host galaxy of RQAGNs are spiral but it is not always true. From AGN unification model given in Fig. 1.3, RQQSOs lie perpendicular to the disk plane. These are classified as QSO if its absolute optical magnitude $M_V \leq -24.9$ (Miller et al. (1990)).

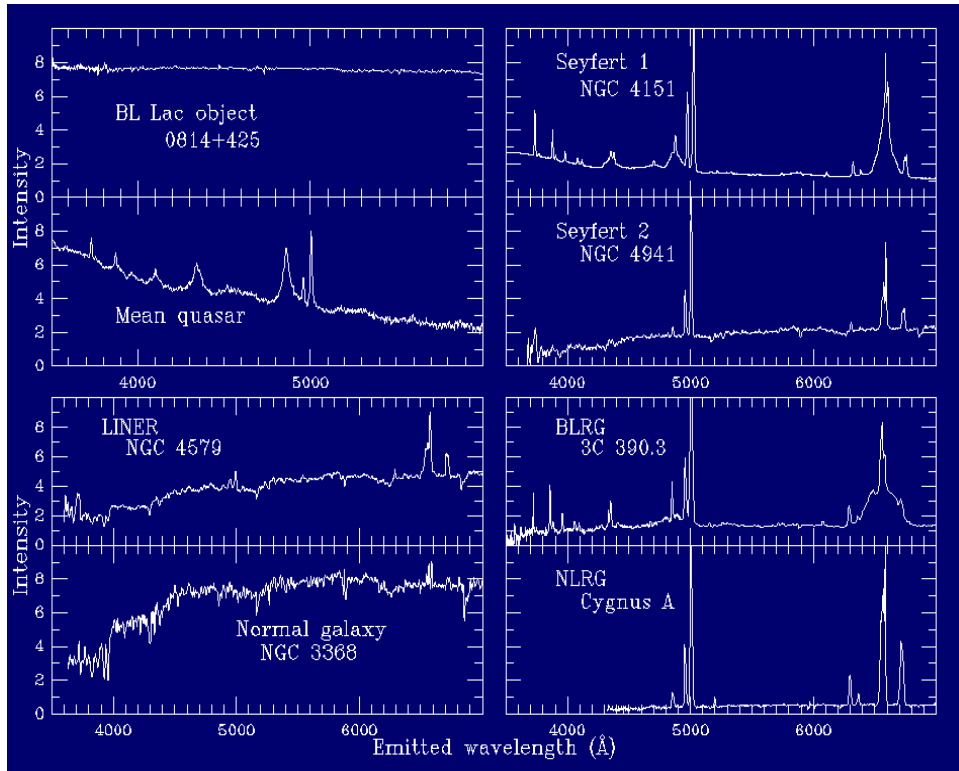


Figure 1.2 Example of different class of AGN spectra. All spectra are shown in the emission rest frame for ease of comparison. Image credit goes to Bill Keel and it taken from <http://www.astr.ua.edu/keel/agn/spectra.html>.

1.2.1.2 Seyfert 1 Galaxies (Sy1)

Seyfert galaxies are identified by Carl Seyfert as a new class of objects [Seyfert \(1943\)](#). These are comparatively low-luminosity and low redshift AGNs. In deep imaging the host galaxy is usually visible with high central surface brightness. The Seyfert galaxies have typical luminosity in the range $10^{41} - 10^{44} \text{ erg s}^{-1}$. Optical spectral of Seyfert 1 galaxies show both broad permitted lines (Full Width Half Maximum (FWHM) = 1 – 10,000 km s^{-1}) and narrow permitted and forbidden lines (FWHM < 1000 km s^{-1}) (see the top right panel of Fig. 1.2). From AGN unification model given in Fig. 1.3, Sy1 galaxies lie with moderate angles with the disk plane.

1.2.1.3 Seyfert 2 Galaxies (Sy2)

Optical spectral of Seyfert 2 galaxies (Sy2) show only narrow permitted and forbidden lines (FWHM < 1000 km s^{-1}) (see second from top in right panel of Fig. 1.2). From

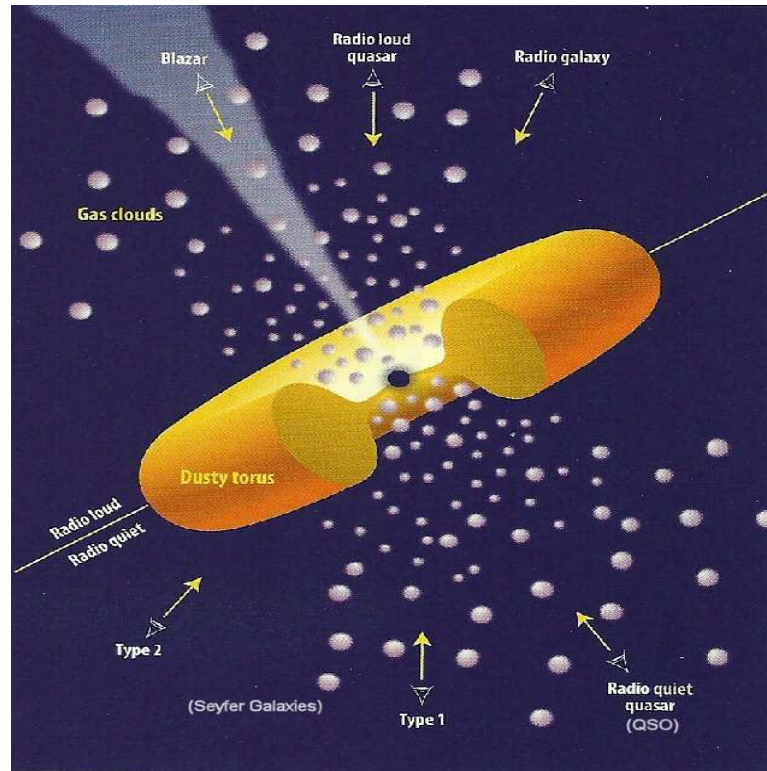


Figure 1.3 Schematic representation of our present understanding of the AGN phenomenon in unified scheme. The type of object we see depends on the viewing angle, whether or not the AGN produces a significant jet emission, and how powerful the central engine is. (Figure courtesy : [Urry & Padovani \(1995\)](#)).

AGN unification model given in Fig. 1.3, Sy2 galaxies lie nearly in the disk plane.

1.2.2 Radio Loud AGNs (RLAGNs)

1.2.2.1 Radio Loud QSOs (RLQSOs)

Radio Loud QSOs (RLQSOs) show high luminosity as RQQSOs ($M_V < -24.9$) ([Miller et al. \(1990\)](#)). They have similar broad and narrow emission lines in their optical spectra as Sy1 galaxies (see second from top in left panel of Fig. 1.2). But these objects have radio loudness $R \geq 10$. RLQSOs can be further classified into two subclasses: Steep-Spectrum Radio Quasars (SSRQs) with radio spectral index $\alpha_r \geq 0.5$, and Flat-Spectrum Radio Quasars (FSRQs) with $\alpha_r \leq 0.5$ where spectral index is defined in eq. (1.1). From AGN unification model given in Fig. 1.3, RLQSOs lie with moderate angles with the jet.

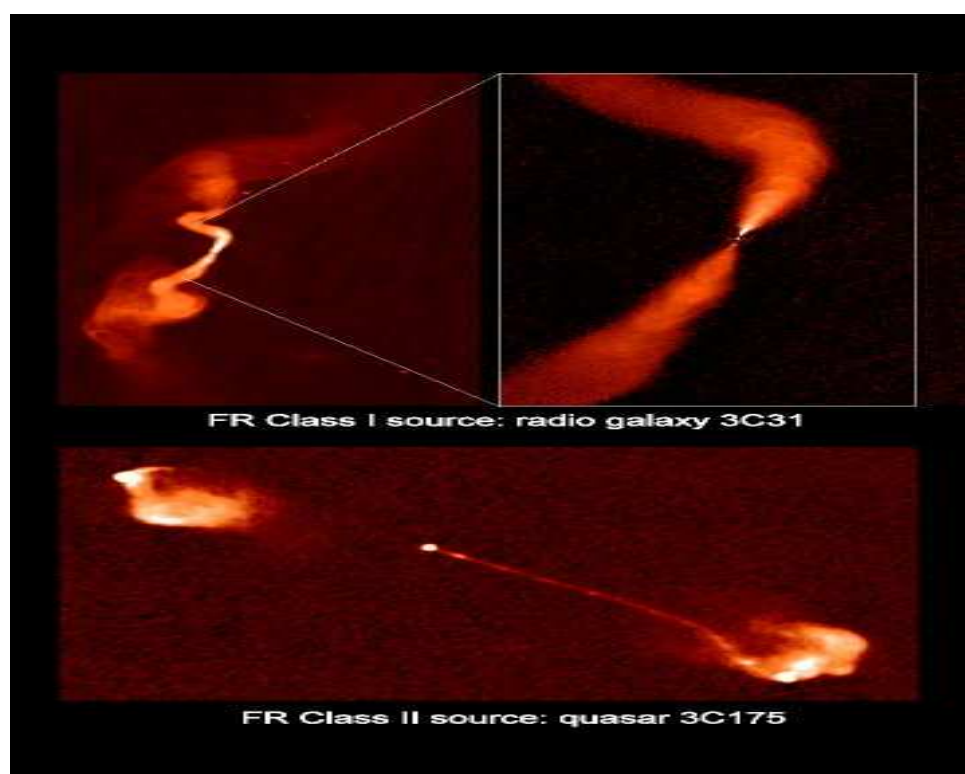


Figure 1.4 Picture of FR I and FR II type radio galaxies, 3C31 (top panel) and 3C175 (bottom Panel) respectively. Graphics by Dinesh

1.2.2.2 Broad Line Radio Galaxies (BLRGs)

Broad Line Radio Galaxies (BLRGs) have optical spectral lines and radio loudness like RLQSOs. But these objects have less luminosity than RLQSOs. BLRGs display exclusively Fanaroff-Riley type 2 (FR II) [Fanaroff & Riley \(1974\)](#) radio morphologies. From AGN unification model given in Fig. 1.3, BLRGs lie with moderate angles with the jet. The FR II have radio morphologies characterized by powerful edge-brightened double lobes with prominent hot spots (see bottom panel of Fig. 1.4).

1.2.2.3 Narrow Line Radio Galaxies (NLRGs)

Narrow Line Radio Galaxies (NLRGs) have optical spectral lines like Sy2 galaxies and radio loudness like RLQSOs. But these objects have less luminosity than RLQSOs. NLRGs display exclusively Fanaroff-Riley type 1 (FR I) ([Fanaroff & Riley \(1974\)](#)) radio morphologies. From AGN unification model given in Fig. 1.3, NLRGs lie nearly in the

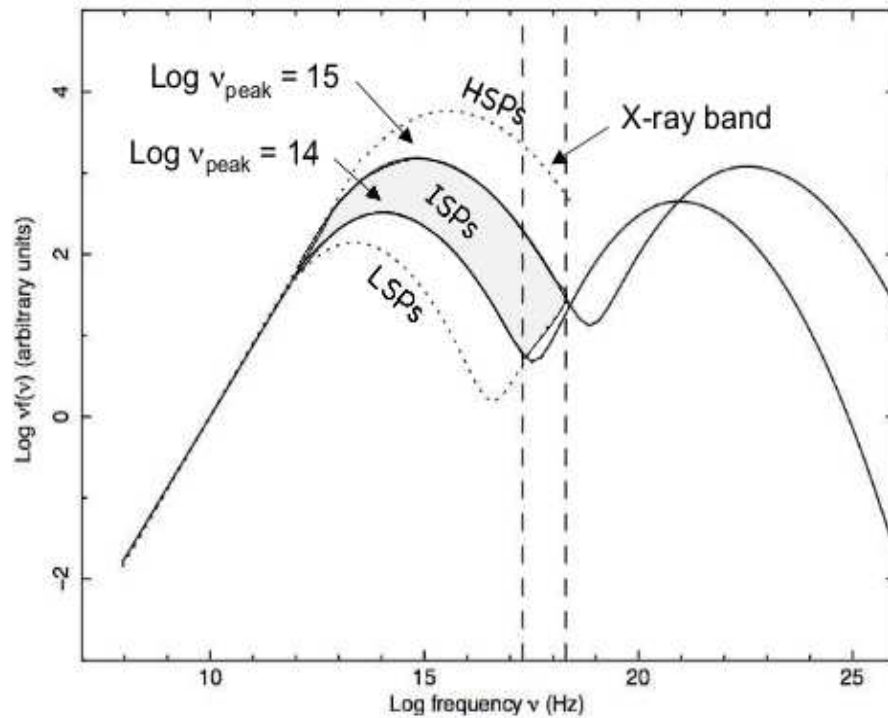


Figure 1.5 The location of synchrotron peaks in the SEDs of the three kinds of blazars. The synchrotron power of LSP peaks below 10^{14} Hz, ISP peaks between 10^{14} - 10^{15} Hz and HSP peaks above 10^{15} Hz frequencies. Figure courtesy : [Raino' et al. \(2009\)](#)

disk plane. The FR I have radio emission peaking near the nucleus (core-brightened), have rather diffuse edge-darkened lobes (see top panel of Fig. 1.4).

1.2.2.4 Blazars

A small subset of RLAGNs called blazars show rapid variability at almost all wavelengths of the EM spectrum ([Hayashida et al. \(2015\)](#) and reference therein) with the emission being strongly polarized (optical linear polarization $\geq 3\%$). BL Lac objects (BLLs) and flat spectrum radio quasars (FSRQs) are collectively known as blazars. BLLs show almost featureless optical continua (no prominent emission lines ($EW > 5\text{\AA}$) or absorption lines) ([Marcha et al. \(1996\)](#); [Stocke et al. \(1991\)](#)) while FSRQs show prominent emission lines in their optical spectra. Blazars emit relativistic charged particle jets nearly aligned to our line of sight (jet angle $\leq 10^\circ$) ([Urry & Padovani \(1995\)](#)) (see Fig. 1.3).

The radiation from blazars is dominated by non-thermal emission at all wavelengths, consisting of two broad spectral bumps (Ghisellini et al. (1997); Fossati et al. (1998)): A low-frequency component from radio to the UV or X-rays, generally agreed to be due to synchrotron radiation from relativistic electrons in the jet, and a high-frequency component from X-rays to γ -rays, which can be either due to Compton scattering of lower-frequency radiation by the same relativistic electrons (leptonic models (Krawczynski (2004))) or due to interactions of ultrarelativistic protons in the jet (hadronic models), either via proton synchrotron radiation (Mücke et al. (2003)) or via secondary emission from photo-pion and photo-pair production process Böttcher (2007), and references therein.

Blazars can be classified into three sub-classes, depending on the peak frequency of their synchrotron emission: LSPs (low-synchrotron-peaked blazars), consisting predominantly of LBLs (red or low energy or radio selected blazars) and defined by a peak of their synchrotron component at $\nu_{sy} < 10^{14}$ Hz, ISPs (intermediate-synchrotron-peaked blazars), consisting mostly of intermediate blazars, defined by 10^{14} Hz $< \nu_{sy} < 10^{15}$ Hz, and HSPs (high-synchrotron-peaked blazars), all of which are HBLs (blue or high energy or X-ray selected blazars) and which are defined through $\nu_{sy} > 10^{15}$ Hz (Abdo et al. (2010)). The high-energy component of the spectral energy distribution (SED) of blazars extends up to γ -rays, peaking at GeV energies in LSPs and at TeV energies in HSPs. SEDs of different sub-classes of blazars are displayed in Fig. 1.5. Blazar properties are consistent with relativistic beaming, i.e. bulk relativistic motion of the jet plasma at small angles to the line of sight, which gives rise to a strong amplification and rapid variability in the observer's frame.

In the present thesis, we have worked on the blazar class of AGNs. Hereafter, we focus on the descriptions related to blazars.

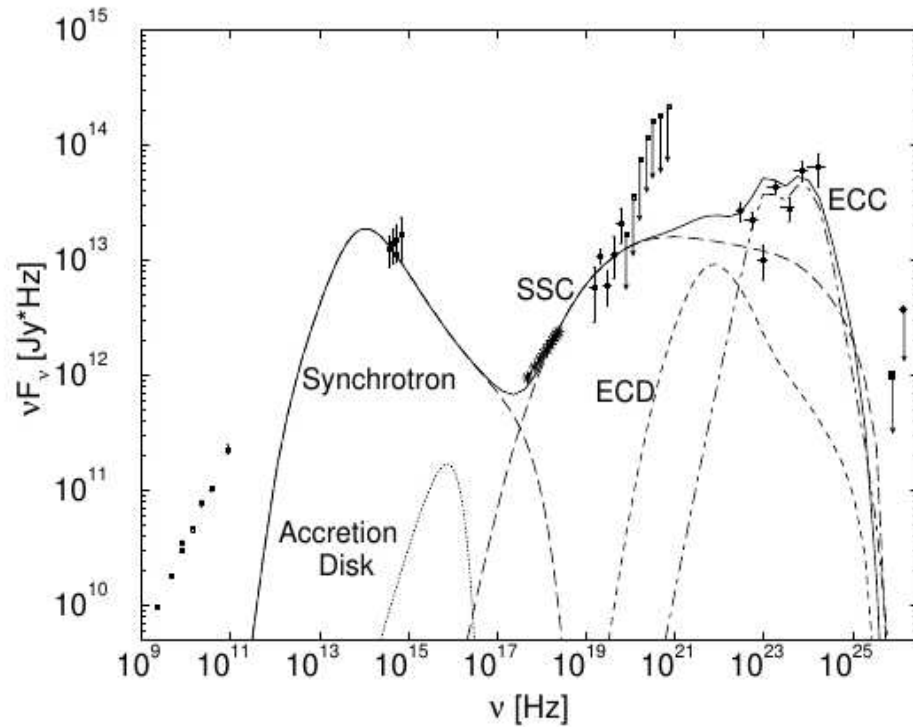


Figure 1.6 The broadband SED of BL Lac object showing the contribution of various emission mechanisms through radio to γ -rays. The low energy part of SED is mainly dominated by synchrotron emission with an additional contribution from accretion disk. However, the high energy photons are produced by SSC+EC. Figure courtesy : [Böttcher & Bloom \(2000\)](#)

1.2.3 Variability of Blazars

The study of variability is one of the most powerful tools for understanding the nature and processes occurring in blazars. Variability of blazars can be broadly divided into three classes. Significant variations in flux may occur over few tens of minutes to the course of less than a day, often called micro-variability, intra-night variability or intra-day variability (IDV) ([Wagner & Witzel \(1995\)](#)). Short term variability (STV) can range time scales from days to few months and long term variability (LTV) can have time scales of several months to several years ([Gupta et al. \(2004\)](#)). The timescale of variability can put an upper limit on the size of emitting region ($R \leq c\Delta t$) and can also be used for calculating the mass of SMBH.

1.3 Emission Mechanism

Broad band SEDs of different sub-classes of blazars are shown in Fig. 1.6 which clearly show the MW blazar emission is mixture of thermal and non-thermal radiations from accretion disk and jets, respectively. Blazars are highly variable sources and vary ~ 5 mag in low-state to outburst state. When a blazar is in low-state, thermal emission from accretion disk can give clear signature in SEDs but when the blazar goes in the outburst state, the emission is dominated by non-thermal radiation. The radio band emission is due to synchrotron radiation, thermal emission is by accretion disk in optical/UV bands, and in X-rays and γ -rays emissions are produced by inverse Compton (IC) scattering of synchrotron photons and also of the seed photons outside the jet (e.g. photons from accretion disk, BLR region etc.). In following subsections, we describe in details about thermal and non-thermal emission mechanisms.

1.3.1 Thermal (Black Body) Radiation

The radiation emitted by matter in thermal equilibrium is known as thermal emission. The thermal emission is the emitted energy by black body radiation and can be defined by Planck's Law. In the case of AGN, the thermal structure of accretion disk follow a negative temperature gradient which imply the temperature decreases as the radial distance from the central SMBH (Shakura & Sunyaev (1973)). The overall structure of accretion disk is governed by mass of the central SMBH and the accretion rate. For the standard optically thick and geometrically thin accretion disk, the temperature varies as a function of radial distance from the center as $T \propto r^{-3/4}$ (Shakura & Sunyaev (1973)). Thus, the accretion disk is a multi-colour black body where each annuals radiates following Planck's Law given by

$$F(\nu) = \frac{2h\nu^3/c^2}{\exp(h\nu/kT(r)) - 1} \quad (1.2)$$

Here h , c , and k are Planck's constant, speed of light in vacuum, and the Boltzmann's constant, respectively. $T(r)$ is the temperature of the black body at radial distance r from the central engine SMBH.

The temperature of accretion disk in AGNs vary in the range of $\sim 4000 - 40000$ K, so, it emit thermal radiation in optical-UV bands of EM spectrum. Hence the optical-UV emission in AGNs are dominated by thermal radiation from accretion disk (Malkan & Sargent (1982)). The overall SEDs of blazars are shown in Figure 1.6.

1.3.2 Synchrotron Radiation

The synchrotron radiation, the emission of highly relativistic and ultrarelativistic electrons gyrating in a magnetic field, is the process which dominates much of high energy astrophysics. This process is responsible for the radio emission from the Galaxy, supernova remnants, extra-galactic radio sources, etc. Synchrotron radiation characteristically is highly polarized and continuous. Its intensity and frequency are directly related to the strength of the magnetic field and the energy of the charged particles affected by the field. Synchrotron radiation is not dependent on the temperature of a given astronomical source; a relatively cool object can release substantial amounts of electromagnetic energy in this form. Synchrotron radiation is thus often termed nonthermal radiation. It is observed in optical and X-ray continuum emission of quasars. Jet of AGNs containing magnetized relativistic plasma emit synchrotron radiation at radio to optical (sometimes X-ray) frequencies. So, the lower energy part of blazar SED is dominated by synchrotron mechanism. The spectrum of power emitted by an ensemble of electrons follows a power law given by

$$P(\nu) \propto \nu^{-\alpha}, \quad \alpha = \frac{p-1}{2} \quad (1.3)$$

where α is the spectral index of the observed power law and p is the power law index of energy distribution of emitting electrons. The power law distribution of electrons can be represented in a variety of ways such as acceleration through shocks (Blandford (1990)). But, the observer can see this power law spectrum only if there is no absorption by the

emitting region. In presence of magnetic field, the emitted photons can be absorbed by the emitting region itself or by some other medium in between. The absorption of emitted radiation by the emission region itself is known as “synchrotron self-absorption” which produces an inverted power-law spectra with index, $\alpha \sim -5/2$. But a slope of $-5/2$ has never been observed so far, and what is found in compact sources is a spectral index considerably flatter than is found in extended sources or in spectra that is complex. This is due to that the different parts of the source become optically thick at different frequencies, and therefore the observed spectrum is a superposition of spectra that peak there. Synchrotron self-absorption coefficient is inversely dependent on the frequency, so a given source will be optically thick below the frequency ν_a and may be considered to be optically thin at all higher frequencies.

1.3.3 Inverse Compton Scattering

Inverse Compton (IC) scattering involves the scattering of low energy photons to high energies by ultrarelativistic electrons so that the photons gain and the electrons lose energy. The process is called inverse because the electrons lose energy rather than the photons, the opposite of the standard Compton effect. Therefore, this process converts low energy photons (IR/optical) to high energy photons (X-ray/ γ -ray). This is thought to be an important emission mechanism in the production of X-rays in AGN where ultraviolet (UV)/optical photons from the accretion disk are thought to be scattered by relativistic electrons in the corona producing a power law X-ray spectrum. The hard X-ray tail of AGN spectra is believed to be caused by Compton up scattering of soft photons in a hot plasma above the accretion disk. In AGNs, the seed (or low energy) photons may be synchrotron photons produced by the same electron population in the jet or photons external to the jet coming from the accretion disk, the dusty torus or emission line clouds.

1.3.3.1 Synchrotron Self-Compton (SSC)

In blazars, synchrotron photons are the seed (or low energy) photons produced by the same electron population in the jet. This process is known as SSC (Marscher & Gear (1985)).

1.3.3.2 External Compton (EC)

Accretion disk can directly produced soft photons (Dermer & Schlickeiser (1993)) or by the dusty torus (Błażejowski et al. (2000)), or reprocessed by the broad line region (BLR; Sikora (1994)). The relativistic electrons in jets will interact with these soft photons and get boosted to higher energies (e.g. GeV-TeV γ -rays). This process is known as External Compton (EC) emission. The high energy part of blazar spectrum is mainly contributed by IC (SSC or EC) scattering processes (see Figure 1.6). The optical-UV photons get up-scattered to GeV-TeV γ -rays energies in blazar jets by these scattering processes.

1.4 Emission Models

In the following subsections, we describe briefly the standard emission models for RLAGNs. Since blazar is a sub-class of RLAGNs, these emission models can explain the blazars observational properties. Blazar variability on diverse timescales can be either “intrinsic” to the blazars or due to some “extrinsic” nature. In this section, the descriptions for the standard models which are responsible for intrinsic blazars emission.

1.4.1 Accretion Disk Based Models

Since blazars are variable on all time scales and in all energy bands, their variability can be used to improve our understanding of the accretion process on to the super massive central black hole which powers the nuclear activity. The most puzzling variations are those happening on the time scale of a few minutes to less than a day i.e. on IDV

timescales. Variability observations of blazars on IDV time scale can provide important clues to the physics of the innermost nuclear regions in these objects. IDV in blazars (mainly in their low-state) involving accretion-disk based models. These models include pulsations of the gravitational modes of the gaseous disk (Kato & Fukue (1980); Nowak & Wagoner (1992)) or orbital signatures from “hot-spots” in the gas surrounding the black hole, either from the disk itself or the corona above it (Zhang & Bao (1991); Mangalam & Wiita (1993)). Accretion-disk based models can explain the variations in optical, UV and X-ray bands, but are difficult to connect to the observed rapid variability in γ -rays.

1.4.2 Jet Based Models

Jet based models are the most important models to explain the multi-wavelength variability observed in blazars on diverse timescales. Here we briefly describe some jet based AGN models.

1.4.2.1 Shock-in-Jet Model

In the case of blazars, the model which we choose assumes the emitted jet direction along the line of sight of the observer. It was first proposed by Blandford & Rees (1978) and further developed in more detail with observational properties by (Blandford & Königl (1979)); Marscher (1980); Königl (1981)).

The non-thermal emission from sub pc to kpc scale AGN jets implies powerful particle acceleration mechanism is at work. It is generally believed that shock fronts propagating down AGN jets are associated with particle acceleration. The electrons are energized along the shock front and then move away at a speed close to the velocity of light as they lose energy via synchrotron and IC processes. Changes in the magnetic field and/or injection rate of relativistic electrons, or the bulk Lorentz factor of flow would be responsible of the observed jet spectrum (Marscher & Gear (1985)). The synchrotron emission from plasma moving towards us at a velocity βc and the bulk Lorentz factor Γ

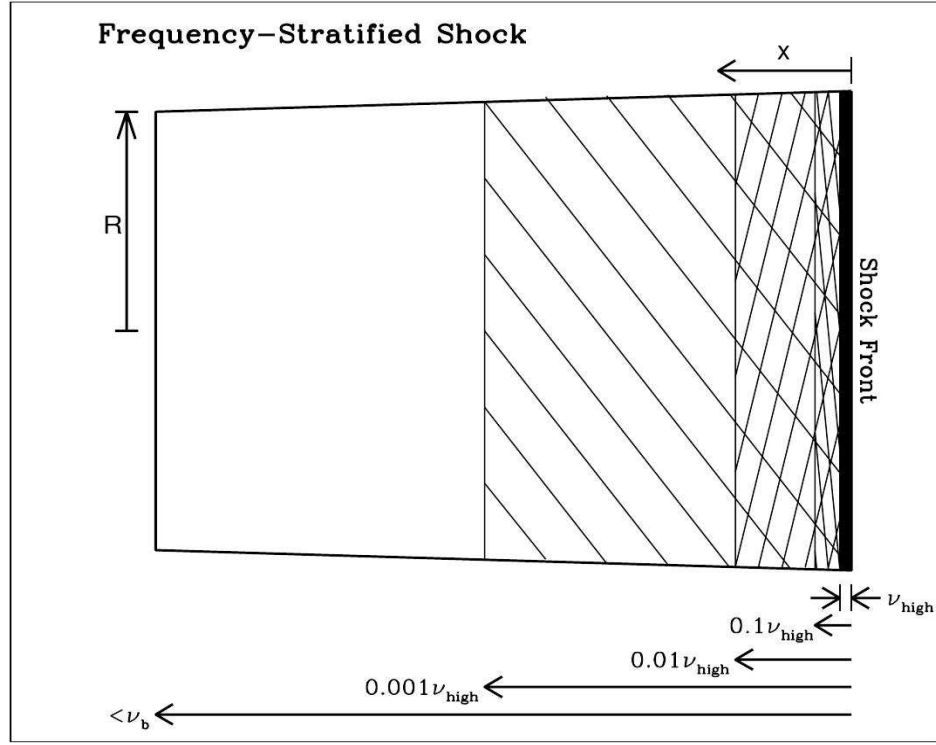


Figure 1.7 A sketch of shock propagating down a relativistic jet. The electrons are accelerated at the shock front and drift behind the shock while losing energy via radiative losses. Figure courtesy : [Marscher \(2009\)](#)

can be given as

$$\Gamma = [1 - \beta^2]^{-1/2} \quad (1.4)$$

is strongly increased, and the observed flux from the AGN is given by

$$S_{obs} = S_{em}[\Gamma(1 - \beta \cos \theta)]^{-(p-\alpha)} \quad (1.5)$$

here θ is the jet angle to the line of sight to the observer, $2 \leq p \leq 3$ which depend on the flow of jet which may be smoothly or knotty, and α is spectral index which is defined as $S_\nu \propto \nu^{-\alpha}$. The formation of jets in AGNs is tied to the accretion disk, so the shock waves may be produced by disturbances that originate there. Major increase in either the bulk speed or internal energy of jet flow which will cause shock wave to form and propagate down to the jet and its function is to convert super-sonic flows to sub-sonic flows ([Marscher \(1996\)](#)).

Shock front compresses the plasma which result an increase in its internal energy, magnetic field, and velocity etc. In this process, energies of the particles increase because of successive shock-crossing, their velocity distributions become isotropic with respect to the flow due to internal scattering. By crossing the shock front multiple times, particles can be accelerated to high energy before they leave the acceleration region (diffusive shock acceleration, Schwadron et al. (2008)). The acceleration is most efficient when the magnetic field is perpendicular to the shock front, since the particles can stream more freely along the field lines. Hence, the synchrotron emission in shocks can be amplified by: (i) increase in density behind shock front, (ii) increase in magnetic field strength, (iii) increase in internal energy, (iv) diffusive shock acceleration.

The particles accelerated across the shock front emit radiation in multi-wavelength depending upon their energy. A shock-induced flare is spread over many decades of frequencies where the high energy photons emerge sooner and within a small distance across the shock front and the thickness of this sheet increases as frequency decreases (Marscher (1996)). So, in a shock-induced flare, the γ -ray and X-ray flux peaks first, followed by optical, IR and then radio. The frequency stratification in a shock induced flare is shown in Fig. 1.7.

1.4.2.2 Turbulent Jet Model

Kelvin-Helmholtz type instabilities due to the interaction of a fast inner spine of the jet with a slower, outer layer could play an important role in the production of IDV at a variety of wavelengths Romero et al. (1999). The plasma in relativistic jets is highly hydro-magnetically turbulent and observation ally this fact is confirmed that the linear polarization is considerably less than that is expected from synchrotron radiation which implies the magnetic field component is randomly oriented. Turbulence form the eddies of many different length scales. Most of the kinetic energy of the turbulent motion is contained in the large scale structures called “eddyies”. Therefore, eddies are the regions of higher electron density , velocity and magnetic field etc. As the disturbance propagates down the jet, it brightens at sites where it encounters density and/or magnetic field enhancements and fades where it encounters diminishments. Here

magnetic field fluctuations play a major role which amplify or reduce the flux density at a given location in the shock (Marscher (1996)). So, the turbulent jet can explain key characteristics of blazar variable emission.

1.4.2.3 Swinging Jet Model

In blazars considerable fluctuations in amplitudes, time scales and/or flares can be observed, and for which geometrical effects in jets can introduce variations (Wagner & Witzel (1995)). Camenzind & Krockenberger (1992) suggest that shocks are unlikely to travel along the jet axis. Every volume element of plasma in relativistic jets possess a finite angular momentum and moves on a helical trajectory due to superposition of out-flow and circular motion. They argued that these knots have enhanced electron density which are injected at a finite jet radius. Therefore, when the knots of higher electron density move relativistically on helical trajectory, the direction beam varies with time. Also, if a shock moves down a jet with a helical structure, each time the shock meets the twist of that structure that is closest to the line of sight of the observer (say the near-side of a conical jet) then the boosting will be the greatest. If the jet is really conical, then the time between the shock intersections and the helical structure might change which implying a ‘quasi-periodic oscillation’ instead of a strictly periodic oscillation.

1.4.3 Some Other Possibilities

Blazar variability is either intrinsic to the source or due to some extrinsic sources. There are two main reasons which can cause extrinsic variability in the blazar. One reason is due to “interstellar scintillation” in which the presence of turbulence in the interstellar medium (ISM) of our galaxy, as well the probability of its existence in the host galaxy of an AGN can effect the reception of low frequency photons. This reason is only applicable in the case of low-frequency radio observations. The another reason is “gravitational microlensing” in which fore-ground or background objects in the blazar field at nearly similar redshift of the blazar can play the role for making the observed emission gravitationally lensed. But such cases are very rare in known blazars. Since

in the present thesis, we have studied blazars in optical/UV and X-ray bands, so, the “interstellar scintillation” will not play any role. No blazar studied in the present thesis has gravitational lens system, so, this reason for extrinsic variability is also ruled out. Therefore, the extrinsic variability is beyond the scope of the present thesis.

1.5 Motivation of the Thesis

AGNs are intrinsically among the most luminous object in the Universe. They have SMBHs at their center. But due to large redshift, it is hard to resolve their detailed fine properties with exiting multi-wavelength observing facilities. In AGNs, on the point of view of multi-wavelength observations, blazars are the extreme and most interesting class of objects. And in blazars class the TeV (10^{12} eV) emitting blazars are the most recent discoveries. In the present thesis, we worked on the TeV blazar class of AGNs and selected 4 blazars for the study.

The present thesis work can be divided into two paprts: (1) space based (XMM-Newton) studies of the blazar PKS 2155–304 in multi-wavelength (optical/UV, and X-ray bands); (2) ground based (5 optical telescopes in which 2 are located in India, 1 in Greece, 1 in Blugaria, and 1 in Serbia) with quasi-simultaneous multi-band optical observations of three TeV blazars: PKS 1510–089, PG 1553+113, and Mrk 501. Using XMM-Newton data of the blazar PKS 2155–304 we studied following:

- Long term flux variability of the blazar in optical, UV and X-ray bands.
- Long term SED studies of the blazar in optical, UV and X-ray bands.
- X-ray spectral study on IDV timescale.
- Search for soft and hard lag between X-ray bands.

Using 5 ground based multi-band optical observations of three TeV blazars: PKS 1510–089, PG 1553+113, and Mrk 501; we studied following:

- We searched for optical IDV in the blazar PG 1553+113.

- We studied flux and color variation on STV/LTV timescales in all these 3 TeV blazars.
- We also studied color magnitude correlation in these three TeV blazars on STV/LTV timescales.

Using our observational results of 4 TeV blazars, we tried to explain the results with standard model of radio-loud AGNs.

1.6 Organization of Thesis

In the thesis, there are total 6 chapters. Different chapters contain following:

- **Chapter 1** is introduction of the subject which contains about AGN, its classification based on unified model, emission mechanism, and standard model for emission mechanism.
- **Chapter 2** describe about XMM-Newton satellite and scientific instruments on board. This chapter also contains about optical telescopes used for observing. We describe the XMM-Newton and ground based telescope data analysis.
- **Chapter 3 and 4** describe the results based on the data taken from XMM-Newton satellite for the blazar PKS 2155–304.
- **Chapter 5** describe the results based on optical data of 3 TeV blazars: PKS 1510–089, PG 1553+113, and Mrk 501.
- **Chapter 6** we summarize the main result of the thesis work, and future plan.

Chapter 2

Multi-wavelength Data, Observation and Analysis Technique

In this thesis, we have focused on the multi-wavelength (MW) study of TeV blazars. For the MW studies, we have used X-ray, UV and optical frequencies data. This chapter is divided into two parts. In the first part, we describe the XMM-Newton space based telescope data which we collected in X-ray, UV and optical frequencies. In the second part, the ground based optical telescopes data which we collected from 5 telescopes in which 2 are in India, 1 in Greece, 1 in Bulgaria and 1 in Serbia.

2.1 Part 1.

XMM-Newton Observations and Data Reduction

2.1.1 XMM-Newton Telescope

The X-ray Multi-Mirror space observatory *XMM-Newton* named in honour of Sir Isaac Newton. Figure 2.1 shows the Artist's impression of *XMM-Newton* spacecraft. It is an

European Space Agency (ESA) mission that is the part of the “Horizon 2000” programme [Jansen et al. \(2001\)](#).



Figure 2.1 Artist's impression of XMM-Newton space observatory in orbit around the Earth. Image courtesy of ESA/D. Ducros

The spacecraft was successfully launched on December 10, 1999 at 14:32 GMT by the European launcher rocket Ariane-504 from the launch pad Kourou (French Guiana) and placed in an eccentric orbit lasting 48 hours. Its perigee and apogee are about 7000 km and 11400 km, respectively from Earth. The eccentric orbit provide a long continuous coverage of the observation of a target field. It is the largest scientific satellite ever launched by the ESA, with a length of 10 meters to accommodate the X-ray imaging system with total mass of 3800 kg. *XMM-Newton* space observatory carries two distinct types of telescopes: three Wolter type-I X-ray telescopes, with different X-ray detectors in their foci and a 30 cm optical/UV telescope with a micro channel plate pre-amplifier Charge Coupled Device (CCD) detector in its focal plane. *XMM-Newton* provides simultaneous observing facility in X-ray and optical/UV window of electromagnetic spectrum. It has three types of scientific instruments on board:

1. The European Photon Imaging Camera (EPIC), for X-ray imaging, spectroscopy and photometry.

2. The Reflection Grating Spectrometer (RGS), for high-resolution X-ray spectroscopy and spectro-photometry.
3. The Optical Monitor (OM), for optical/UV imaging and spectroscopy.

Figure 2.2 is showing the arrangement of the instruments on the XMM-Newton satellite. All the scientific instruments operate simultaneously and are co-aligned. The basic characteristics which make the XMM-Newton a unique space observatory are: simultaneous MW observing facility; high sensitivity; good angular resolution; moderate and high spectral resolution; and long continuous target visibility.

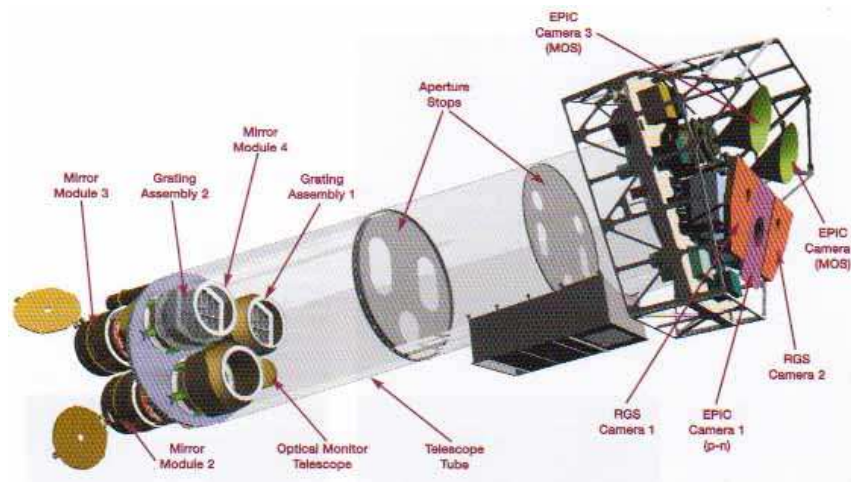


Figure 2.2 Image showing the XMM-Newton scientific instruments. The X-ray telescopes, two with Reflection Grating Arrays, are visible at the lower left. At the right end of the assembly, the focal instruments are shown: The EPIC-MOS cameras with their radiators (black/green "horns"), the radiator of the EPIC-pn camera (violet) and those of the (light blue) RGS receivers (in orange). The black box at the bottom of the bus is the out gassing device. Image courtesy of Dornier Satellitensysteme GmbH and ESA.

2.1.2 X-ray Telescope

A normal telescope works by reflecting and focusing light technique. But X-rays have such high energy that they pass through most of the materials, making reflection impossible. To resolve the reflection problem in X-ray telescopes, mirrors are arranged in such a way that the incoming X-rays graze off of the mirrors, like a stone skipping on water.

The shape and highly-polished surfaces of the mirrors make sure that the incoming X-rays are focused into a beam when they fall on the detectors. XMM-Newton have three identical, co-aligned and tube-like X-ray telescopes with a focal length of $f = 7.5m$ and field of view of $\sim 30'$ ((see Table 2.1 on page 32 [de Chambure et al., 1999](#)); [Aschenbach \(2002\)](#)). Figure 2.3 shows the technical drawing of one of the X-ray telescope.

Table 2.1 Parameter details of an XMM-Newton X-ray telescope ([Jansen et al. \(2001\)](#)).

Telescope focal length	7500 mm
Number of mirrors per telescope	58
Outer mirror radius	350 mm
Inner mirror radius	153 mm
Axial mirror length	600 mm
Outer mirror thickness	1.07 mm
Inner mirror thickness	0.47 mm
Minimum packing distance	1 mm
Mirror substrate material	Nickel
Reflective coating	Gold

Each telescope consist of 58 Wolter type-I mirrors which are nested in a coaxial and confocal configuration. This design provide a large collective area over a wide energy band. The thin mirror shells made of nickel having thickness $\sim 1mm$. The inner side of each shell is coated by gold with surface roughness of $\sim 3\text{\AA}$. Gold is used for surface coating because it improve the X-ray reflectivity due to its large atomic number. The range of mirror grazing incidence angles lie between 17 and 42 arcmin. The entrance aperture of 58 mirrors of each telescope are bonded by the 16 spokes of a single spider as shown in figure 2.4. An electron reflector is fixed in the exit aperture which produces a circumferential magnetic field to averts low energy electrons reflected by the mirrors reaching the focal plane detectors. The basic characteristics of each X-ary telescope are: good image quality, large effective area and high straylight rejection efficiency. The total effective area of the combination of three X-ray telescopes of *XMM-Newton* is $A_{eff} = 4300 \text{ cm}^2$ at the energy 1.5 keV and $A_{eff} = 1800 \text{ cm}^2$ at 8.0 keV. *XMM-Newton* is ideal for discovery, and imaging & spectral studies of faint sources, particularly in the energy range of 2.0 – 10.0 keV.

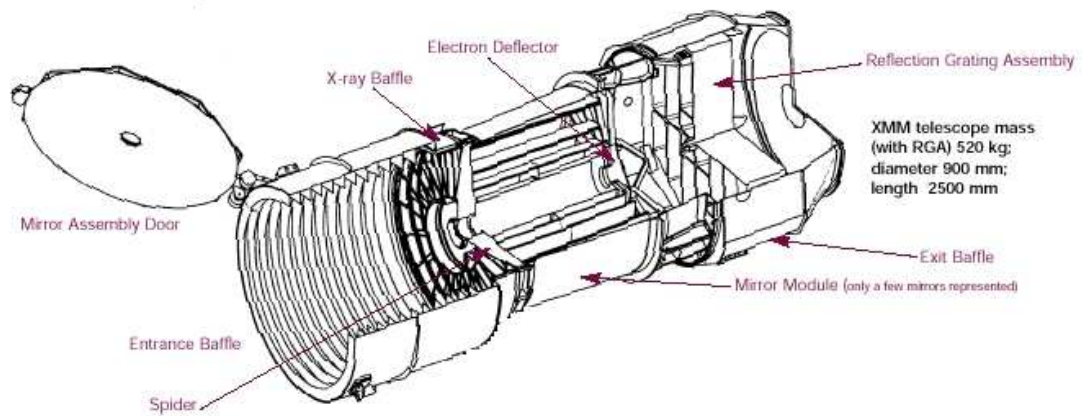


Figure 2.3 Technical drawing of one of the XMM-Newton X-ray telescope. Image courtesy of ESA

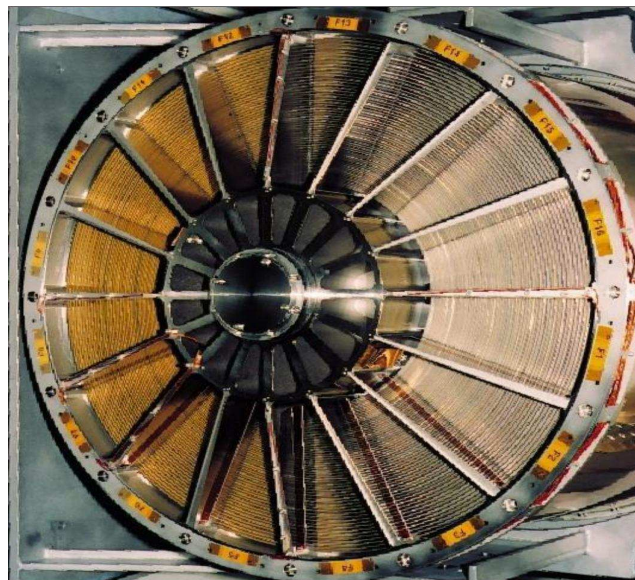


Figure 2.4 The XMM-Newton mirror module during integration. One spider carrying a full set of 58 flight mirror shells is visible. Image courtesy of Dornier Satellitensysteme GmbH and ESA.

2.1.3 The European Photon Imaging Camera (EPIC)

The X-ray imaging detectors are the most important scientific instruments placed on board to the *XMM-Newton*. These detectors are placed on the focus point of the three X-ray telescopes to gather information about the energy, position and time of detection simultaneously. The complete EPIC device consists of two identical MOS (Metal Oxide

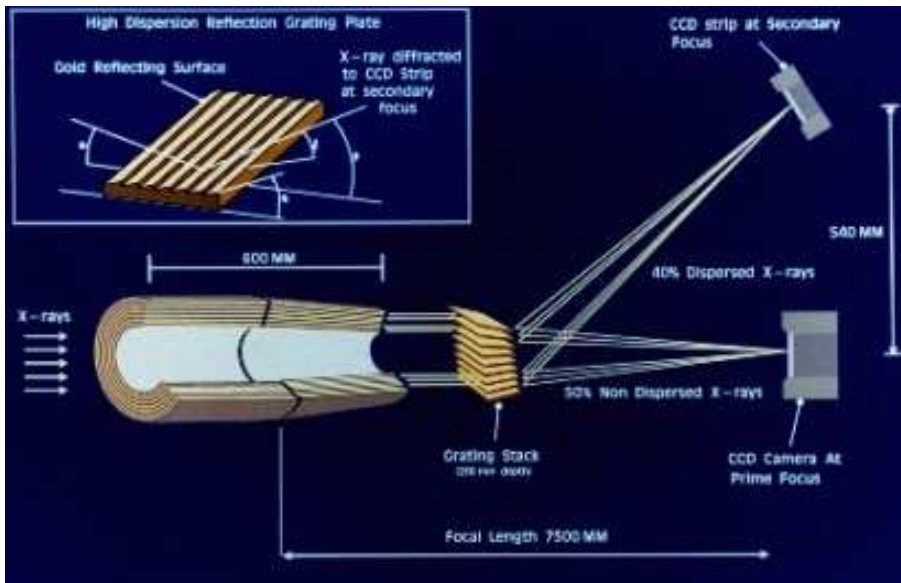


Figure 2.5 Image shows the schematic of X-rays path in the XMM-Newton Wolter type I telescope with EPIC camera in its primary focus and the RGS detectors in the secondary focus.

Semiconductor) CCD (Charge Couple Device), one pn-CCD (p-type/n-type semiconductor) and a EPIC Radiation Monitor System (ERMS). The MOS cameras have been developed in the French and British collaboration and the pn camera have been developed in the collaboration between Institut für Astronomie und Astrophysik, Tübingen (IAAT) and Max-Planck-Institut für extraterrestrische Physik (MPE). The MOS detector share the incoming X-ray flux with the RGS detector due to its geometrical arrangement as shown in Figure 2.5. The MOS-CCDs are the modified version of the optical CCDs suitable to register X-ray photons, but the pn-CCD is a new device developed for the X-ray astronomy.

Two X-ray telescopes of *XMM-Newton* are equipped with EPIC MOS CCD array and the third carries a different CCD array called as EPIC pn. EPIC cameras provide a unique facility to perform extremely sensitive imaging observations over a field of view of $30'$ in energy range of 0.15 to 15 keV, moderate angular ($\sim 6''$ FWHM; $\sim 15''$ HEW) and spectral resolution ($E/\Delta E \sim 20-50$). A comparative study of all EPIC-MOS and EPIC-pn CCDs parameters are given in table 2.2.

A filter wheel was fixed in front of each EPIC camera which has six different filter positions. Four positions of filter wheel are equipped with aluminized filters of different

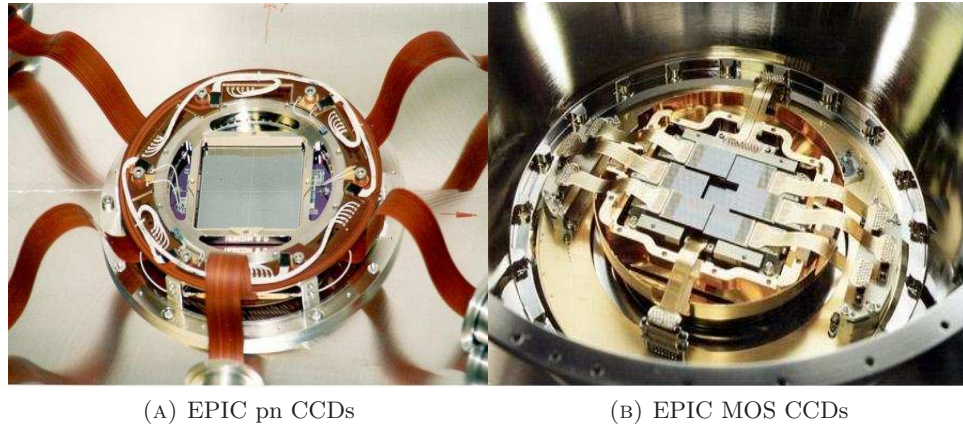


Figure 2.6 Left panel shows the image of the 12 CCDs of the EPIC pn detector. Its spatially uniform detector quality over the entire FOV is realized by the monolithic fabrication of twelve 3 x 1 cm pn-CCDs on a single wafer. The four individual quadrants have each three pn-CCD subunits. Image courtesy of MPI-semiconductor laboratory, MPE, Astronomisches Institut Tübingen, Germany and ESA. Right panel shows the photograph of the array of 7 CCDs of an EPIC MOS camera. The two MOS cameras are arranged on the spacecraft focal plane bulkhead so that the CCDs are orthogonal. Image courtesy of Leicester University, University of Birmingham, CEA Service d’Astrophysique Saclay and ESA

Table 2.2 Parameter details of EPIC-pn and EPIC-MOS CCDs as given by XMM-Newton Users handbook 2009.

Parameters	EPIC-pn	EPIC-MOS
Number of CCDs	Twelve	Seven
Number of pixels in a single CCD	64×200	600×600
Pixel size(μm)	150×150	40×40
Field of view(arcmin)	27.5	33.5(maximum)
PSF(FWHM/HEW)(arcsec)	6/15	5/14
Time resolution of the full field(s)	0.056	3
Timing resolution(ms)	0.04	1.0
Bandpass(keV)	0.15-15.0	0.15-12.0
Sensitivity($\text{erg cm}^{-2}\text{s}^{-1}$)	$\sim 10^{-14}$	$\sim 10^{-14}$
Energy resolution[1keV/6.4keV](eV)	80/140	70/135
Quantum efficiency[0.5/6.4/8.0 keV]	88%/99%/97%	45%/87%/65%
Operating temperature($^{\circ}\text{C}$)	~ -120	~ -80

thickness (one “thin” two “medium” and one “thick” filter) which provide facility to filter out the low energy (e.g. IR, optical and UV) radiations and observe a X-ray source in different (e.g. low, moderate and high) flux states, one is the fully opened position without any blocking filter and the last one is the fully blocked position with a thick ($\sim 1\text{mm}$) aluminium layer blocking all radiations and protecting the EPIC detector from being damaged by high energy radiations mainly originating from Van-Allen radiation belt. The shot noise is enhanced by low energy radiations, a shift in energy scaling ($\sim 3.6\text{eV}$) which change the energy resolution. All EPIC cameras are well shielded with 3cm thick aluminium sheet. The radiation monitor measure the rate of particle radiation affecting the satellite and also provide information about the particle radiation background near EPIC detector. The solar flare is the main source of high level of particle background. At high level of background radiation monitor serves as a warning device for sensitive EPIC CCDs and can cause the filter wheel to move into the block filter position to avoid damages on the EPIC CCDs. The pn camera CCDs can be operated in full frame, extended full frame and large window mode which are common modes in all quadrants. A single CCD (CCD0 in quadrant 1) can be used for small window, timing and burst modes. The parameters details and other specification of EPIC-pn detector in different mode of observation is given in table 2.3.

2.1.4 The Optical Monitor(OM)

The Optical/UV Monitor Telescope (XMM-OM) is a standalone instrument that is mounted on the mirror support platform of *XMM-Newton* alongside the X-ray mirror modules (Jansen et al. (2001)). The XMM-OM provides coverage between 170 nm and 650 nm of the central 17×17 arcmin² region of the X-ray field of view with an angular resolution of one arcsec, permitting routine MW observations of *XMM-Newton* targets simultaneously in X-ray and UV/optical bands. It achieve an impressive imaging sensitivity compared to a similar instrument on the ground based telescopes because the low value of sky background in space. The OM consists of a telescope module and a separate digital electronics module which has two identical units for redundancy as shown in figure 2.7.

Table 2.3 Parameters of the six standard readout modes as implemented in-orbit. The energy flux in the last column was derived in the energy band from 0.1 keV to 10 keV with the assumption of an unabsorbed power law with photon index 2.0, observed with thin filter (Strüder et al. (2001)).

Mode	Field of view(FoV) In pixel format In arcminute	Time resolution in ms	Out of time (OOT) events in %	Life time with OOT events in	Brightest point source for XMM in counts per sec % in $\text{erg cm}^{-2} \text{s}^{-1}$
Full frame	398×384 27.2×26.2	73.3	6.2	99.9	6 8.1×10^{-12}
Extended full frame	398×384 27.2×26.2	199.2	2.3	100	for extended sources only
Large window	198×384 13.5×26.2	47.7	0.15	94.9	9 1.2×10^{-11}
Small window	63×64 4.3×4.4	5.7	1.1	71.0	104 1.4×10^{-10}
Timing	199×64 13.6×4.4	0.03	100	99.5	4000 5.9×10^{-9}
Burst	20×64 1.4×4.4	0.007	Depends on PSF	3.0	60000 8.1×10^{-8}

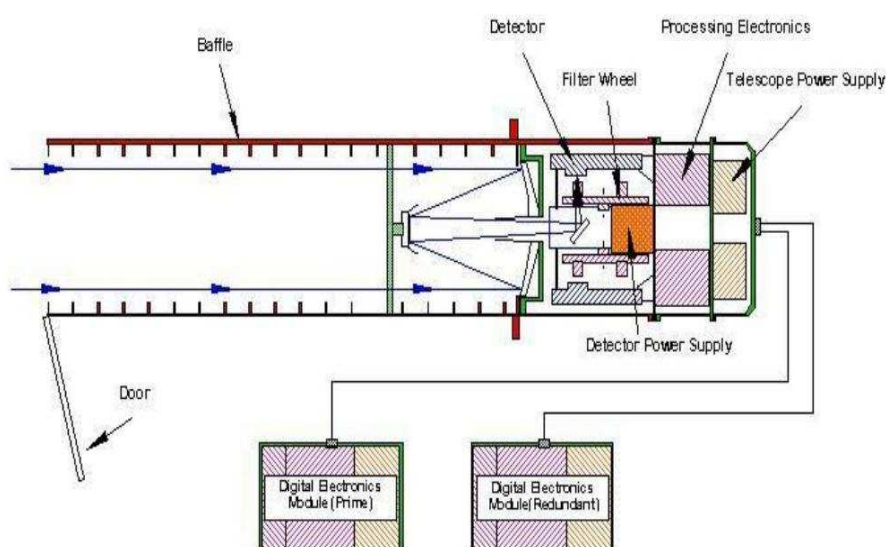


Figure 2.7 A schematic diagram of the Optical Monitor(OM) telescope aboard XMM-Newton satellite. The OM consists of a 30 cm Ritchey-Chretien arrangement of mirrors that reflect light through a filter wheel to a detector. The telescope’s three mirrors all sit inside a baffle. Image courtesy of MSSL, UK and ESA.

The telescope module contains the telescope optics, detectors, detector processing electronics units and power supply. The digital module contains instrument control unit and data processing unit, which manage communication with spacecraft and commanding of the instrument and pre-processing the data from the instrument before it is telemetered to the ground, respectively. The XMM-OM uses a Ritchey-Chretien telescope design modified by field flattening optics built into the detector window (Mason et al. (2001)). In the telescope module $f/2$ primary mirror of 0.3 m diameter feeds a hyperboloid secondary mirror, which modify the focal ratio to 12.7, with a focal length of 3.8 m. There are two distinct detector chain for redundancy. A 45° flat mirror located behind the primary mirror can rotate the incoming light towards one of the two redundant detector chain. Each detector chain has a filter wheel and detector system. The filter wheel has eleven apertures, in which one is blanked off to serve as a shutter, prevent light reaching to the detector. Another seven filters locations are filled with seven lenticular filters, in which six filters constitute a set of broad band filters for color discrimination in the UV and optical bands and their wavelength bands lies between 180 to 580 nm range, the list of filters and their wavelength bands are mentioned in table 2.4. The seventh filter is a “white light” filter which transmits light over the full range of the detector to provide

Table 2.4 The OM filter table with their wavelength bands in nanometre(nm) and the preliminary zero points. The filters are arrange in the order that they occur in the filter wheel. The zero points magnitude updated on October 2000 after the ground based observation programme become operational ([Mason et al. \(2001\)](#)).

Filter	Band wavelength(nm) (nm)	Zeropoints (magnitude)
Blocked		
V	510-580	18.11
Magnifier	380-650	
U	300-390	18.24
B	390-490	19.28
White	150-500	
Grism 2	290-500	
UVW1	245-320	17.37
UVM2	205-320	16.02
UVW2	180-225	15.17
Grism1	200-350	

maximum sensitivity to a point source ([Mason et al. \(2001\)](#)). In remaining three filter positions, two contains grisms, one optimized for optical and the other for UV range, and the last one contains a $\times 4$ field expander or magnifier to give high spatial resolution in a 380-650 nm range of the central portion of the field of view.

The XMM-OM detector is a compact image-intensified photon counting instrument. Each of the XMM-OM detectors consist of a microchannelplate-intensified CCD ([Fordham et al. \(1992\)](#)) with 384×288 pixels in which 256×256 pixels are usable for science observation. Incoming photon events are centroided to $1/8$ th of a CCD pixel to yield 2048×2048 pixels on the sky. Each CCD pixel has a size of about 0.4765 arcsec square on the sky. In literature, to avoid confusion, size of observing window is expressed in terms of centroided pixels. S-20 photocathode is deposited inside of the detector window and convert incoming photons into photoelectrons. These photoelectrons are proximity focussed into a microchannelplate stack, which amplifies the signal by a factor of 10^5 . Before the resulting photoelectrons are converted back into the photos by a P46 phosphor screen, light from phosphor screen is transmitted through a fibre taper which adjust for the difference in physical size between fast-scan CCD and microchannelplate stack used to detect the photons. The dark noise of the detector is very low.

2.1.5 XMM-Newton data reduction procedure

The Science Analysis System (SAS) developed and maintained by the Survey Science Center (SSC) and Science Operation Center (SOC) at ESA. SAS is a collection of tasks, scripts and libraries, specifically designed to reduce and analyze data collected by the *XMM-Newton* satellite. The *XMM-Newton* data are available in two formats:

- 1. Observation Data File (ODF):** These files contain raw data of observations in Flexible Image Transport System (FITS) format.
- 2. Pipeline Processing System (PPS):** These files contain a collection of validated, top-level scientific products which include: calibrated photon event files, source lists, multi-wavelength images, and cross-correlation products generated at the SSC.

We used SAS version 11.0.0 with the latest calibration files to reduce the *XMM-Newton* data of the TeV blazar PKS 2155-304. SAS is necessary to extract standard (spectra, light curve, etc.) even if we start with pipeline processed data products (PPS). Moreover, SAS provides a facility to reproduce the pipeline reduction procedure using ODF files as input and to get the PPS products. It is recommended to start with ODF data rather than PPS data. When there is change in the SAS software and/or instrument calibration files, the ODF will be processed by SSC pipeline to get the new PPS products. SAS is not designed for higher level scientific analysis such as spectral fitting and temporal analysis. But SAS creates detector response and barycentric corrected event timing information. Extensive EPIC and OM source-detection softwares are included in SAS. The SAS product files are in OGIP FITS standard format, therefore any high-level analysis package used in high-energy astrophysics should be theoretically capable of processing *XMM-Newton* data (The XMM-Newton ABC guide 2015). The procedure applied for data analysis of *XMM-Newton* observations are described below.

2.1.5.1 XMM-Newton Science Archive

All observations taken with *XMM-Newton* are made publicly available through the *XMM-Newton* Science Archive (XSA). The XSA provides simple and flexible access to data from EPIC and OM catalogues. Proprietary XMM-Newton data can be searched but can not be download by anyone except the Principal Investigator (PI) of the project. After the proprietary period (one year) is over, it will be available in public archive. An observation can be searched on XSA website¹ using many different parameters e.g. target name, coordinates of target, observation date, observation ID etc. Both ODF and PPS files are available for download. The data files can be filtered before download which help us to reduce the file size. The data can be retrieved either by direct download or ftp. In this thesis we have used public archive *XMM-Newton* data in ODF format of the blazar PKS 2155–304.

2.1.5.2 Standard data reduction procedure

XMM-Newton data analysis requires extensive standard calibration files which are available under a Current Calibration File (CCF) directory. Information on the CCF and instructions for downloading/mirroring the files can be found under the SOC *XMM-Newton* calibration page². Standard initial processing of the blazar PKS 2155–304 was performed by using XMM-Newton Science Analysis Software (XMMSAS) version 11.0.0. The basic steps of XMM-Newton data reduction using XMMSAS are summarized as below:

- 1. SAS environmental parameters and invocation:** There are a few parameters which need to be set for the proper operation of SAS. Two are taken care by the initialization script, SAS_DIR and SAS_PATH. Two parameters, listed below still need to be set before SAS invoked.

SAS_CCFPATH, sets the directory path to the CCF data.

SAS_ODF, sets the directory path to the ODF files which we wants to process.

¹<http://nxsa.esac.esa.int/xsa>

²http://xmm2.esac.esa.int/external/xmm_sw_cal/calib/index.shtml

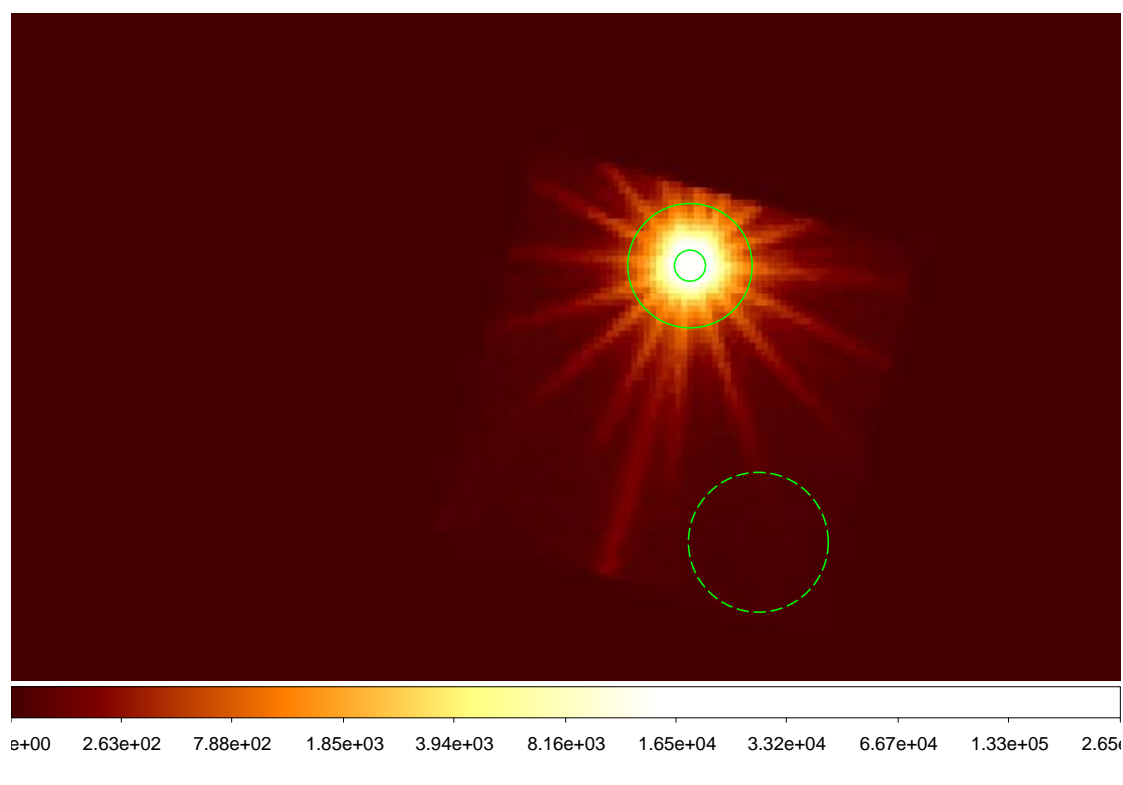


Figure 2.8 XMM-Newton PN Small Window(SW) mode image of PKS 2155-304 on 30 November 2005. The source region is an annulus region with radius 10-40 arcsec.

- 2. Generating a Calibration Index File (CIF):** The XMM-Newton ODF files contain information about observation date, instrument used, exposure mode, filters, exposure time, etc. To calibrate an ODF file, first we need to identify the CCF file which will be used in the calibration. The task “cifbuild” create a CIF file which determines the set of CCF needed for each observation. It is necessary to set the SAS environment parameter SAS_CCF again with CIF path and file name.
- 3. Generating the ODF summery file:** The task “odfingest” create a ODF summery file with data extracted from the instrument housekeeping data files and the calibration database. It is essential for reprocessing the ODF files with the pipeline tasks as well as for other many tasks. It is necessary to set the SAS_ODF parameter again with path and name of the ODF summery file.

- 4. Obtain the calibrated data (event list):** Run the SAS tasks “emchain” or “emproc” (to produce calibrated and concatenated photon event files for the EPIC-MOS camera) and “epchain” or “epproc” (to do the same for the EPIC-pn camera). The calibrated photon event files can be directly use to generate scientific products (i.e. images, spectra, light curves, etc.) through the SAS tasks “evselect” or “xmmselect”. If an observation ID has more than one exposure, a specific exposure can be accessed using the exposure parameter. The calibrated photon event file corresponding to all exposures which contains in a single observation is produced using one time execution of the tasks “emproc” and “epproc” where the SAS has been initialized.
- 5. Generating Good Time Interval (GTI) event list:** Before generating a GTI event list file, we checked for the high soft proton background period which are caused by solar activity. It is done by generating a hard band light background curve in the energy range 10-12 keV and then we define GTI for those times where the hard band count rate was less than 0.4 ct sec^{-1} (for EPIC-pn data). GTI event list is generated by SAS task “tabgtigen” which filter out the interval of flaring particle background from the calibrated event list.
- 6. Filtering the event file:** The SAS task “evselect” is used for filtering event file, as well as generating image, light curve and spectra. The standard filtering criteria applied on the event file is based on three parameters: event patterns, quality flag, and energy range. The event pattern parameters refer the number and pattern of pixels triggered for each event. The values of pattern parameter is 0 (for single pixel events), 1-4 (for double pixel events) and 5-12 (for triple and quadruple pixel events). We have used only single and double pixel events in this work. The quality flag parameter value provides a bit encoding of various conditions (e.g. near hot pixels or outside the field of view). (Flag=0) is the most conservative screening criteria which is used when serious spectral analysis to be done. Finally, only events in the energy range 0.3–10 keV with quality flag=0 are used in this thesis work.

7. Source and background region selection in the image: After filtering the event file, we run the SAS task “evselect” for generating a X-ray image of the source on the active CCDs. Figure 2.8 shows the EPIC-pn image of the blazar PKS 2155–304 in the Small Window (SW) mode. In imaging modes, source region is circular which consist of the source PSF determined from the image. The continuous outer circle in the annulus region shown in figure 2.8 is the selected source region which is used to generate a filtered event file for source region with “evselect” task. The background region is the maximum circular region on the CCD chip where source was located and was least affected from source counts in the case of EPIC-pn data. The dashed circle shown in figure 2.8 is the selected background region which is used to generate a filtered event file for background region.

8. Correcting from possible photon pile-up: Event pile-up may be observed depending on how bright the source and in which mode the EPIC detector is used. Pile-up occurs whenever a X-ray source is too bright for the selected read-out mode so that the incoming X-ray strike the two neighbouring pixels or the same pixel in the CCD more than once in a read-out cycle. Pile-up is like an overexposure effect which can be occurred in two ways (e.g. pattern pile-up and energy pile-up).

Pattern pile-up: It occur when more than one photon is detected in two or more adjacent pixels during a single read-out cycle. During the read-out, the electronics can not distinguish whether signals in adjacent pixels originate from one or more photons, thus, two or more photons are erroneously combined to an individual event of higher pattern type. In such cases two adjacent individual photons are erroneously combined to a double event whose energy is equal to the sum of the individual energies of the incoming photons.

Energy pile-up: It occur when more than one photons hit the same pixel during a single read-out cycle. In that case the read-out electronics can not distinguish whether the signal in a pixel originates from one or more photons, thus a single event of erroneous energy is read and is equal to the sum of the individual energies of the incoming photons.

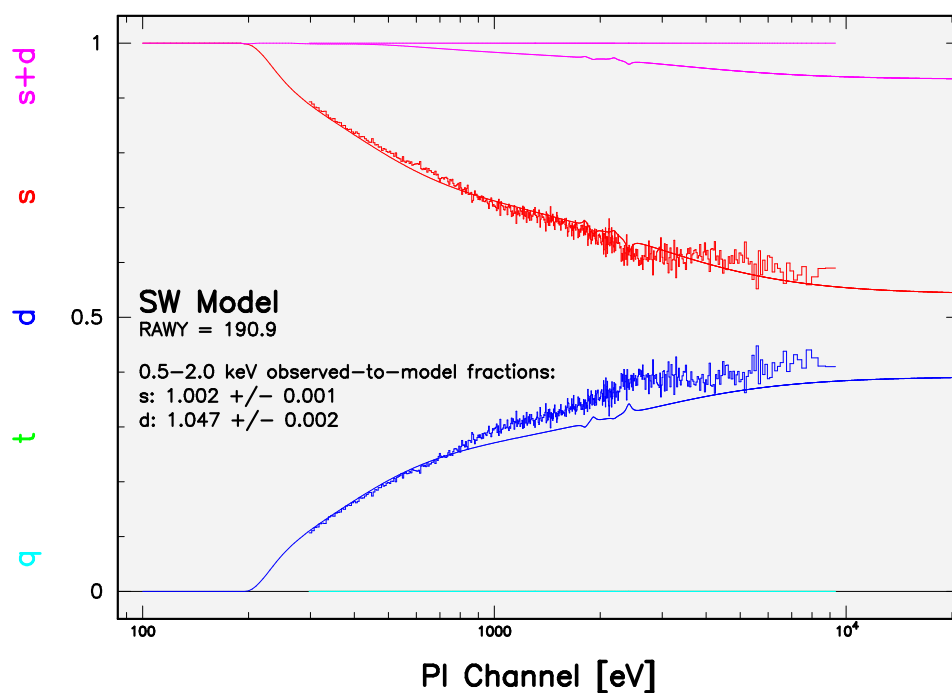
Pile-up affect the source spectra in three following ways:

Photon loss: In both pile-up pattern photons count rate will be under estimated.

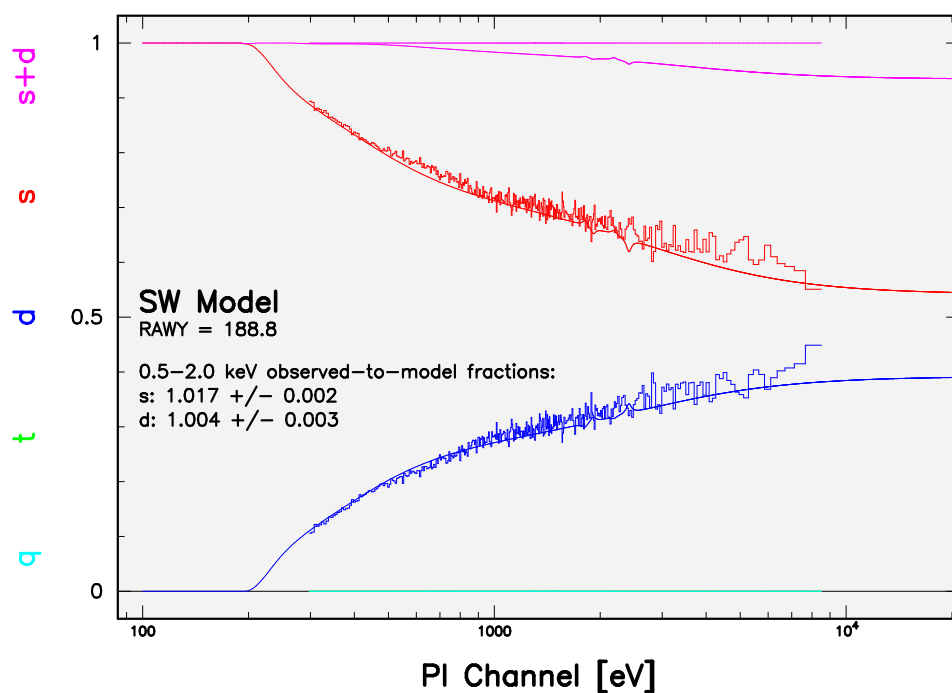
Pattern migration: The expected events pattern distribution is migrated from one to another due to the pile-up effect. In pattern pile up, double events are over estimated but in case of energy pile-up the single events are over estimated.

Energy distortion: The energy spectra of the source will appear to be harder than it's actual value because the photons energy are over estimated in both types of pile-up patterns.

Possible photon pile-up in the source spectra is investigated by running the SAS task “epatplot” on the source region event file, which produce a ‘postscript’ file displaying the observed versus expected pattern distribution. The top panel of figure 2.9 shows the “epatplot” output for a 40 arcsec radius circular region centred on PKS 2155-304 in SW mode shown in figure 2.8. The output of “epatplot” displays the energy dependent fraction of single and double pixel events compared with a predicted model for no pile-up. The source spectrum will be affected by pile-up if the expected distributions are significantly discrepant from the observed ones. The task “epatplot” also calculates two diagnostic numbers which may be used to evaluate the presence of pile-up in the source spectra. In the absence of pile-up, the 0.5 - 2.0 keV (default range) observed-to-model singles and doubles pattern fractions ratios should both be consistent with 1.0 within statistical errors (1σ error is given). If pile-up is present, the singles pattern ratio will be smaller than 1.0 and the doubles ratio will be larger than 1.0. These ratios are printed on the console and displayed on the plot (The XMM-Newton ABC guide (2015)) as shown in the figure 2.9. The calculated observed-to-model fractions for single and double pixel events within a certain energy range can be incorrect, therefore, the most efficient method to check the presence of pile-up is the graphical agreement of the observed (histogram) and expected (solid line) pattern distribution shown in the figure 2.9. The upper panel of figure 2.9 shows that the double pixel events fraction is higher than the expected value and the single pixel events fraction is smaller than the expected value which clearly indicate the presence of pile-up in



(A) Before pileup correction



(B) After pileup correction

Figure 2.9 The energy dependent fraction of single (red) and double (blue) pixel events from SW mode observation. In top panel pile-up is evident by divergence of the single and double pixel event pattern distribution from the model prediction for no pile-up.

the source spectra. The method to reduce pile-up in a given observation data is to excise the core of the PSF, up to a radius where the pile-up fraction becomes negligible. In this method we have extracted the filtered event lists of annular regions around the centroid position excising more and more of the core of the PSF until the observed pattern distributions match the expected one. Figure 2.8 shows a source centred annulus region with a radius of 10-40 arcsec, we have extracted the filtered event lists of this annular region to remove the pile-up effect from the source spectra. The bottom panel of figure 2.9 shows the output of task “epatplot” for the same SW mode of PKS 2155-304 observation, but from events in a source centred annulus region with radius of 10-40 arcsec. Figure 2.9 (bottom panel) clearly shows single and double pixel events pattern distribution match with the expected one.

8. Generating light curve: Light curve is extracted from source and background filtered event files using SAS task “evselect”. The size and co-ordinates of the source and background regions were obtained from the image of filtered event file by displaying FITS file on image viewer e.g. ‘ds9’. The light curve generated in such a way that is corrected for various effects affecting the detection efficiency, such as vignetting, PSF variation, bad pixels, quantum efficiency variation, as well as for variations affecting the stability of the detection within exposure, like GTIs and dead time. All these effects can affect source and background light curves in a different way, therefore, the background subtraction has to be done accordingly. A SAS task “epiclcorr” which requires source and background light curves as input files and perform all of these corrections at once.

9. Generating spectral files and spectra (e.g. ancillary and instrument response files), We have generated all the spectral files using SAS task “xmmselect” GUI window method. To extract the source spectrum, we loaded the cleared event file in “xmmselect” task. After execution of “xmmselect” task, GUI window will open. We made an exposure image which displayed automatically in a ds9 window. We select the source and background region whose spectrum we wish to extract. By using “OGIP Spectral Products” will generate four files (source, background,

ancillary and instrument response files). The “specgroup” command combined the four spectral files and generate the binned source spectra. The source spectral file can be loaded in the spectral fitting software ‘XSPEC’ for spectral fitting. We used ‘XSPEC’ version 12.8.0 to fit the spectra of the blazar PKS 2155–304.

10. **Count rate to flux conversion:** We used “effluxer” SAS task which converts X-ray EPIC spectrum generated by “evselect/xmmselect” from the usual counts versus instrument channels space into physical unit ($\text{erg cm}^{-2} \text{s}^{-1} \text{keV}^{-1}$ Vs keV). The task “effluxer” corrects the energy redistribution and the effective area of the telescope, for any combination of scientific modes and filters. For Spectral Energy Distribution (SED) analysis, we have converted the X-ray count rate of EPIC-pn detector into the flux density ($\text{erg cm}^{-2} \text{s}^{-1}$).

2.1.5.3 XMM-Newton OM data reduction procedure

1. **OM data reduction:** XMM-Newton OM detector can be operated in three modes of observation (e.g., imaging, fast and grism mode). Each mode of observation has dedicated commands to reprocess the data: “omichain”, “omfchain”, and “omgchain” for imaging, fast, and grism mode data, respectively. Each command is not a single command but it is a metatask that call several procedures that are used to prepare the data for processing, make and apply flat field images, and detect sources. The command “omichain”, and “omfchain” also calculate the instrumental magnitudes of sources, find the position of the sources (in equatorial coordinate system), and produce a sky image; “omgchain” produces a spectrum of the sources. Therefore each chain command apply all necessary corrections, so no further processing or filtering is required. We used “omichain” command to reprocess the imaging mode OM data for all filters in UV/optical bands.
2. **Count rate to flux conversion:** The count rate corresponding to different OM filters are converted into flux ($\text{erg cm}^{-2} \text{s}^{-1} \text{\AA}$) by multiplying with conversion factor corresponding to each filter given on page 158 of Users Guide XMM-Newton Science Analysis System 2011.

2.2 Part 2.

Ground Based Optical Observations and Data Reduction

2.2.1 Optical Telescopes

In this dissertation, we have done optical studies of three TeV blazars (PKS 1510–089, PG 1553+113 and Mrk 501). The optical photometric observations during June 2012 to September 2014 of the three TeV blazars were carried out using five telescopes around the world. Among which two telescopes are in India operated by Aryabhata Research Institute of observational sciencES (ARIES), Nainital, India. One is the 1.04m Sampuranand Telescope (ST) having Ritchey-Chretien (RC) optics with a f/13 beam equipped with Johnson UBV and Cousins RI filters. The other is the 1.3m Devasthal Fast Optical Telescope (DFOT) which is a fast beam f/4 telescope with a modified RC system equipped with broad band Johnson-Cousins B, V, R, I filters. DFOT provides a pointing accuracy better than 10 arcsec RMS (Sagar et al. (2011)). Further details of both telescopes are given in Table 2.5 (telescopes A and B, respectively). We also employed the 1.3m RC telescope of Skinakas Observatory³, of the University of Crete, Greece. Technical parameters and chip specifications for the cameras used are given in Table 5 (Telescope C). All frames were exposed through a set of standard Johnson-Cousins BVRI filters. In addition to above telescopes, we carried out photometric observations of the blazars using the 60 cm Cassegrain telescope of Belogradchik Astronomical Observatory (AO), Bulgaria which is equipped with standard UBVRI filter sets. Instrumental details are summarized in Table 5 (Telescope D). Observations were also taken with 60cm Cassegrain telescope, which is located on Vidojevica mountain in South Serbia, through Johnson-Cousins BVRI standard filter set (Telescope E). The details of these five telescopes, detectors and other parameters used are given in Table 2.5, filter details in Table 2.6, and picture of telescopes in figure 2.10.

³Skinakas Observatory is a collaborative project of the University of Crete, the Foundation for Research and Technology – Hellas, and the Max-Planck-Institut für Extraterrestrische Physik.

Table 2.5 The basic parameters details of ground based optical telescopes and instruments used in this work.

Site:	A	B	C	D	E
Scale:	0.535/pixel	0.37/pixel	0.2825/pixel	0.330/pixel ^a	0.465/pixel
Field:	18 × 18	13 × 13	9.6 × 9.6	16.8 × 16.8	15.8'x15.8'
Gain:	1.4 e ⁻ /ADU	10 e ⁻ /ADU	2.687 e ⁻ /ADU	1.0 e ⁻ /ADU	1.25 e ⁻ /ADU
Read Out Noise:	4.1 e ⁻ rms	5.3 e ⁻ rms	8.14 e ⁻ rms	8.5 e ⁻ rms	3.75 e ⁻ rms
Typical seeing :	1.2to 2.0	1to 2.8	1to 2	1.5to 3.5	1to 2

A : 1.30 meter Ritchey-Chretien Cassegrain optical telescope, ARIES, Nainital, India

B : 1.04 meter Sampuranand Telescope, ARIES, Nainital, India

C : 1.3-m Ritchey-Chretien telescope at Skinakas Observatory, University of Crete, Greece

D : 60-cm Cassegrain telescope at Astronomical Observatory Belogradchik, Bulgaria

E : 60-cm Cassegrain telescope, Astronomical Station Vidojevica - ASV

^a With a binning factor of 1 × 1

Table 2.6 The details of central wavelength and band width of broad band optical filters.

Filter	Central wavelength(nm) λ (nm)	Bandwidth $\Delta\lambda$ (nm)
U	360	60
B	440	90
V	550	90
R	640	160
I	800	150

2.2.2 Optical Photometric Data Reduction

The raw CCD image frames stored from observations from ground based optical telescopes need to be processed. The raw data have combined effect of photons collected from the source, atmosphere, telescope, detector and its electronics. Unstable sky condition and variable seeing degrade image quality. The mechanical and optics system of telescope can also additionally degrade the image quality. In addition to these, the detector CCD has thermal noise and pixel to pixel non-linearity. So, extracting the actual photons detected from the source, need the removal of effect caused by the atmosphere, telescope and detector.

To extract data for scientific use, we need the processing of the raw observational data which is we done in three following steps: **(I)** pre-processing, **(II)** processing, and **(III)** post-processing. We will discuss below these three steps in more detail.

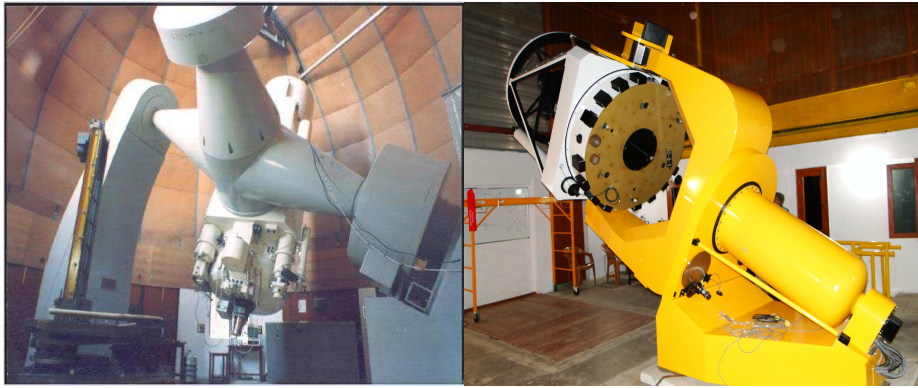
I. Image Pre-processing

Image preprocessing on the raw data is done for removal of CCD detector effect. For pre-processing we use standard routines in the package IRAF⁴ The steps involves are following:

(a) Bias Subtraction

In bias frames, CCD exposure is zero second with closed shutter i.e. CCD chip is simply read out. The bias frams is basically thermal noise of the detector which allow us to

⁴Image Reduction and Analysis Facility (IRAF) is distributed by the National Optical Astronomy Observatories, which are operated by the Association of Universities for Research in Astronomy, Inc., under cooperative agreement with the National Science Foundation.



(A) 1.04 m ST, ARIES

(B) 1.30 m DFOT, Devasthal



(C) 1.3 m SOUC, Crete

(D) 0.6 m AOB, Bulgaria



(E) 0.6 m ASV, Vidojevica

Figure 2.10 Picture of Five ground based optical telescopes

determine the underlying noise (DC offset) level within each data frame. The bias frame has almost a constant value over entire CCD chip. In an observing night, we take bias frame with almost regular interval and median combined them to make a master bias frame for a specific observing night. This master bias frame will be subtracted from all source image frames as well as all sky flat image frames.

(b) Flat Fielding

Flat image frames are collected for correcting the pixel-to-pixel inhomogeneity due to manufacturing of CCD. All the pixels of a CCD do not necessarily have the same response, though ideally they are supposed to have the same sensitivity. To correct the non uniform sensitivity of pixels of CCD detector and make all pixels almost equally sensitive, this is a very important task. We collect image frames of uniform sky background without stars in dawn and dusk time in all filters. We make sure to collect at least 3 flat image frames in each filter on a particular observing night. We subtract master bias frame of a particular observing night from all flat frames and then for individual filter, we use median combine to make master flat frame of that filter. The same process is repeated for all filters and master flat frames are generated in all filters in which observations were carried out. Master flat frame's are normalized which gives almost equal sensitivity to all pixels of CCD. Now source image frames of individual filters will be divided by normalized master flat frame of that filter.

(c) Cosmic Rays Removal

On visual inspection of source image frames, we noticed a few bright specks in addition to stars. These are cosmic ray events and need to be removed. The intensity profile of cosmic rays are different from the stellar profile. Cosmic rays are removed by using standard routine in IRAF software.

(d) Trimming the Image Frames

It is the last task in pre-processing in which we trim image edges. The edges of most of the CCD images may show some abnormal behaviour due to opening and closing of

CCD shutter. To avoid it, we usually trimmed 5 pixels from all four sides of source image frames and the trimmed image is further used for processing.

II. Image Processing

After completing the pre-processing of the data, we have removed the effect of detector. Now in processing stage which is also popularly called as photometry is done. Photometry involves the detection of source positions, and magnitudes of detected source for a given CCD image.

For doing photometry, we use standalone software DAOPHOT II (Stetson 1987). This software requires a list of prior information and included with various notations and abbreviations : (a) RE – the readout noise of the CCD (in analog-to-digital converter unit (ADU)); (b) GA – the number of photoelectrons corresponding to 1 ADU; (c) HI and LO – maximum and minimum observed brightness level above and below which the detector fails to operate linearly; (d) FW – full width at half maximum (FWHM) of an unresolved stellar image; (e) FI – fitting radius which is slightly (~ 0.5 pixel) less than FW; (f) PS – PSD radius which is $\sim 4 \times$ FI or FW; (g) WA – watch progress which is set to 1 and all the analysis can be seen on the computer screen. But if we set this parameter equal to 0, then nothing will be displayed on the computer screen; (h) AN – analytical model PSF which varies from 1 to 6. Different number from 1 to 6 represent different PSF model which we choose according to image quality; (i) TH – Threshold above which the stellar sources will be detected.

Following steps are involved in the processing the data:

(a) Object Detection

In DAOPHOT software a routine called FIND is used to detect star like objects. FIND routine convolves the image to locate a star in a pixel by fitting an analytic profile by supplying a analytical model parameter AN in DAOPHOT II (e.g. AN = 1 represents Gaussian profile). It tries to locate stars by going through pixel by pixel and looking for locations where the Gaussian profile fit is good, i.e, where the central height of the best fitted model Gaussian profile achieves a large, positive value lying near the center

of star image. In this way FIND identified the X and Y position of stars in the frame and catalogued them in a file with extension image file.coo.

(b) Photometry

Photometry gives the instrumental magnitude of star like objects detected by above FIND routine. Photometry is the brightness measurement of the objects. There are three different types of photometry: (a) aperture photometry, (b) profile fitting (PSF) photometry, (c) and surface photometry. PSF photometry is useful in a very crowded field where if we fit suppose Gaussian profile on each stars present in the field, there are events in which the two or more stars Gaussian profile fit have some overlap which imply if we try to get the brightness of one object, it will have additional flux from other object too. Surface photometry is useful for extended objects. So, for our project PSF and surface photometry are not of any use, so, we will not discuss those further in the thesis. Our sources are isolated star like objects in the image field and for that, aperture photometry is use. Here we will briefly describe about aperture photometry

(c) Aperture Photometry

It is clear from the name of photometry, we first get center coordinate of star like objects in image frames. Using the centre, we define concentric 4 - 5 circular apertures (maximum number of allowed concentric apertures are 12 by DAOPHOT II). The aperture has to be large enough to enclose the entire stellar image, therefore measuring all the light from the stellar image, so, no data under sampling will be there. We provide aperture size $\sim 1 \times \text{FWHM}$, $2 \times \text{FWHM}$, $3 \times \text{FWHM}$, $4 \times \text{FWHM}$. We have noticed that the $2 \times \text{FWHM}$ gives best S/N, and we use that aperture for doing photometry of objects detected in image frames by FIND routine. It is done with a routine called PHOT. Here we also set IS and OS and these parameters represent inner sky, and outer sky, respectively. Basically the median of annuls between IS and OS is used as background.

III. Post-processing

This step is also known as calibration of the photometric data i.e. the final data product which is free from all additional effects i.e. atmospheric, detector, telescope, etc. To reach on finally calibrated data, we have to go with following steps:

(a) Cross-matching Stars

In observing run where we have large number of image frames of a target object from one or more than one observing night, it is impossible that same object will always fall on the same pixel of detector. So, to make a catalogue of observation in a particular filter, we need a transformation of all the image frames on a self adopted standard image frame of that object in a specific filter. DAOMATCH routine of DAOPHOT II does it very well. This programme make triangles of stars. This programme considers maximum 30 brightest stars between the two frames and provides the coordinate transformation equations between the various frames with respect to a reference frame byu taking into linear and rotational transformation. The DAOMATCH programme lists all the X and Y coordinate transformations of all the image frames w.r.t. the master frame which we supplied as first input frame. With help of transformation coefficients provided by DAOMATCH, locally developed routine play a role to get instrumental magnitudes of the target blazar and several comparison stars with the time of observation extracted from photometry file of each image frame. Now the instrumental light curves of blazar and comparison stars in its field of view can be generated.

(b) Final Photometric Calibration

Our three TeV blazars which we have studied in the thesis have three or more local standard stars. To calibrate the instrumental magnitude of the blazar, we do following:

(1) We select 2 local standard star (say star A and star B). We try to find these standard star with nearly similar brightness and colour of the blazar. Suppose we say blazar as BL, then we generate time series data of BL - star A, BL - star B, and star A - star B. Since star A and star B are standard stars, star A - star B light curve w.r.t time will be non variable. After making sure star A - star B light curve has non-variable nature, we

use one of the star A or star B for calibration of the blazar data. Suppose we use Star A for calibration of blazar data then it will be as follows

$$StarA_{ins} = StarA_{std} + C \quad (2.1)$$

Here $StarA_{ins}$ = instrumental magnitude of Star A, $StarA_{std}$ = standard magnitude of Star A, C = constant. $StarA_{ins}$ is known for individual observation, $StarA_{std}$ is known and constant, and C will be different constant for different image frame which can be calculated with help of $StarA_{ins}$ and $StarA_{std}$. Since the blazar and the standard star were observed in the same field of view on same image frame, so the instrumental magnitude of blazar (BL_{ins}) should also differ from its calibrated magnitude (BL_{std}) by the same factor C i.e.

$$BL_{ins} = BL_{std} + C \quad (2.2)$$

So, the calibrated magnitude of the blazar can be given w.r.t standard star A is

$$BL_{std} = BL_{ins} - StarA_{ins} + StarA_{std} \quad (2.3)$$

and the uncertainty in calibrated magnitude is

$$\sigma(BL_{std}) = \sqrt{\sigma(BL_{ins})^2 + \sigma(StarA_{ins})^2} \quad (2.4)$$

Chapter 3

Multi-wavelength Flux Variability and Spectral Energy Distribution of the Blazar PKS 2155-304 from XMM-Newton

3.1 Introduction

In the present work, we have studied the optical/UV and X-ray band variability of the BL Lac PKS 2155–304 which is a HSP blazar. PKS 2155–304 was one of the first recognized BL Lacs (Schwartz et al. (1979); Hewitt & Burbidge (1980)) and is the brightest object in UV to TeV energies in the southern hemisphere. The redshift of PKS 2155 – 304 is 0.116 ± 0.002 as determined by optical spectroscopy of the galaxies in the BL Lac field (Falomo et al. (1993)). This object has been studied on many occasions in single and multiple bands of the EM spectrum to search for variability, cross-correlated variability, SEDs and other properties of the source on diverse timescales (e.g., Shimmins & Bolton (1974); Carini & Miller (1992); Urry et al. (1993); Brinkmann et al. (1994); Marshall

¹Work presented in this chapter has been published in Bhagwan et al. (2014), MNRAS, 444, 3647

et al. (2001); Aharonian et al. (2005); Dominici et al. (2006); Dolcini et al. (2007); Piner et al. (2008); Sakamoto et al. (2008); Kastendieck et al. (2011); H.E.S.S. Collaboration et al. (2012), and references therein).

The first X-ray observation of PKS 2155 – 304 was taken by Schwartz et al. (1979) using HEAO-1. Chadwick et al. (1999) detected for the first time very high energy gamma-ray photons from this source using the Durham MK 6 telescope and thus classified it as a TeV blazar. There also are more recent claims of TeV emission from this source (H.E.S.S. Collaboration et al. (2012), and references therein). Simultaneous multi-band observations of the source from optical to X-ray bands using XMM-Newton data were reported by Zhang et al. (2006a); Zhang et al. (2006b). Zhang (2008) found that the synchrotron emission of PKS 2155 – 304 peaked in the UV-EUV bands rather than the soft X-ray band. Gaur et al. (2010) searched for intra-day variability (IDV) and quasi-periodic oscillations (QPOs) in the source using XMM-Newton data. Using International Ultraviolet Explorer (IUE) observations in the UV band of PKS 2155 – 304 Urry et al. (1993) reported a possible short-lived QPO of ~ 0.7 day. More recently, stronger evidence for a ~ 4.6 hr QPO in this source on one occasion in XMM-Newton observations was reported by (Lachowicz et al. (2009).

The blazar’s flux is rapidly variable in all the EM bands and is often accompanied by spectral changes as well. Changes in the SEDs are very likely associated with changes in the spectra of the emitting electrons. Modelling of broad-band SEDs of blazars is required to understand the extreme physical conditions inside the different emission regions. Flux variability studies can in principle play an important role in understanding the physical phenomena that are responsible for the low, high and outburst states of the source. Such studies are very important in discriminating between the models and applying tight constraints on model parameters, which are usually changed under the assumption that all other parameters are fixed (e.g., Mukherjee et al. (1999); Petry et al. (2000); Hartman et al. (2001)). In the ideal case, such studies require large amounts of simultaneous data in various EM bands; unfortunately, this is severely lacking for blazars.

Thanks to the XMM-Newton satellite, which has instruments to observe simultaneously a specific source in optical, UV, and X-ray bands which can partially overcome the limitation of simultaneous data in various EM bands. On searching the complete archive of XMM-Newton, we found that there were 20 occasions on which data in at least one optical-UV band as well as X-ray bands were taken on same date for the BL Lac PKS 2155 – 304. These observations span a period of almost 12 years (2000 – 2012).

They are thus ideal for studying the long-term flux and spectral variability of the source in the optical, UV, and X-ray bands. We have used these data sets to generate simultaneous broad-band SEDs for the low-energy hump and we have fitted these SEDs with models to study the synchrotron emission mechanism and investigate how the various model parameters vary with the source flux.

3.2 The XMM-Newton Observations and data reduction

During the years 2000 – 2012 i.e. over the last ~ 12 years, the BL Lac PKS 2155 – 304 has been observed by XMM-Newton on 20 occasions. The journal of observations is given in Table 3.1. In the present work, we study the data obtained from the Optical Monitor (OM; [Mason et al. \(2001\)](#)) and the European Photon Imaging Camera (EPIC) PN detector ([Strüder et al. \(2001\)](#)). We did not consider the data from EPIC-MOS as the EPIC-PN data are more sensitive, and are less affected by photon pile-up effects. In all the observations, the EPIC-PN detector was operated in the small window (SW) imaging mode. The OM has three optical and three ultraviolet (UV) filters and can provide data in the optical/UV bands simultaneously with the X-ray observations. In all 20 observations with X-ray and at least one UV or optical band measurements are available in the archive.

We followed the standard procedure to reprocess the Observation Data File (ODF) with the XMM-Newton Science Analysis System (SAS) version 11.0.0 with the latest calibration files. We considered both single and double events ($PATTERN \leq 4$) of good quality ($FLAG = 0$). The source counts in each observation were accumulated from a circular region centred on the source and with a radius of $33''$ to $40''$. These radii have

been chosen to sample most of the PSF according to the observing mode. Background counts were accumulated from a circular region of radius $45''$ on the CCD chip where the source was located and was the least affected from the source counts. The EPIC-PN redistribution matrix and effective areas were calculated with the `rmfgen` and `arfgen` tasks, respectively.

We checked for the high soft proton background periods which are caused by solar activity by generating a hard-band background light curve in the energy range 10–12 keV. We then defined as the “good time interval” (GTI) those times where the hard band count rate was less than 0.4 ct/sec. We also investigated the possibility for photon pile-up effects, which may be strong for a bright source such as PKS 2155 – 304. To this end, we used the `epatplot` SAS task. We found that nine observations were affected by photon pile-up. For these observations we excluded a circular region with a radius of $10''$ centred on the source and we extracted the source counts in an annulus region which has an outer radius lying in the range of $33''$ to $40''$, depending on the position of the source on the chip.

We used the `efluxer` task to produce background subtracted, flux-calibrated EPIC-PN X-ray spectra in physical units of $\text{erg cm}^{-2} \text{s}^{-1}$. These spectra can be used to study the shape of the continuum X-ray emission in a model-independent way. On the other hand, their effective spectral resolution is degraded with respect to the intrinsic spectral resolution of EPIC-PN, but this is not a serious drawback in our case, as there are no narrow spectral features in the X-ray spectrum of this source. The final spectra are obtained between 0.3 – 10 keV with the default energy bins of the `efluxer` command. The Galactic hydrogen column density in the direction of PKS 2155 – 304 is $N_{\text{H}} = 1.71 \times 10^{20} \text{ cm}^{-2}$ which has been calculated through the N_{H} calculator tool available online¹; this was developed by Lorella Angelini at the *HEASARC* and uses the [Dickey & Lockman \(1990\)](#) density map. Although this is a rather low value, the X-ray spectra are expected to be significantly affected at energies below 0.5 keV. For that reason, we consider only the flux-calibrated spectra at energies higher than 0.6 keV. We have used the 0.6-10.0 keV X-ray flux in SED fittings.

¹<http://heasarc.gsfc.nasa.gov/cgi-bin/Tools/w3nh/w3nh.pl>

Table 3.1 Observation log of PKS 2155-304 with XMM-Newton EPIC/pn and optical monitor (OM)

Revolution	Obs.ID	Exp.ID	Start Date	End Date	Duration (ks)	Pileup	OM Filters ¹
087	0124930101	087-1	2000-05-30 05:29:42	2000-05-30 22:28:11	37.9	Yes	3
087	0124930201	087-2	2000-05-31 00:30:51	2000-05-31 20:40:09	59.3	Yes	1
0174	0080940101	0174-1	2000-11-19 18:38:20	2000-11-20 11:26:51	57.2	Yes	1
0174	0080940301	0174-2	2000-11-20 12:53:01	2000-11-21 05:56:32	58.1	Yes	1
0362	0124930301	0332-1	2001-11-30 02:36:09	2001-12-01 04:19:46	44.6	Yes	1,2,3,4,5,6
0450	0124930501	0450-1	2002-05-24 09:31:02	2002-05-25 14:38:50	96.1	Yes	3,4,5,6
0545	0124930601	0545-1	2002-11-29 23:27:28	2002-12-01 07:18:43	56.8	No	1,2,3,4,5,6
0724	0158960101	0724-1	2003-11-23 00:46:22	2003-11-23 08:19:01	26.6	No	2,3,4
0908	0158960901	0908-1	2004-11-22 21:35:30	2004-11-23 05:37:29	28.4	No	4,5,6
0908	0158961001	0908-2	2004-11-23 19:45:55	2004-11-24 06:59:34	39.9	No	1,2,3,4
0993	0158961101	0993-1	2005-05-12 12:51:06	2005-05-12 20:52:56	26.1	Yes	1,2,3,4,5,6
1095	0158961301	1095-1	2005-11-30 20:34:03	2005-12-01 13:20:58	59.9	Yes	1,2,3,4,5,6
1171	0158961401	1171-1	2006-05-01 12:25:55	2006-05-02 06:26:09	64.3	Yes	1,2,3,4,5,6
1266	0411780101	1266-1	2006-11-07 00:22:47	2006-11-08 04:26:19	29.9	No	1,2,3,4,5,6
1349	0411780201	1349-1	2007-04-22 04:07:23	2007-04-22 22:59:14	58.5	Yes	1,2,3,4,5,6
1543	0411780301	1543-1	2008-05-12 15:02:34	2008-05-13 08:02:50	60.7	Yes	1,2,3,4,5,6
1734	0411780401	1734-1	2009-05-28 08:08:42	2009-05-29 02:09:02	64.3	Yes	1,2,3,4,5,6
1902	0411780501	1902-1	2010-04-28 23:47:42	2010-04-29 20:26:00	69.1	No	1,2,3,4,5,6
2084	0411780601	2084-1	2011-04-26 13:50:40	2011-04-27 07:34:18	63.3	Yes	1,2,3,4,5,6
2268	0411780701	2268-1	2012-04-28 00:48:26	2012-04-28 19:54:01	53.6	No	1,2,3,4,5,6

¹ 1 = UVW2, 2 = UVM2, 3 = UVW1, 4 = U, 5 = B, 6 = V

The OM data were taken in the standard imaging mode. We reduced the OM data with the standard SAS routine `omichain`. This routine provides a *combolist* file with the source count rate and instrumental magnitudes for all the sources which are present in the field of view. The PKS 2155 – 304 fluxes corresponding to six optical/UV filters were corrected for galactic reddening ($E_{B-V} = 0.019$; Schlafly & Finkbeiner (2011) with the standard reddening correction curve by Cardelli et al. (1989)) and applied using equation (2) in Roming et al. (2009).

3.3 The observed long-term light curves

Fig. 3.1 shows the long term optical, UV, and X-ray light curves of PKS 2155–304, using the observations we studied in this work. The points in this figure indicate the average count rate of each observation in the various OM filters, in the 0.6–2 keV (“soft”) and 2–10 keV (“hard”) X-ray bands. On visual inspection, the source is highly variable in all bands, over the time period of ~ 12 years on which the XMM–Newton observations were performed. We have estimated the rms variability amplitude i.e. $\sqrt{\sigma^2/m^2}$ where σ^2 and m are the variance corrected for the experimental contribution, and mean of the light curve, respectively for each light curve. The variability amplitude increased slightly going from the soft to hard X-ray bands but it decreased going from optical to UV bands. The values of rms variability amplitudes corresponding to the hard X-ray, soft X-ray, UVW2, UVM2, UVW1, U, B, and V bands are 0.38, 0.35, 0.36, 0.38, 0.38, 0.39, 0.40, and 0.47, respectively.

On visual inspection, the observed variations in the optical bands are well correlated with the variations in the UV bands. The same appears to be true with the variations detected in the soft and hard X-ray bands. However, this is not the case when we compare the variability detected in the optical/UV bands and in the X-rays. Fig. 3.2 shows the UVW1 count rate plotted as functions of the 2–10 and 0.6–2 keV band measurements (upper and lower panels, respectively). Clearly, the flux variations in the UV and X-ray bands are not well correlated.

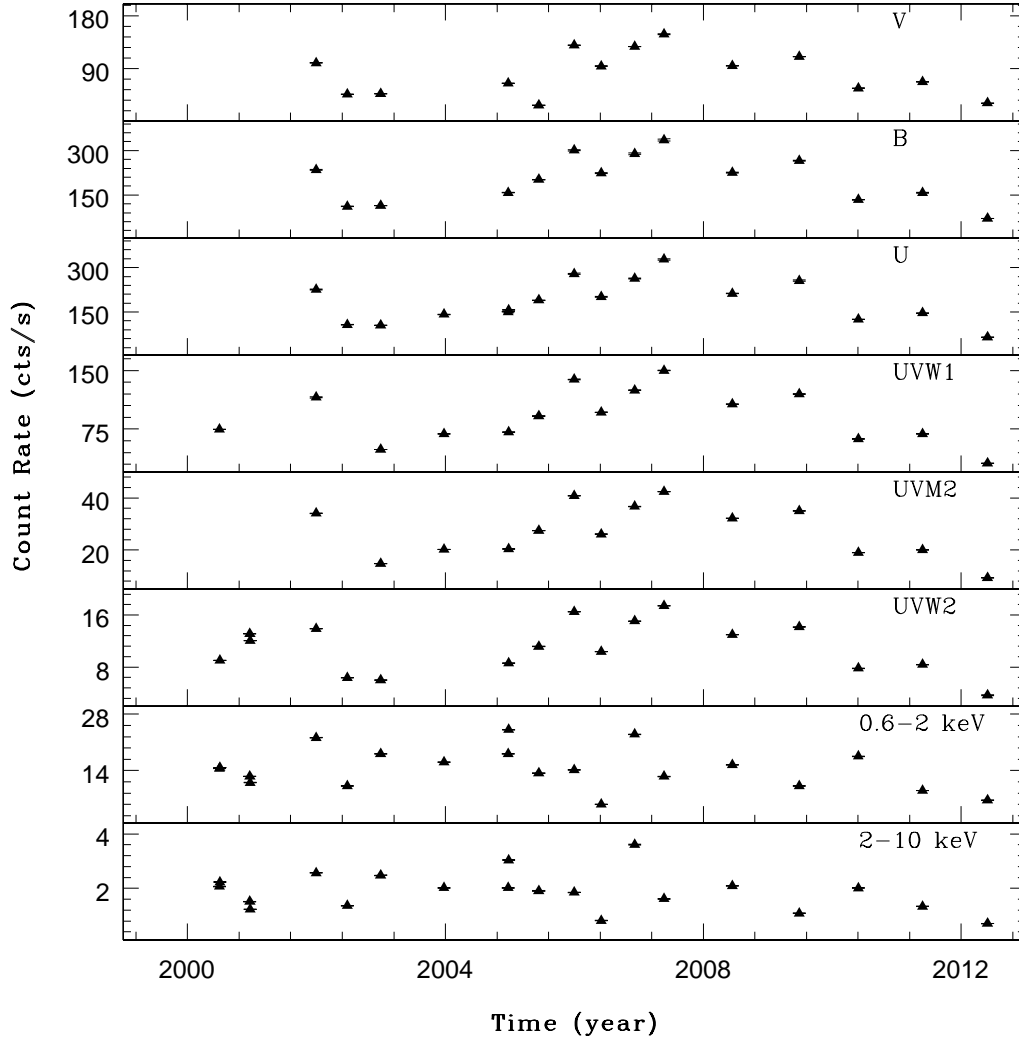


Figure 3.1 Long term variability light curves for the XMM-Newton optical/UV and X-ray bands

3.4 SED Modeling

Fig. 3.3 to Fig. 3.9 show twenty optical/UV to X-ray SEDs of PKS 2155 – 304, using the mean optical and UV flux measurements in each XMM-Newton observation and the flux calibrated EPIC-PN data we described in the previous section. The spectra cover a frequency range of over three orders of magnitude. More importantly, as we have stressed earlier, the data in the optical and UV bands are simultaneous with those in the X-ray bands. Given the shape of the SED in the optical/UV and X-ray bands, the low energy synchrotron peak of this source is located between the energy bands sampled

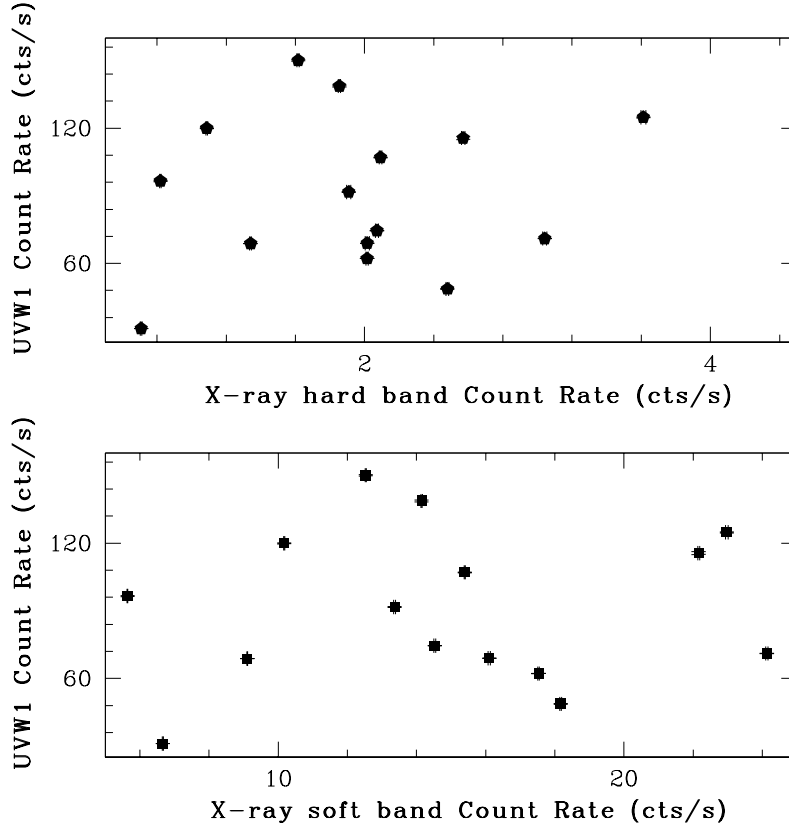


Figure 3.2 UV versus soft (0.6-2.0 keV) and hard (2.0-10 keV) X-ray band plot.

by the XMM-Newton OM and EPIC-pn observations.

We fitted all SEDs with two models. The first one was a log-parabolic model. We also considered the case of a spectral model that has a power law shape at low energies, and then acquires a log-parabola form at higher energies, following [Massaro et al. \(2006\)](#) and [Tramacere et al. \(2009\)](#). We describe below the best-fit results in both cases.

3.4.1 Log-parabolic fits

Log-parabolic models are parametrized with functions of the form $F(E) = KE^{-(\Gamma+b\text{Log}(E))}$, where $F(E)$ is the source flux in units of photons $\text{cm}^{-2} \text{s}^{-1} \text{keV}^{-1}$ at energy E (see e.g. [Massaro et al. \(2004\)](#)). The Γ parameter is the photon index at 1 keV, and b is a parameter that measures the spectral curvature. Since in our case the data are directly in flux density units (i.e. $\text{ergs cm}^{-2} \text{s}^{-1}$), we decided to fit them with a model of the form:

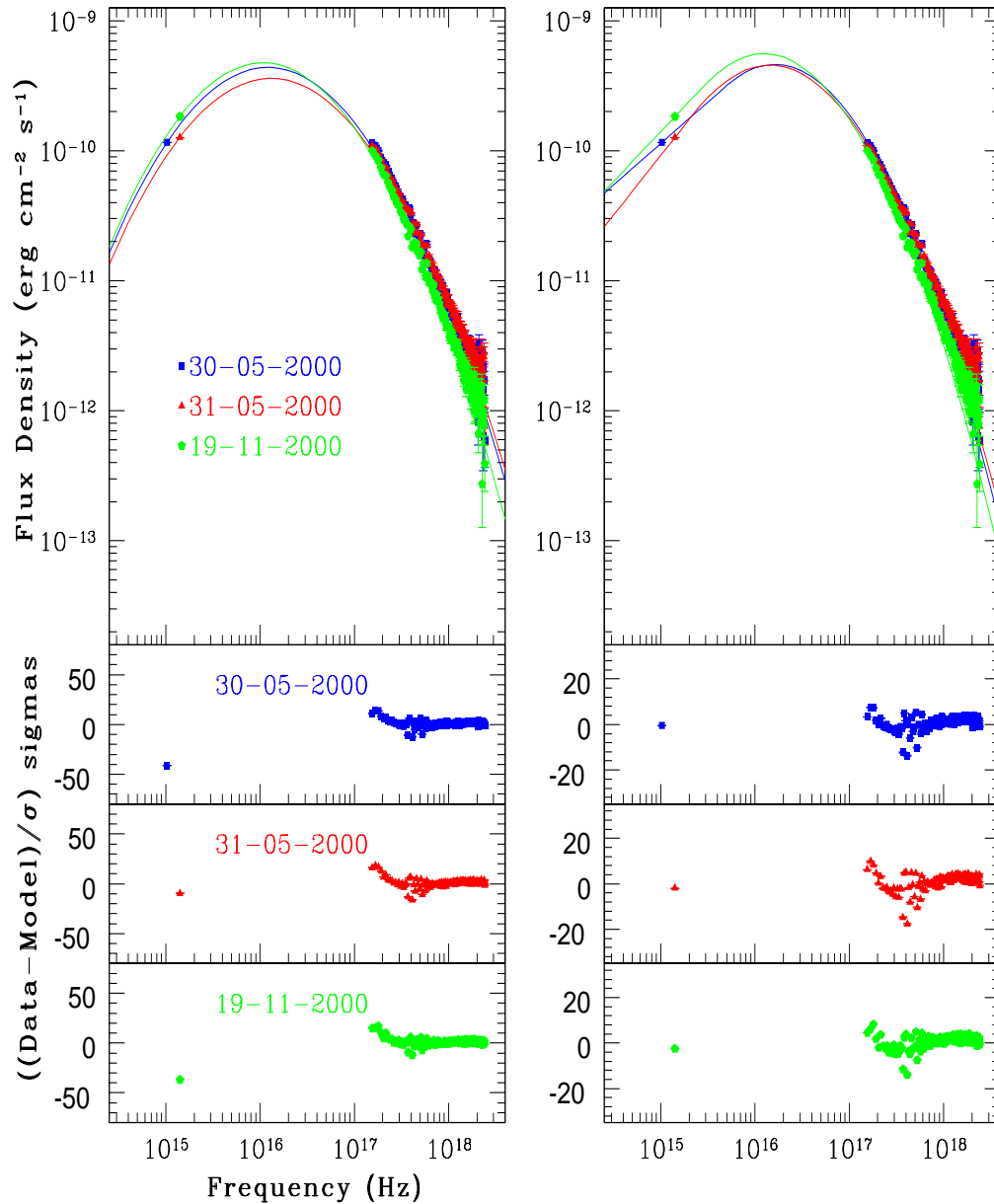


Figure 3.3 Example SED and best-fit model curves for three observations. The best-fit curves in the case of the log-parabolic model (together with the corresponding residuals) are plotted in the upper and lower left panels, respectively. In the right hand panels, we plot the best-fit curves (and the residuals) in the case of the power-law+log-parabolic model.

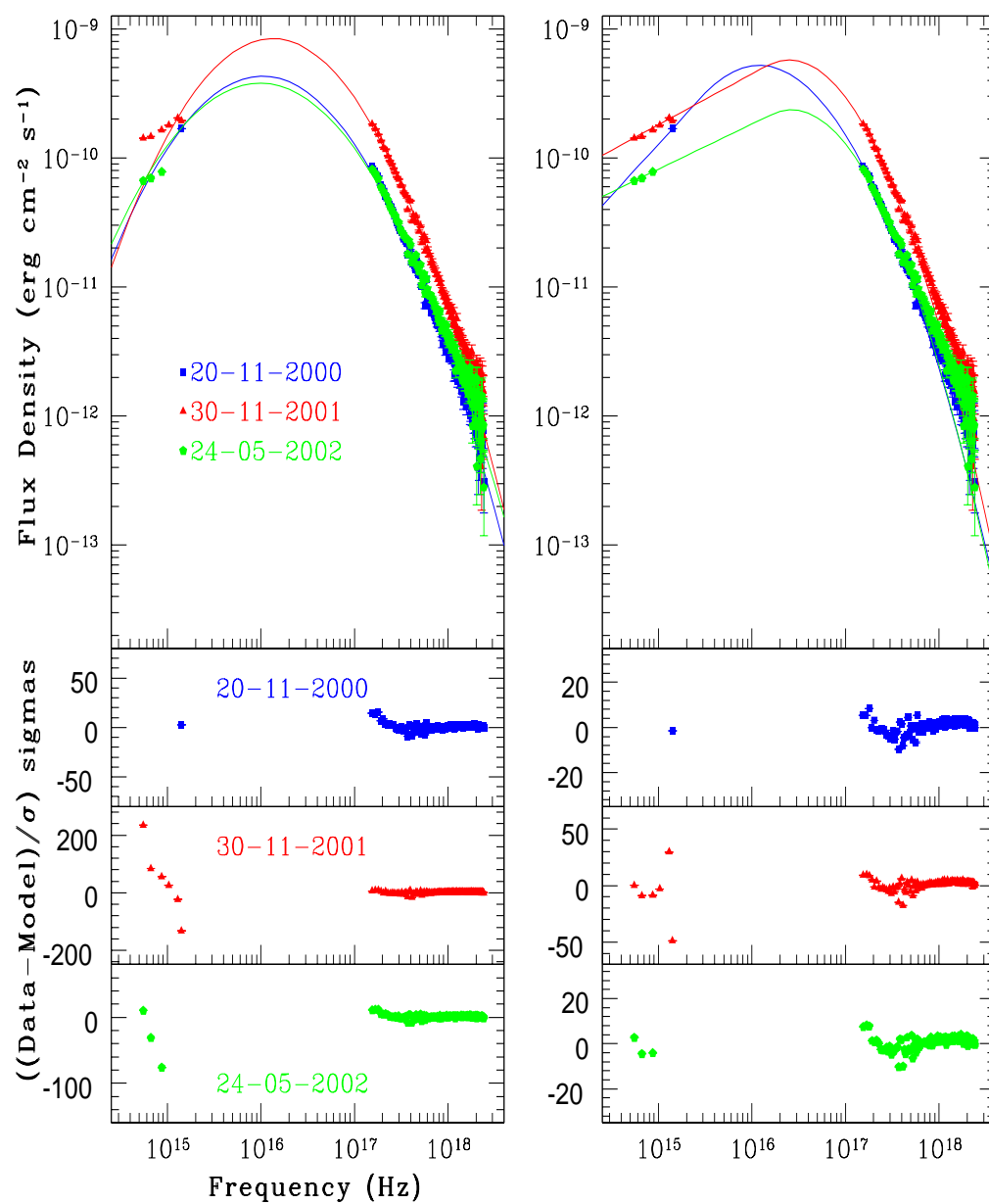


Figure 3.4 Same as figure 3.3 for three different dates of observations.

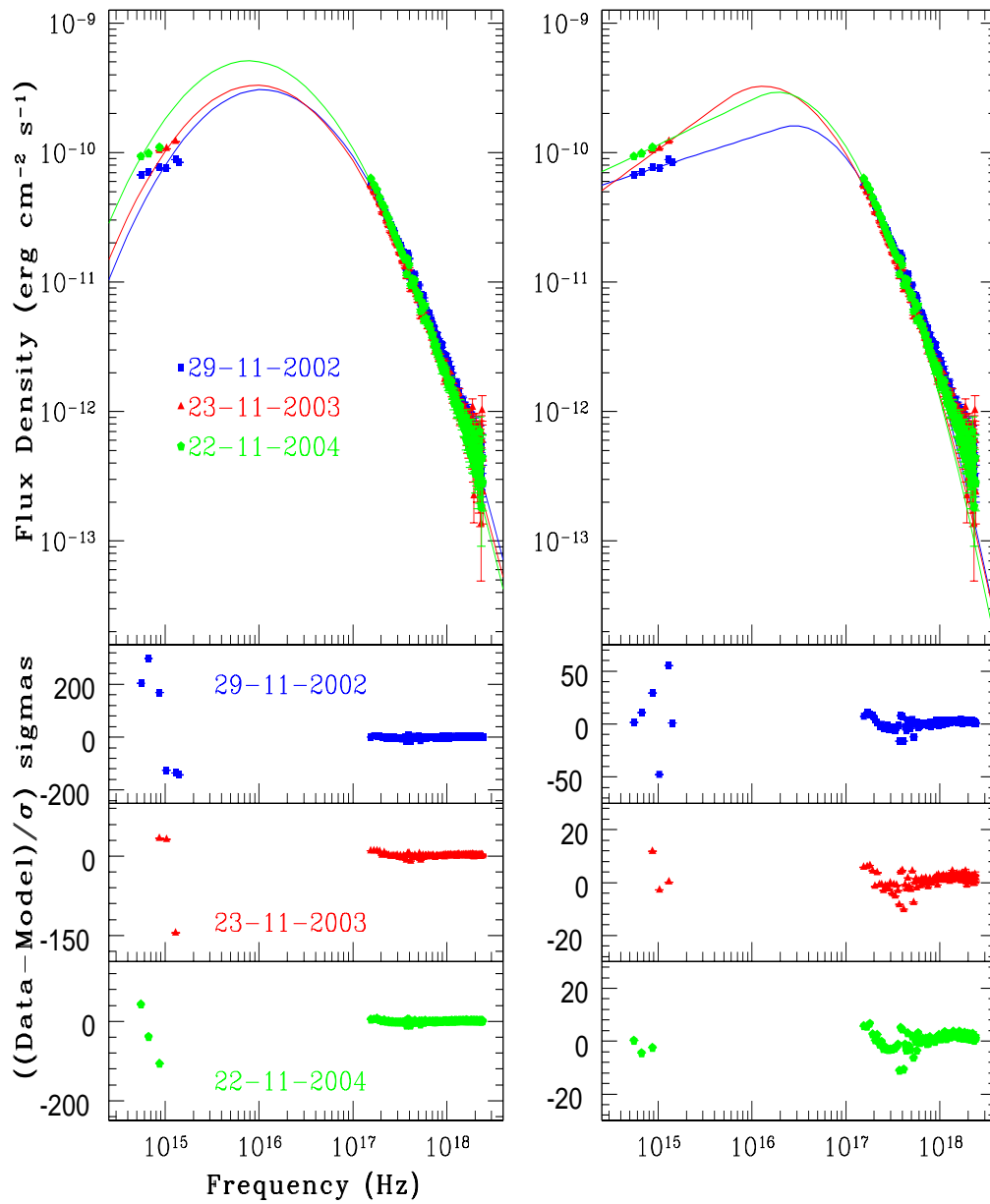


Figure 3.5 Same as figure 3.3 for three different dates of observations.

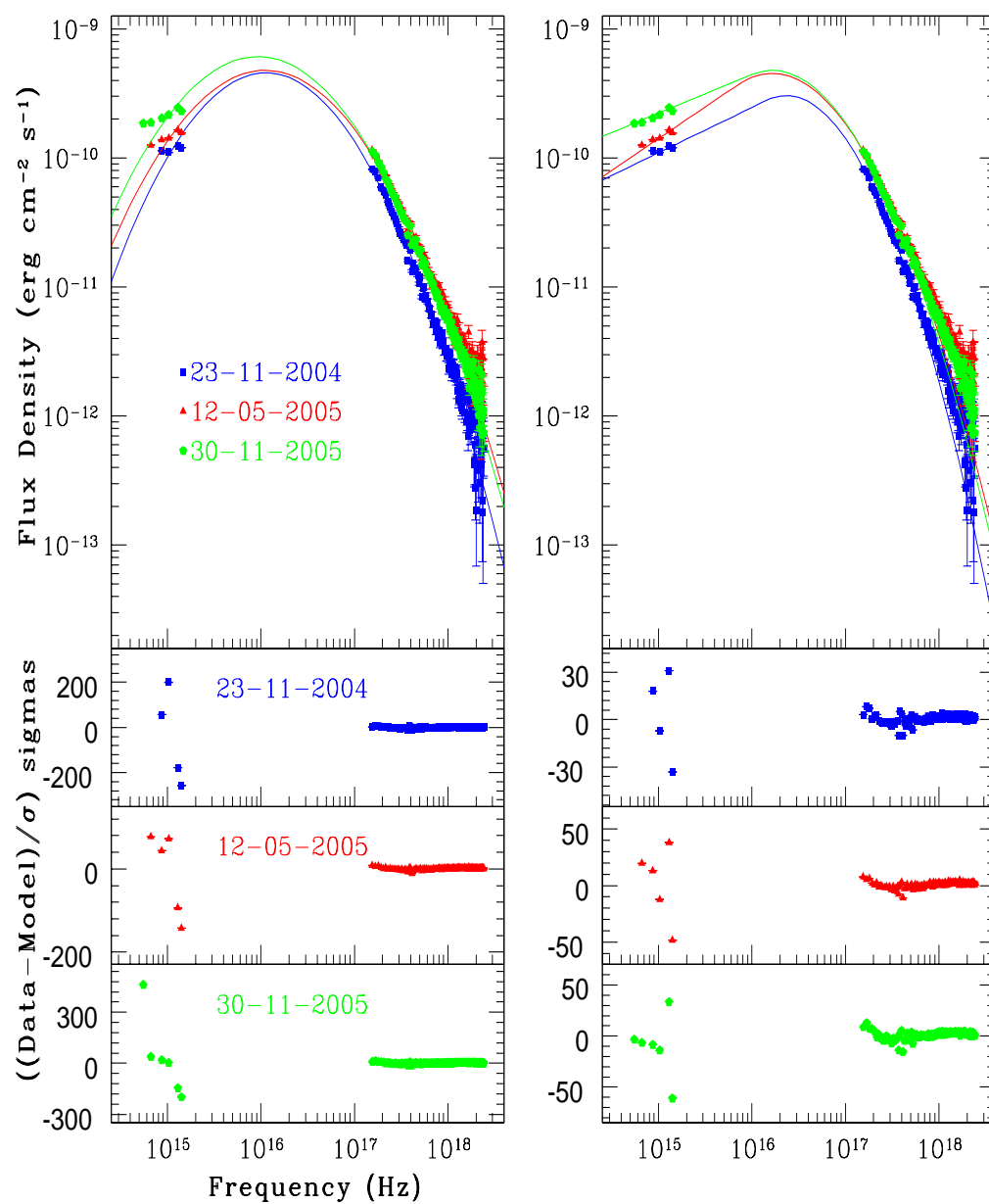


Figure 3.6 Same as figure 3.3 for three different dates of observations.

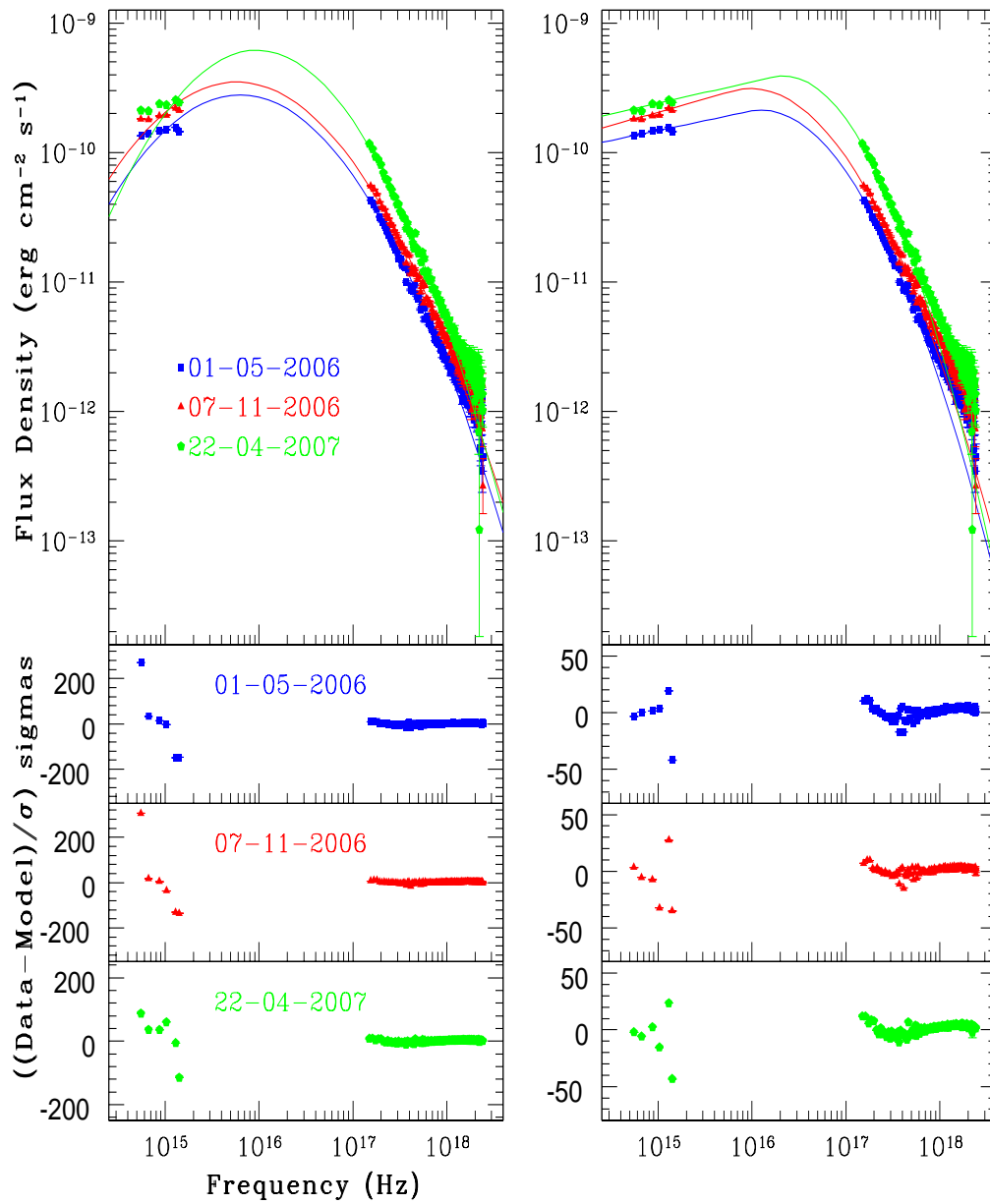


Figure 3.7 Same as figure 3.3 for three different dates of observations.

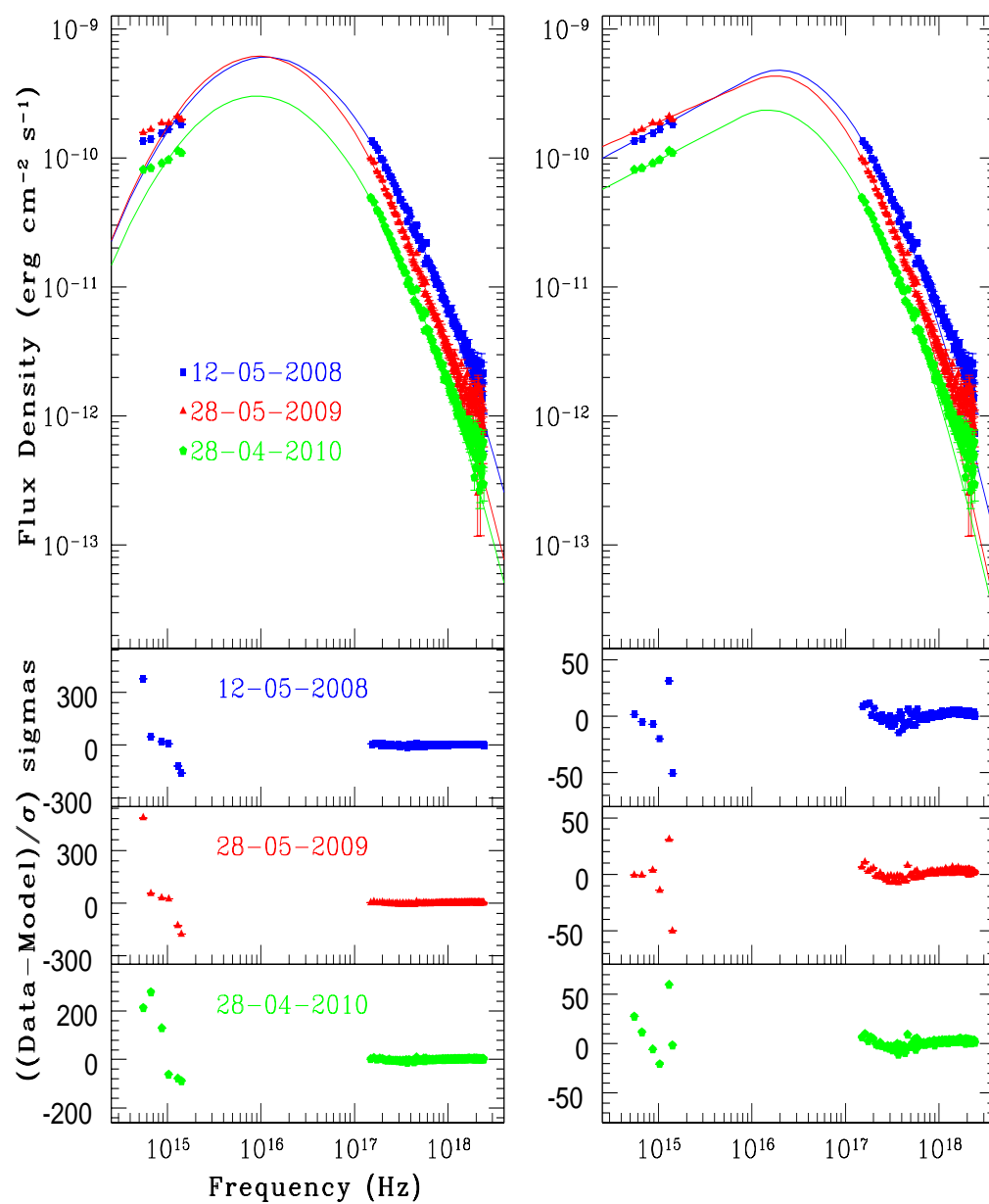


Figure 3.8 Same as figure 3.3 for three different dates of observations.

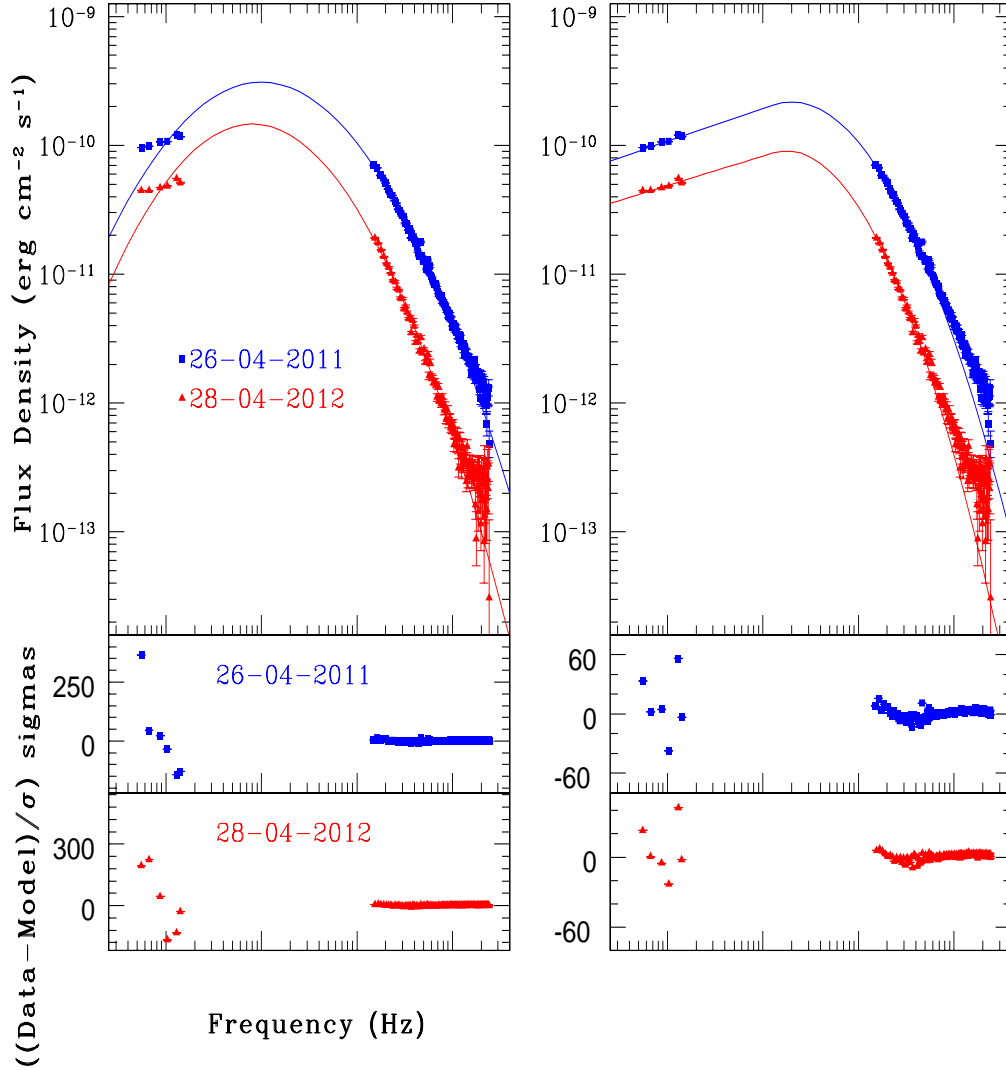


Figure 3.9 Same as figure 3.3 for two different dates of observations.

$$S(E) = K_S 10^{-b[\log(E/E_p)]^2}, \quad (3.1)$$

where $S(E) = E^2 F(E)$, and $K_S = E_p^2 F(E_p)$. The model has three free parameters: E_p , which is the energy where the peak power is emitted (in units of keV), K_S (the model normalization), which indicates the power at E_p , and the spectral curvature parameter b . Log-parabolic models best fit curved spectra which decrease symmetrically around their peak frequency, and b determines the curvature of the model around E_p . Similar models have been applied for a long time to parametrize blazar spectra in various energy

Table 3.2 The SED best-fitting model parameter values for the LP model. K_S : normalization constant (peak power) in units of 10^{-10} erg cm $^{-2}$ s $^{-1}$. b : spectral curvature parameter. E_p : energy at which the peak power is emitted in units of 10^{-2} keV.

Observation ID	K_S	b	E_p	χ^2/dof
0124930101	4.4	0.50	5.0	3257/122
0124930201	3.6	0.49	5.4	2489/122
0080940101	4.8	0.53	4.4	3094/122
0080940301	4.3	0.54	4.3	1423/122
0124930301	8.4	0.60	5.5	85765/127
0124930501	3.8	0.49	4.0	7850/124
0124930601	3.1	0.55	4.5	213989/127
0158960101	3.3	0.55	3.8	24141/123
0158960901	5.1	0.56	3.3	15388/124
0158961001	4.6	0.59	4.7	141156/125
0158961101	4.8	0.50	4.6	42881/125
0158961301	6.1	0.50	3.8	276580/127
0158961401	2.8	0.43	2.6	120717/127
0411780101	3.5	0.40	2.4	132211/127
0411780201	6.2	0.52	3.9	28801/127
0411780301	6.0	0.52	4.7	187076/127
0411780401	6.2	0.57	4.0	288613/127
0411780501	3.0	0.54	3.8	157672/127
0411780601	3.1	0.47	4.1	175309/127
0411780701	1.5	0.55	3.3	137475/126

bands. For example, [Landau et al. \(1986\)](#) analysed the SEDs of a sample of blazars in millimetre to UV bands and found that the synchrotron emission of BL Lac sources were well fitted by a log-parabolic model. [Krennrich et al. \(1999\)](#) also used the log-parabolic model to describe the spectral curvature of Mkn 421 in the TeV band, while [Giommi et al. \(2002\)](#) applied it to the X-ray SEDs of 157 blazars observed by BeppoSAX.

The best model fit results are listed in Table 3.2, together with the best-fit χ^2 values (and the degrees of freedom – dof). Obviously, the best-model fits are not statistically acceptable for any of the 20 SEDs. (It is for this reason that we do not provide errors on the best-fitting model parameter values). Examples of the quality of the model fits are shown in Fig. 3.3 to 3.9. The solid lines in the upper left hand panel of Fig. 3.3 to Fig. 3.9 indicate the best-fit log-parabolic model to the SEDs that are plotted in the same panel, and in the left lower panels of the same Figures we also plot the best-fit residuals.

Fig. 3.3 to Fig. 3.9 indicate that there are systematic discrepancies between the best-fit models and the data at both high ($> 10^{18}$ Hz) and low ($< 10^{15}$ Hz) frequencies. These discrepancies could be the major reasons for the large χ^2 values. In the high frequency end, the observed SED is always flatter than the best-fit models. This spectral flattening could be caused by the fact that the inverse Compton (IC) component starts contributing to the emission observed above $\sim 10^{18}$ Hz (i.e. $\sim 4 - 5$ keV). In the low frequency end, the observed flux is higher than the model flux in almost all cases (see for example the 22/04/2007 SED in Fig. 3.7).

There are three obvious physical possibilities for the discrepancy at lower frequencies. The first would be the contribution of the host galaxy emission, which should be more significant in the optical bands. However, if this contamination were to be important, the discrepancy should be much smaller at high flux states since we can safely assume that the host galaxy emission is constant; this is not the case. The second possible physical explanation would be that the emission from the broad line region (BLR) and/or the underlying accretion disk is variable, and contributes significantly in the low frequency part of the observed SED.

A third possibility is that a log-parabolic model is not actually the true underlying physical model for the broad band, optical/UV upto X-ray SED of the source. For that reason, we also investigated the possibility that the low energy segment of the PKS 2155–304 UV to X-ray spectra follows a single power law and the log-parabolic bending becomes apparent only above a “critical”, turn-over energy, E_c .

3.4.2 Power-law plus log-parabolic (PLLP) fits

In the case of spectra in units of photons $\text{cm}^{-2} \text{sec}^{-1} \text{keV}^{-1}$ this model is defined as: $F(E) = K(E/E_c)^{-\Gamma}$, at energies below E_c , and $F(E) = K(E/E_c)^{[-\Gamma - b \log(E/E_c)]}$ at energies higher than E_c (Γ is the photon index). For spectra in flux density units (like our case), the above equations become:

$$S(E) = K_S(E/E_c)^{-\alpha'}, E \leq E_c, \quad (3.2)$$

$$S(E) = K_S(E/E_c)^{[-\alpha' - b \log(E/E_c)]}, E > E_c, \quad (3.3)$$

where K_S is the model normalization ($K_S = KE_c^2$), and $\alpha' = \Gamma - 2$ is the spectral index of the SED in flux density units (i.e., $S(E) = E^2 F(E)$; we chose to denote the spectral index with α' in order to distinguish it from the usual spectral slope, $\alpha = \Gamma - 1$, which applies to SEDs in power over keV units). In this model, the energy where the peak power, S_p , is emitted is given by: $E_p = E_c 10^{-\alpha'/2b}$.

The best model fit results are listed in Table 3.3, together with the best-fit χ^2 values and dof. Although the χ^2 values have decreased significantly when compared to the χ^2 values in the case of the log-parabolic best model fits, these models are still not statistically acceptable for any of the 20 SEDs. Examples of the quality of the model fits are also shown in Fig. 3.3 to Fig. 3.9. The solid lines in the upper right hand panel in this figure indicate the best-fit PLLP models to the SEDs that are plotted in the same panel, and in the right lower panels of the same Figure we plot the respective best-fit residuals.

This time, the best-model fits do not over-predict the UV spectra at low frequencies, but the X-ray band residuals display a “wavy” pattern. This is the result of the fact that the model does not fit well the X-ray data above $\sim 5 \times 10^{17}$ Hz. The χ^2 values decrease even more, although the reduced χ^2 values increase significantly in some cases. A major reason for this is the extremely small error bars in the optical/UV part of the spectra. Indeed, the discrepancy between the best-fit model and the observed SEDs (i.e. the ratio “(data-model)/data”) is of the order of $\sim 5\%$ in the UV band, and even smaller in the X-ray band (except from the $3.5 - 4 \times 10^{17}$ Hz region, where we observe discrepancies of the order of 10 – 20 % in all spectra), even in the case of the SEDs with the highest χ^2 values. In fact, if we assume that the error of the SED points in all cases is equal to 5% of the SED values, then the best-fit models to all spectra are now acceptable (with reduced χ^2 values of the order of 1 – 2). In this case, we can also estimate the 1- σ error for the best-fit parameter values. These errors are indicated in Table 3 by the numbers in the parentheses next to the best-fit results in the case of the SED fits up to the 5×10^{17} Hz.

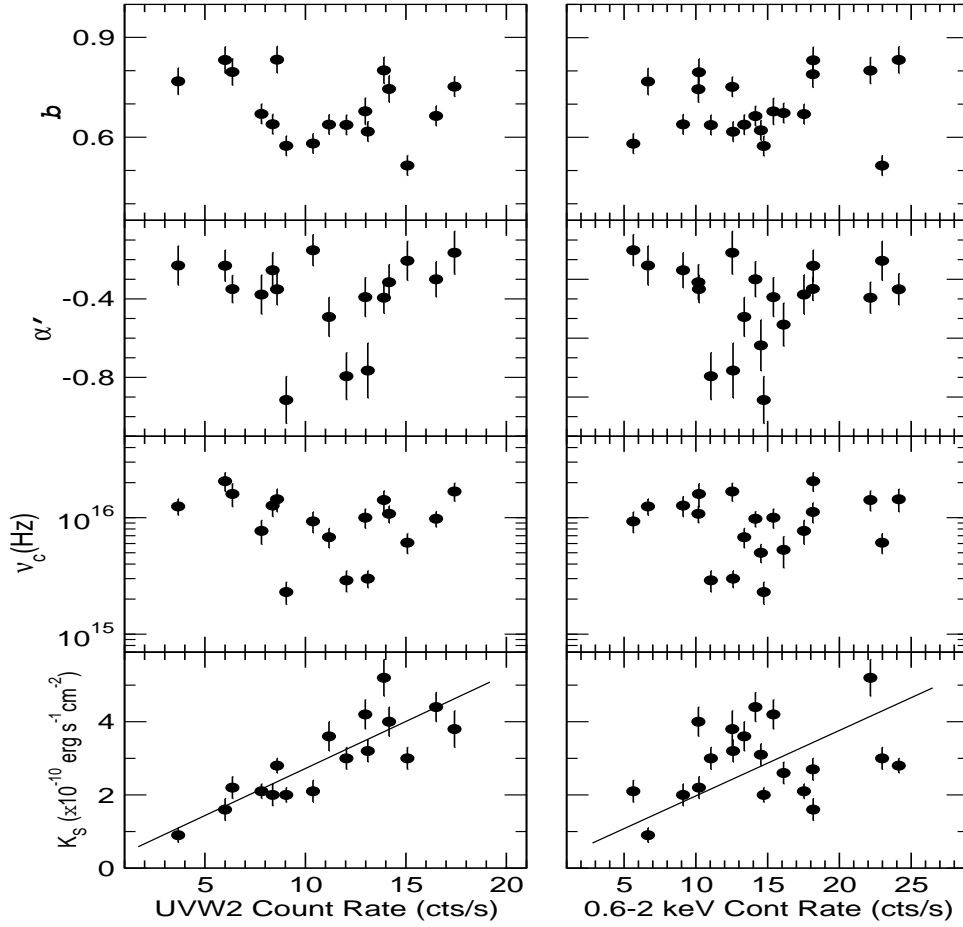


Figure 3.10 Plots of the best-fit values of the spectral curvature b , spectral slope α' , turn-over frequency ν_c and normalization constant K_S , as function of the UVW2 and the 0.6–2 keV count rates (left and right panels, respectively). The solid line in the lower panels indicates lines with a slope of one, and are plotted for illustration purposes (see text for details).

We used the PLLP best-fit results to investigate correlations between the best-fit model parameters and the observed UV and soft X-ray count rates. Fig. 3.10 shows plots of the best-fit model parameters with the observed UVW1 and 0.6–2 keV count rates (left and right panels, respectively). To quantify the correlation we used both the frequently used Pearson’s r as well as the non-parametric Kendall’s τ . Only the model normalization (i.e., K_S) is positively correlated with the UV flux (see lower left panel in Fig. 3.10). The correlation is statistically significant, and rather strong: Pearson’s r is 0.84 ($\tau = 0.65$)

and the probability that this value appears by chance is $P_{\text{null}} = 2.5 \times 10^{-5}$ (3×10^{-4}). In order to emphasize even more the correlation between the model normalization and the UV flux, the solid line in the bottom left panel of Fig. 3.10 indicates a straight line with a slope of unity. This is not the best fit to the data plotted in the same panel, but we plot it there in order to indicate that such a line appears to describe well the relation between the data plotted. Therefore, the UV flux variations could indeed be, to a large extent, proportional to the model normalization variations; i.e.. to a first approximation, the UV flux is simply responding to the model normalization variations, without being affected by the other model parameter changes.

On the other hand, K_S does not correlate significantly with the soft X-ray flux (and neither does any of the other best-fit model parameter values). In the lower-right panel of Fig. 3.10 we also plot the one-to-one line. There may exist a rough positive correlation between the two quantities, but both Pearson's r and Kendall's τ imply that this correlation is not statistically significant. This result explains the lack of correlation we observe between the UV and X-ray fluxes (see Fig. 3.1). While the UV flux responds mainly to the model normalization, the X-ray flux must also be significantly affected by spectral shape variations as well (i.e. variations of b and E_c).

We also investigated the correlations within the model parameters. The only significant correlation that we found are those between ν_c (the turn-over frequency which corresponds to E_c) and α' (Pearson's $r = 0.73$, Kendall's $\tau = 0.5$, and $P_{\text{null}} = 2.2 \times 10^{-4}$ and 2.3×10^{-3} , respectively) and between ν_c and b ($r = 0.80$, $\tau = 0.65$, $P_{\text{null}} = 2.7 \times 10^{-5}$, and 5.7×10^{-5} , respectively). Fig. 3.11 left panel shows a plot of α' and b versus ν_c . Our results indicate that flatter and more curved spectra are associated with higher turn-over frequencies.

The top right panel in Fig. 3.11 shows a plot of the model curvature b as a function of ν_p (the frequency at which the maximum power is emitted). Not surprisingly, given the correlation between ν_p , α' , and b , the parameters b and ν_p are also strongly correlated. The correlation is positive, in the sense that as the peak power increases, the spectral curvature increases as well. The dashed line in the same panel indicates the best-fit line to the data (in the log-log space).

The fit has been performed using the “ordinary least-squares bisector” method of [Isobe et al. \(1990\)](#). The best-fit result indicates that: $b \propto \nu_p^{0.48 \pm 0.04}$. The error on the best-fit slope value indicate that the positive correlation between the parameters (in the log–log space) is significant at a level much higher than 3σ . The lower right panel in the Fig. 3.11 shows S_p (i.e. the maximum emitted power) plotted as a function of ν_p . The two parameters appear to be loosely anti-correlated ($r = -0.21, \tau = -20$, but $P_{\text{null}} \sim 0.2-0.3$, in both cases). However, when we fit the data (in log-log space, we find that: $S_p \propto \nu_p^{-1.23 \pm 0.23}$). This result indicates that, if there is a correlation between these two parameters, it is an anti-correlation: as the maximum power emitted increases, the frequency at which it is emitted decreases.

3.5 Discussion and Conclusions

We have studied 20 archival XMM-Newton observations of PKS 2155 – 304 which have been performed in a period of over twelve years from 2000 to 2012. These observations can be useful in the study of the long-term optical/UV and X-ray variability of the source, not just because their number is large, but also because they allow us to study the flux and spectral variability of the source, over a broad frequency range, *simultaneously*. Our main results can be summarized as follows:

Table 3.3 The SED best-fit model parameter values for the power-law+log-parabolic model. (Numbers after the slash indicate the best fit results in the case of the model fits to the SED data up to 5×10^{17} Hz.)

Observation ID	K_S	ν_c	α'	b	χ^2/dof
0124030101	2.2/3.1(± 0.3)	2.3/5.0(± 0.9)	-0.82/-0.64(± 0.13)	0.54/0.62(± 0.03)	1208/122 & 394/25
0124930201	1.7/2.0(± 0.2)	2.0/2.3(± 0.5)	-0.86/-0.92(± 0.12)	0.52/0.57(± 0.03)	1847/122 & 646/25
0080940101	2.8/3.2(± 0.3)	2.4/3.0(± 0.5)	-0.77/-0.76(± 0.14)	0.56/0.62(± 0.03)	1171/122 & 379/25
0080940301	2.5/3.0(± 0.3)	2.3/2.9(± 0.6)	-0.81/-0.79(± 0.12)	0.58/0.64(± 0.03)	1012/122 & 245/25
0124030301	4.8/5.2(± 0.5)	11.6/14.2(± 2.8)	-0.40/-0.39(± 0.08)	0.70/0.80(± 0.04)	5294/127 & 4058/30
0124930501	2.1/2.2(± 0.3)	10.0/16.0(± 3.6)	-0.40/-0.35(± 0.07)	0.63/0.80(± 0.04)	1000/124 & 280/27
0124030601	1.5/1.6(± 0.3)	16.6/20.6(± 3.8)	-0.24/-0.23(± 0.08)	0.71/0.83(± 0.04)	8266/127 & 7030/30
0158960101	2.3/2.6(± 0.3)	4.2/5.3(± 1.6)	-0.53/-0.53(± 0.11)	0.60/0.67(± 0.03)	1029/123 & 412/27
0158960901	2.6/2.7(± 0.3)	8.4/11.2(± 2.2)	-0.38/-0.35(± 0.06)	0.69/0.79(± 0.04)	919 /124 & 335/27
0158961001	2.6/2.8(± 0.2)	11.8/14.4(± 3.2)	-0.35/-0.35(± 0.08)	0.73/0.83(± 0.04)	3310/125 & 2726/28
0158961101	3.2/3.6(± 0.4)	5.1/6.8(± 1.3)	-0.49/-0.49(± 0.10)	0.55/0.64(± 0.03)	5288/125 & 4686/29
0158961301	4.1/4.4(± 0.4)	7.6/9.8(± 1.5)	-0.30/-0.30(± 0.09)	0.57/0.66(± 0.03)	6965/127 & 5727/30
0158961401	2.0/2.1(± 0.3)	6.6/9.3(± 1.9)	-0.15/-0.15(± 0.08)	0.48/0.58(± 0.03)	4726/127 & 2782/30
0411780101	2.8/3.0(± 0.3)	4.4/6.1(± 1.2)	-0.21/-0.21(± 0.10)	0.43/0.52(± 0.03)	4533/127 & 3473/30
0411780201	3.8/3.8(± 0.5)	11.8/16.8(± 3.0)	-0.18/-0.16(± 0.11)	0.61/0.75(± 0.03)	4792/127 & 3100/31
0411780301	3.8/4.2(± 0.4)	7.8/10.0(± 1.9)	-0.39/-0.39(± 0.10)	0.59/0.68(± 0.04)	6042/127 & 4577/30
0411780401	3.8/4.0(± 0.4)	8.9/10.8(± 1.8)	-0.32/-0.32(± 0.09)	0.66/0.74(± 0.04)	5000/127 & 3980/31
0411780501	1.9/2.1(± 0.2)	6.4/7.7(± 1.8)	-0.38/-0.38(± 0.10)	0.60/0.67(± 0.03)	6452/127 & 5299/31
0411780601	2.0/2.0(± 0.3)	10.0/12.7(± 2.5)	-0.26/-0.25(± 0.09)	0.55/0.64(± 0.03)	8006/127 & 6354/31
0411780701	0.8/0.9(± 0.2)	9.9/12.5(± 2.0)	-0.23/-0.23 (± 0.10)	0.66/0.77(± 0.04)	3721/126 & 3101/30

K : normalization constant in units of 10^{-10} erg cm $^{-2}$ s $^{-1}$.

ν_c : turn-over frequency in units of 10^{15} Hz.

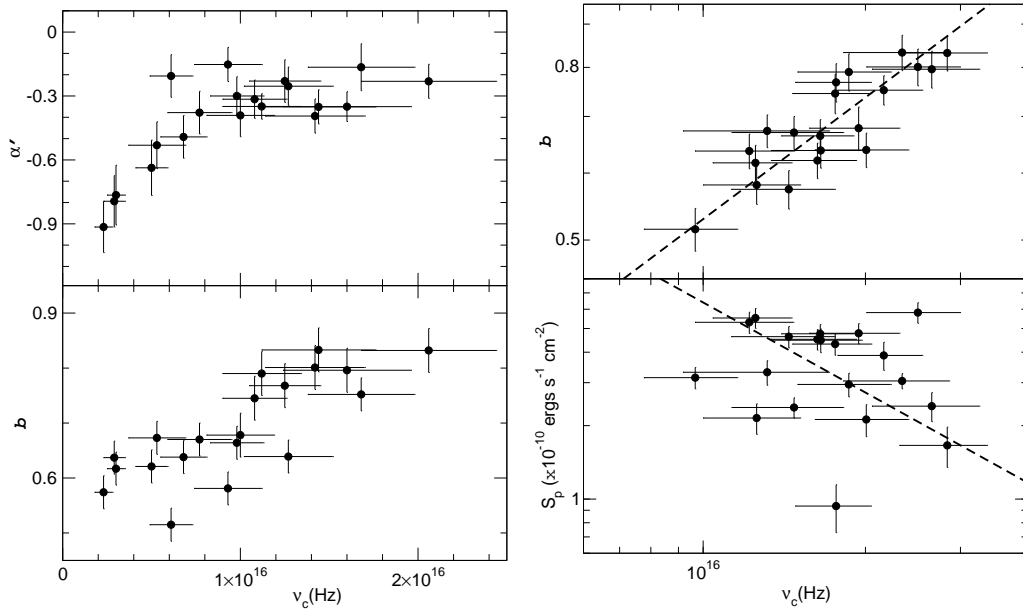


Figure 3.11 Left panel shows the best PLLP fit α' and b values plotted as a function of the turn-over frequency, ν_c . Right panel shows the b and S_p parameter values plotted as a function of the peak frequency, ν_p

(1) The source is variable at all bands on time scales of years. The amplitude of the rms variability is of the order of $\sim 35 - 45\%$ at all bands. We did not observe any extreme activity taking place during these observations. The variability amplitude slightly increases from the soft to the hard X-ray band, and decreases from the optical to the UV bands.

(2) The optical/UV band fluxes increase and decrease in phase, i.e. the optical/UV band variations are well correlated. However, the X-ray and optical/UV fluxes are not correlated.

We then used (i) a log-parabolic (LP) model and (ii) a power-law plus log-parabolic (PLLP) model to fit the broad band SEDs. The LP model fits are not formally acceptable. [Massaro et al. \(2004\)](#) and [Tramacere et al. \(2009\)](#) have found that a LP model can well fit the optical/UV and X-ray spectra individually, but could not fit the combined optical/UV and X-ray bands. Our results are in agreement with their results.

The fits improve in the case of the PLLP model, but there are still significant discrepancies above ~ 4 keV in the X-rays, most probably due to the increased contribution of the

IC component at larger energies. We repeated the fits using data up to 5×10^{17} Hz only. These model fits appear to describe rather well the overall shape of the optical/UV and X-ray spectrum of the source at the $\sim 5\%$ level, i.e. the data/model ratio is typically between 0.95 and 1.05 at all energies up to 5×10^{17} Hz). If we increase the error of the data points to this level, then the PLLP model fits the data well.

If we accept that PLLP model can parametrize the optical/UV and X-ray SED of the source then our results from the SED fitting of all observations can be summarized as follows:

- (1) The turn-over frequency correlates *positively* with the model spectral slope, and with the curvature parameter, b : as the turn-over energy increases, the spectrum steepens, and the curvature parameter increases.
- (2) Due to the above mentioned correlations, the peak frequency, ν_p and the curvature parameter b are also positively correlated. As ν_p shifts to higher energies, the spectral curvature also increases following the relation: $b \propto \sqrt{\nu_p}$.
- (3) We do not observe a strong correlation between the peak power, S_p , and the peak frequency, ν_p . If there is a relation between these two parameters, it is most probably an anti-correlation, in the sense that as the peak luminosity decreases, the peak frequency shifts to higher energies, roughly according to the relation: $S_p \propto 1/\nu_p$.

[Massaro et al. \(2008\)](#) considered a sample of blazars and observed an anti-correlation between E_p and b for five TeV blazars: PKS 0548 – 322, 1H 1426 + 428, Mrk 501, 1ES 1959 + 650, and PKS 2155 – 304. They also found a positive correlation between the spectrum peak power, S_p , and E_p . These correlations and anti-correlations were based on the results when a log-parabolic model was used to fit the X-ray spectra only. Clearly, our results regarding the relations between E_p, b and S_p are contrary to those reported by [Massaro et al. \(2008\)](#). However, they also studied PKS 2155-204, and found that the $S_p - \nu_p$ and $b - \nu_p$ relations in this object were different than the same relations for the other objects in their sample results. In fact, the observational relations presented in their Fig. 8 are quite similar to our plots shown in the right panel of Fig. 3.11.

From a phenomenological point of view, the PLLP model can be explained if the electron distribution at low energies follows a power-law up to a turn-over energy, and a log-parabolic shape at higher energies. If that is the case, our results indicate that this low-energy power-law branch is always present in PKS 2155 – 304. Furthermore, we can constrain the typical slope of the power-law energy distribution of the electrons, s , using the well-known relation between s and α' : $\alpha' = (s - 3)/2$. For the mean spectral index value of $\alpha' \sim -0.41$ in our case, we estimate that $s \sim 2.2$. This slope is fully consistent with predictions of models which assume first-order Fermi acceleration as being the primary acceleration mechanism in most collision less MHD shocks, as has been shown both analytically (e.g., [Bell \(1978\)](#); [Kirk et al. \(2000\)](#)) and numerically (e.g., [Bednarz & Ostrowski \(1998\)](#); [Baring et al. \(1999\)](#); [Ellison & Double \(2004\)](#)).

The presence of the log-parabolic branch in the electron distribution can be explained as in [Massaro et al. \(2004\)](#). These authors have shown that when the acceleration efficiency of particles is inversely proportional to the energy itself, then the energy distribution approaches a log-parabolic shape. They proposed that the log-parabolic spectra are naturally produced when the statistical acceleration probability have an energy dependency. According to this model the curvature, r , is related to the fractional acceleration gain ϵ by $r \propto [\log \epsilon]^{-1}$ and $E_P \propto \epsilon$, where E_P is the peak energy. This produces a negative trend in the relation between E_P and b (see [Tramacere et al. \(2009\)](#)).

An alternative explanation of the above trend is provided by the stochastic acceleration framework that includes a momentum diffusion term. The diffusion term plays a crucial role in the broadening of the spectral shape of the electrons ([Kardashev et al. \(1962\)](#); [Massaro et al. \(2006\)](#)). [Tramacere et al. \(2009\)](#) showed that the log-parabolic spectrum results from the evolution of a mono-energetic or quasi-mono-energetic particles injection under a Fokker-Planck equation with a momentum-diffusion term. [Kardashev et al. \(1962\)](#) have shown that the curvature term r is inversely proportional to the diffusion term D and the time t : $r \propto \frac{1}{Dt}$. This relation leads to the following connection between the peak frequency, the peak energy of the electron distribution, γ_p , and the spectral curvature b (Eqn. 5 of [Tramacere et al. \(2009\)](#)): $\ln(E_P) = 2\ln(\gamma_p) + 3/(5b)$.

Hence both the fractional acceleration gain term, ϵ , and the momentum diffusion term, D predict an anti-correlation between E_P and b . However, this opposite to what we observe. As we showed in Section 3.4, if there is a relation between E_P and b , this is a *positive*, and not a negative one.

The inability of the model to provide acceptable fits to the broad band optical/UV and X-ray SEDs of PKS 2155 – 304, as well as the positive correlation between E_p and b that we observe, perhaps indicates that the optical/UV and X-ray emission in this source are produced by two different populations of leptons. Optical/UV emission may be produced by slow leptons and the X-ray emission may be due to emission from much more energetic leptons, which may have been accelerated through the energy dependent particle acceleration mechanism. This possibility could also explain the fact that the optical/UV bands are well correlated with each other but not correlated with X-ray bands. Another possibility for positive correlation between E_P and b can arise within the stochastic acceleration framework if the cooling losses successfully compete with the acceleration and diffusion components (Tramacere et al. (2011)). However, only if we can analyse more SEDs, preferably including a wider range of EM bands, might the correlations between these parameters be clarified. That would definitely increase our understanding of the emission processes that dominate the spectra of blazars.

Chapter 4

Flux and Spectral Variability of the Blazar PKS 2155–304 with XMM-Newton: Evidence of Particle Acceleration and Synchrotron Cooling

4.1 Introduction

X-ray variability in HBLs is characterized by correlated changes of the spectral index with the X-ray flux and lags between soft and hard X-rays. A photon index-flux correlation was first observed by (George et al. (1988)) in Mrk 421 using *EXOSAT*. Similar results were also obtained for other HBLs (Giommi et al. (1990); Sambruna et al. (1994)). A soft lag in the HBL H 0323+022 in *Ginga* X-ray observations was observed for the first time by (Kohmura et al. (1994)).

¹Work presented in this chapter has been published in Bhagwan et al. (2016), *New Astronomy*, 2016, 44, 21-28

PKS 2155–304 ($\alpha_{2000.0} = 21^{\text{h}} 58^{\text{m}} 52.0^{\text{s}}$, $\delta_{2000.0} = -30^{\circ} 13' 32''$) at $z = 0.116$ is a HSP blazar that is highly variable across the entire EM spectrum (Gaur et al. (2010), and references therein). It is the brightest blazar in the UV to γ -ray bands in the southern hemisphere. Blazar variability is best studied throughout different phases which can be considered to be: outburst, pre/post outburst, and low states. PKS 2155 – 304 is one of the most commonly observed blazars for simultaneous multi-wavelength observations and has received maximum attention for simultaneous multi-wavelength observational campaigns (e.g. Urry et al. (1993); Urry et al. (1997); Brinkmann et al. (1994); Courvoisier et al. (1995); Edelson et al. (1995); Pesce et al. (1997); Pian et al. (1997); Marshall et al. (2001); Aharonian et al. (2005); Aharonian et al. (2009b); Dominici et al. (2006); Zhang et al. (2005); Zhang et al. (2006b); Dolcini et al. (2007); Piner et al. (2008); Sakamoto et al. (2008); Kapanadze et al. (2014); H.E.S.S. Collaboration et al. (2012)). This blazar has also been observed in assorted single EM bands over more diverse timescales. For instance, (Kastendieck et al. (2011)) have studied the long term optical variability, (Carini & Miller (1992)) have searched for intra-day and long term optical variability of this source. Gaur et al. (2010) have studied the X-ray intra-day variability in the blazar. There are some evidences for PKS 2155–304 have shown quasi-periodic oscillations (QPOs) on IDV time scales from *IUE* and *XMM-Newton* observations (Gaur et al. (2010); Urry et al. (1993); Lachowicz et al. (2009)). (Morini et al. (1986); Sembay et al. (1993)) observed PKS 2155–304 in the high flux state and detected pronounced spectral variations. Using *XMM-Newton* data (Zhang (2008)) have reported that the synchrotron emission of PKS 2155–304 peaked in UV–EUV bands rather than the soft X-ray band. Massaro et al. (2008) fitted the SED of PKS 2155–304 with a log-parabolic model and found that the curvature of the SED is anti-correlated with the peak energy E_p .

In a recent paper (Bhagwan et al. (2014)), we used all the archival *XMM-Newton* observations of PKS 2155 – 304 in order to study its broad band (optical/UV and X-ray) flux and spectral variability. We found that the long term optical/UV and X-ray flux variations in this source are mainly driven by model normalization variations. We also found that the X-ray band flux is affected by spectral variations. Overall, the energy

at which the emitted power is maximum correlates positively with the total flux. As the spectrum shifts to higher frequencies, the spectral “curvature” increases as well, in contrast to what is expected if a single log-parabolic model were an acceptable representation of the broad band SEDs. These results suggested that the optical/UV and X-ray emissions in this source may arise from different lepton populations.

We have now started the study of the individual *XMM-Newton* observations of the same source, with the aim to study its short term X-ray variability properties, since these data provide an excellent opportunity to analyse and model the blazar emission in different flux states with identical instrumentation. In this chapter, we present the results from the analysis of the *XMM-Newton* observation of PKS 2155 – 304 which was taken on 24 May 2002. The same data has been analyzed by (Zhang et al. (2005); Zhang et al. (2006b)). They have studied the short term variability and cross correlation analysis between the different X-ray energy bands. The observation includes three nearly equal length pointings at the blazar with a total exposure time of ~ 93 ks. But each exposure has been taken with different filters. We noticed that the combined light curve of these three pointings shows nearly stable flux states, declining flux states, rapid flares, and weak oscillations. We have found evidence for flux related spectral variations (which is typical of this source). We also find evidence (*for the first time*) for the presence of both “hard” and “soft” time lags, which are variable with time. Since the flux variability behaviour in this observation is rather typical of the source, we believe that the results we present in this chapter may be representative of the X-ray variability properties of the source. This will be confirmed when we will have finished the analysis of the remaining observations as well. The final results will hopefully offer us a more complete view on the physical processes which dominate the X-ray flux and spectral evolution in the source.

4.2 Data and Reduction

We analysed the archival *XMM-Newton* EPIC/pn data of the blazar PKS 2155–304 in the 0.3 – 10 keV X-ray band. These observations were made on 24 May 2002 (orbit

450, Obs ID 0124930501; PI: Fred Jansen). This observation ID has three continuous EPIC/pn exposures in small window (SW) mode with different filters: 450-1 was taken in the medium filter, 450-2 in the thin filter and 450-3 in the thick filter. The duration of the respective cleaned files are 31.7, 31.6 and 29.7 ks, respectively. The Original Data File (ODF) was reprocessed using Science Analysis System (SAS) version 11.0.0 with the most recent available calibration files.

By generating a hard band background light curve in the energy range 10–12 keV, we have checked for the high soft proton background periods which are caused by solar activity. We removed those points for which the hard band count rate was greater than 0.4 count/sec, and then we generated the good time interval (GTI) data. We have used the single and double events with quality and pattern flags constrained to $(FLAG = 0) \& (PATTERN \leq 4)$ for our analysis. We have carefully examined the pile-up effect in the data by SAS task *epatplot* and found that the data is indeed affected by pile-up. As a result, we extracted the source count from an annulus region which was centred on the source with inner radius of $10''$ and outer radius of $40''$. The background counts were accumulated from a circular region of radius $45''$ on the CCD chip near where the source was located and least affected from the source counts.

We extracted background subtracted light curves by using the *epiclccorr* command. The spectral analysis was done by using the *xmmselect* and *specgroup* tasks in SAS. We have used the task *specgroup* to rebin all spectra, in order to have at least 50 counts for each background subtracted spectral channel and the value of over sampling parameter is taken as 5.

4.3 Excess Variance

The measurement uncertainties contribute an additional variance to the data. The variance remaining after subtracting the expected contribution of measurement error is called excess variance. [Nandra et al. \(1997\)](#) and [Edelson et al. \(2002\)](#) have used excess variance as an estimator of the intrinsic source variance and we summarize that approach

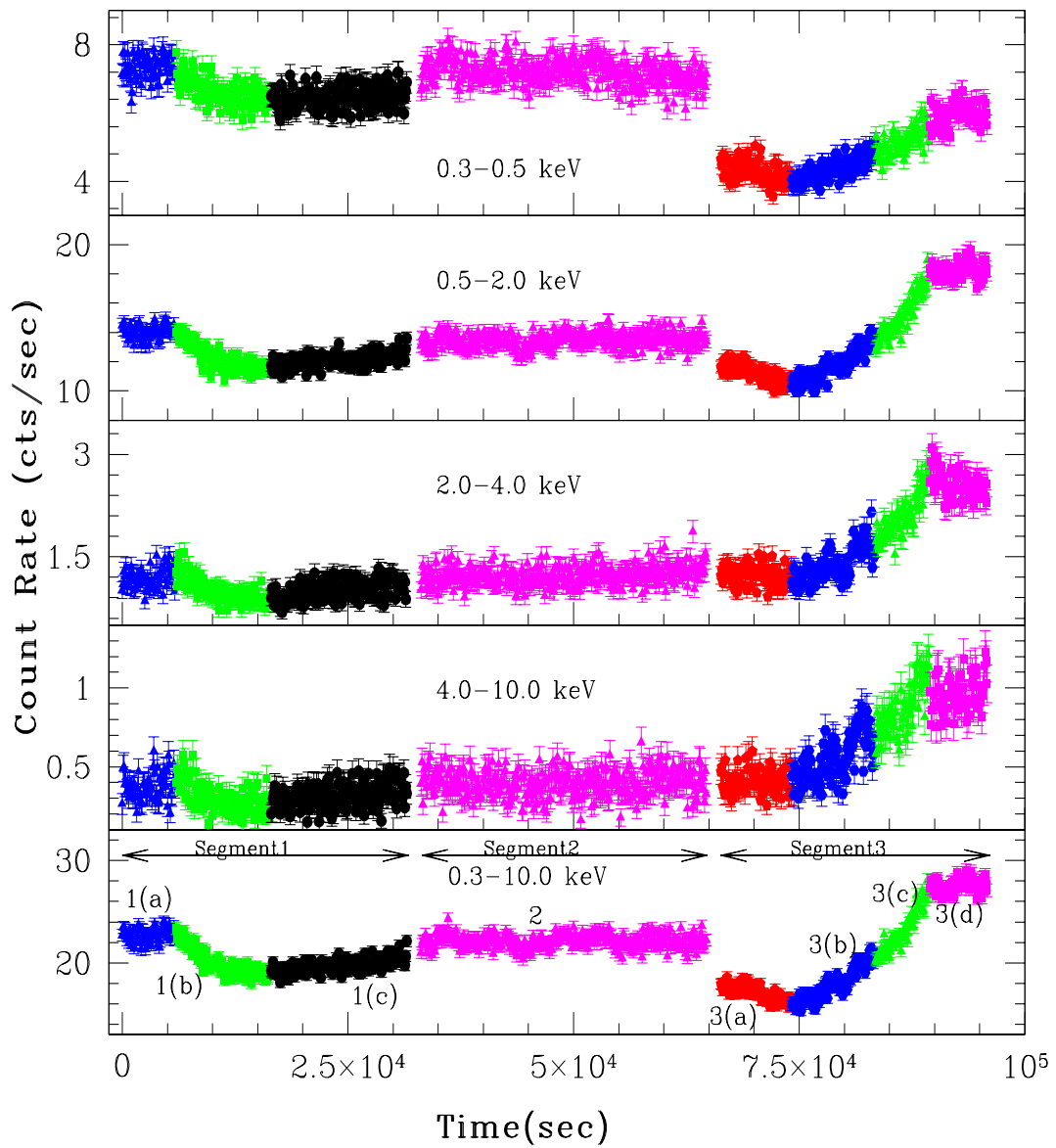


Figure 4.1 The background subtracted X-ray light curve of PKS 2155-304 in different energy bands.

here. It is defined as

$$\sigma_{EX}^2 = V^2 - \overline{\sigma_{err}^2} , \quad (4.1)$$

where

$$V^2 = \frac{1}{N-1} \sum_{i=1}^N (x_i - \bar{x})^2 , \quad (4.2)$$

and

$$\overline{\sigma_{err}^2} = \frac{1}{N} \sum_{i=1}^N \sigma_{err,i}^2 , \quad (4.3)$$

where \bar{x} , $\overline{\sigma_{err}^2}$ and N are the mean, mean square error and total number of data points in the light curve, respectively.

The normalized excess variance is expressed by $\sigma_{NEX}^2 = \sigma_{EX}^2 / \bar{x}^2$ and the fractional root mean square variability amplitude (F_{var} ; [Edelson et al. \(1990\)](#); [Rodríguez-Pascual et al. \(1997\)](#); [Vaughan et al. \(2003\)](#)) is expressed as the square root of the normalized excess variance:

$$F_{var} = \sqrt{\frac{V^2 - \overline{\sigma_{err}^2}}{\bar{x}^2}} . \quad (4.4)$$

Obviously F_{var} and σ_{NEX}^2 convey the same information but F_{var} is more often used in the literature and it conveniently gives the root mean square (rms) variability amplitude in term of percentages. Through Monte Carlo simulations, [Vaughan et al. \(2003\)](#) estimated the errors in F_{var} and σ_{NEX}^2 , and they found that the error on σ_{NEX}^2 decreases when the signal to noise ratio (S/N) increases according to

$$(\sigma_{NXS}^2)_{err} = \sqrt{\left(\sqrt{\frac{2}{N}} \frac{\sigma_{err}^2}{\bar{x}^2}\right)^2 + \left(\sqrt{\frac{\sigma_{err}^2}{N}} \frac{2F_{var}}{\bar{x}}\right)^2}, \quad (4.5)$$

$$(F_{var})_{err} = \sqrt{\left(\sqrt{\frac{1}{2N}} \frac{\sigma_{err}^2}{\bar{x}^2 F_{var}}\right)^2 + \left(\sqrt{\frac{\sigma_{err}^2}{N}} \frac{1}{\bar{x}}\right)^2}. \quad (4.6)$$

4.4 Results

4.4.1 Light Curves

We present the light curves extracted from entire observation of PKS 2155–304 in the five energy bands of 0.3–0.5 keV, 0.5–2.0 keV, 2.0–4.0 keV, 4.0–10.0 keV and 0.3–10.0 keV (with an 100s binning) in Fig. 4.1. As mentioned above, this observation consists of three exposures with a duration 31.7, 31.6 and 29.7 ks, respectively. The gaps between the individual exposures are of the order of ~ 1.5 ks. The three sub-parts are easily spotted by the abrupt change in the source flux. For example, the flux drop at around ~ 65 ks since the start of the observation is not real, but is due to the change of the EPIC/pn filters, since the EPIC/pn thin filter is more transparent to the soft energy photons than the thick filter. A similar effect, but of a much smaller amplitude, is observed ~ 30 ks since the start of the observation, when the EPIC/pn filter was switched from medium to thin.

Despite the EPIC/pn filter changes, a visual inspection indicates significant and clearly defined flux variability in the light curve. In Fig. 4.1, the individual exposures are marked as segments 1, 2, and 3. We divided segment 1 into three sub-segments: 1(a) where the source flux is almost constant; 1(b) where the flux decreases; and 1(c) where the source flux rises. Segment 2 is relatively flat, but this is when the source has shown a hint of a QPO (Gaur et al. (2010)). Segment 3 is divided into four sub-segments: 3(a), with decreasing flux, 3(d) corresponds to the \sim constant flux level towards the end of

the observation, while 3(b) and 3(c) are defined during the first and second part of the strong rising flux state in between. The percentage variability and signal to noise ratio (S/N) of segment 1, 2 and 3 in 0.3 – 10.0 keV band are 6.6 ± 0.16 , 1.5 ± 0.22 , 21 ± 0.15 and 37.7, 39.3, 38.0, respectively.

4.4.2 Spectral Variability

To investigate if there are spectral variations associated with the well defined flux variations, we generated the spectra of the eight sub-segments we discussed above. We then fitted a simple power law (PL) model to the X-ray spectra using XSPEC (v. 12.8.0). The average value of Galactic neutral hydrogen absorption was found from the High Energy Astrophysics Science Archive Research Centre (HEASARC) N_H calculator to be $N_H = 1.71 \times 10^{20} \text{ cm}^{-2}$ (Dickey & Lockman (1990)). We kept this value fixed in all the spectral fits.

The best model fit results (reduced χ^2 values and model parameters with their corresponding 90% confidence level) are summarized in Table 4.1. In the last three columns of the same Table we list the best-fit flux estimates (together with their 90% confidence limits) in the 0.3–2, 2–10 and 0.3–10 keV bands. The best fit PL models, and ratios of data to model are plotted in Fig. 4.2 for all the segments. Based on the null probability for the PL model fits (listed in the 7th column of the upper part of Table 4.1), the model provides statistically acceptable fits to the spectra of all segments. The exception are the spectra of segments 3(b) and 3(d), in particular, where the probability is low. The data-to-model ratios for segments 3(d) (bottom right panels in Fig. 4.2) show a convex shape above ~ 2 or 3 keV. This shape is indicative of a more complex spectral shape. For that reason, we also fitted the spectra with a broken power-law model (BKPL). The best BKPL model fit results are also listed in Table 4.1. The model resulted in entirely unconstrained break-energies, and almost identical Γ_1 and Γ_2 best fit values, in the case of segments 1(a), 1(b), 1(c). These results imply that a single PL model is adequate for the characterization of the energy spectra of these segments. For this reason, we do not list the BKPL best-fit results for these segments in Table 4.1.

Table 4.1 Results of X-ray spectral fitting with power law and broken power law in the energy range of 0.3-10 keV band for PKS 2155–304.

Segment	Γ_1	N^a	E_{break}	Γ_2	χ^2/dof	Prob.	Flux ^b	Flux ^c	Flux ^d
Power-Law (PL) Model									
1(a)	$2.66^{+0.01}_{-0.01}$	$3.04^{+0.02}_{-0.02}$	151.8/142	0.27	$1.010^{+0.003}_{-0.004}$	$0.305^{+0.003}_{-0.003}$	$1.315^{+0.004}_{-0.005}$
1(b)	$2.70^{+0.01}_{-0.01}$	$2.65^{+0.01}_{-0.01}$	157.1/157	0.48	$0.898^{+0.002}_{-0.002}$	$0.250^{+0.002}_{-0.002}$	$1.148^{+0.003}_{-0.003}$
1(c)	$2.68^{+0.01}_{-0.01}$	$2.63^{+0.02}_{-0.01}$	185.0/177	0.34	$0.882^{+0.002}_{-0.002}$	$0.255^{+0.002}_{-0.002}$	$1.137^{+0.003}_{-0.003}$
2	$2.58^{+0.01}_{-0.01}$	$2.86^{+0.01}_{-0.01}$	222.5/207	0.22	$0.921^{+0.001}_{-0.001}$	$0.320^{+0.001}_{-0.001}$	$1.241^{+0.002}_{-0.002}$
3(a)	$2.56^{+0.01}_{-0.01}$	$3.04^{+0.02}_{-0.02}$	172.4/156	0.17	$0.973^{+0.004}_{-0.003}$	$0.347^{+0.003}_{-0.003}$	$1.321^{+0.004}_{-0.005}$
3(b)	$2.46^{+0.01}_{-0.01}$	$3.16^{+0.02}_{-0.02}$	205.8/174	0.05	$0.976^{+0.004}_{-0.004}$	$0.420^{+0.003}_{-0.003}$	$1.395^{+0.005}_{-0.004}$
3(c)	$2.32^{+0.01}_{-0.01}$	$4.12^{+0.02}_{-0.02}$	182.9/178	0.38	$1.217^{+0.004}_{-0.004}$	$0.676^{+0.006}_{-0.005}$	$1.885^{+0.007}_{-0.007}$
3(d)	$2.32^{+0.01}_{-0.01}$	$4.89^{+0.02}_{-0.02}$	247.3/179	5.5e-4	$1.444^{+0.004}_{-0.005}$	$0.793^{+0.006}_{-0.006}$	$2.236^{+0.007}_{-0.005}$
Broken-Power-Law (BKPL) Model									
2	$2.58^{+0.01}_{-0.01}$	$2.86^{+0.01}_{-0.01}$	$3.27^{+2.16}_{-0.78}$	$2.65^{+0.17}_{-0.04}$	210.7/205	0.38 (4.0e-3)	$0.921^{+0.002}_{-0.001}$	$0.315^{+0.002}_{-0.002}$	$1.236^{+0.003}_{-0.002}$
3(a)	$2.55^{+0.01}_{-0.02}$	$3.05^{+0.02}_{-0.02}$	$2.95^{+0.83}_{-1.50}$	$2.69^{+0.10}_{-0.09}$	160.3/154	0.35 4.0e-3	$0.972^{+0.003}_{-0.003}$	$0.338^{+0.005}_{-0.004}$	$1.310^{+0.007}_{-0.004}$
3(b)	$2.49^{+0.02}_{-0.02}$	$3.13^{+0.02}_{-0.03}$	$1.26^{+0.60}_{-0.25}$	$2.42^{+0.02}_{-0.03}$	190.4/172	0.16 (1.2e-3)	$0.977^{+0.004}_{-0.003}$	$0.431^{+0.003}_{-0.004}$	$1.408^{+0.007}_{-0.005}$
3(c)	$2.35^{+0.03}_{-0.02}$	$4.08^{+0.03}_{-0.07}$	$1.26^{+0.50}_{-0.44}$	$2.28^{+0.02}_{-0.02}$	170.2/176	0.61 (1.8e-3)	$1.220^{+0.005}_{-0.005}$	$0.683^{+0.009}_{-0.006}$	$1.902^{+0.011}_{-0.007}$
3(d)	$2.30^{+0.01}_{-0.01}$	$4.90^{+0.02}_{-0.02}$	$4.93^{+0.47}_{-1.15}$	$2.85^{+0.22}_{-0.31}$	196.3/177	0.15 (1.3e-9)	$1.442^{+0.005}_{-0.004}$	$0.761^{+0.008}_{-0.007}$	$2.203^{+0.010}_{-0.008}$

^a Normalization constant in units of 10^{-2} photon $\text{cm}^{-2}\text{s}^{-1}\text{keV}^{-1}$ ^b Unabsorbed 0.3–2.0 keV model flux in units of 10^{-10} erg cm^{-2} s^{-1} ^c Unabsorbed 2.0–10.0 keV model flux in units of 10^{-10} erg cm^{-2} s^{-1} ^d Unabsorbed 0.3–10.0 keV model flux in units of 10^{-10} erg cm^{-2} s^{-1}

Contrary to this, the BKPL best-fit χ^2 values are smaller than the respective PL best-fit values, for the remaining segments. The numbers in parenthesis in the 7th column of Table 4.1 indicate the probability of the F -statistic given the χ^2 values of the PL and BKPL best-fits. Based on the F -ratio probabilities, the improvement in the fit when we consider the BKPL model is significant at more than the 99% level in the case of segment 2 and all sub-segments of the last part of the observation.

Our results indicate that during segments 2 and 3(a), when the flux remains rather constant, the spectra steepen above the break energy by an average $\Delta\Gamma = 0.11 \pm 0.08$. A stronger spectral steepening, by a factor of $\Delta\Gamma = 0.55 \pm 0.27$ is also observed during segment 3(d), when the flux remains again \sim constant, albeit at a higher than previous level. In all these three cases, the break-energy is rather high, with an average value of 3.4 ± 0.7 keV. On the contrary, the strong flux rise observed during segments 3(b) and 3(c), is associated with a small, but significant, spectral hardening at high energies, of $\Delta\Gamma = -0.07 \pm 0.02$, between the spectral slope below and above the break-energy. At the same time, the average break energy for these segments is 1.26 ± 0.32 , which is significantly smaller than the break-energy in the spectra of segment 3(d).

“Log-parabolic” models have also been used to describe continuously downward-curving spectra of HSPs (Massaro et al. (2004)). We fitted the spectra of all segments with such a model, but the quality of the fits are not significantly better than that of the PL fits. In fact, in some cases, the χ^2 values are even larger than those from the PL fits (for a smaller number of dof). The best-fit curvature parameter turns out to be negative only for segments 1(b) and 1(c), but even in this case, the values are consistent with zero within the errors.

Using the PL best-fit results, we investigated whether the spectral variations are related with the flux variations of the source. Fig. 4.3 shows a plot of the spectral PL index¹ as a function of the source 2–10 keV flux. In general, we find that the spectral slope is anti-correlated with flux; the spectra “harden” with increasing flux. Using the data plotted in Fig. 4.3, we find a correlation coefficient of $r = -0.95$, which is significant

¹Note that the plot in Fig. 4.3 does not change if we use the best-fit Γ_1 values from the BKPL fits, as they are almost identical to the best-fit Γ values of the PL fits.

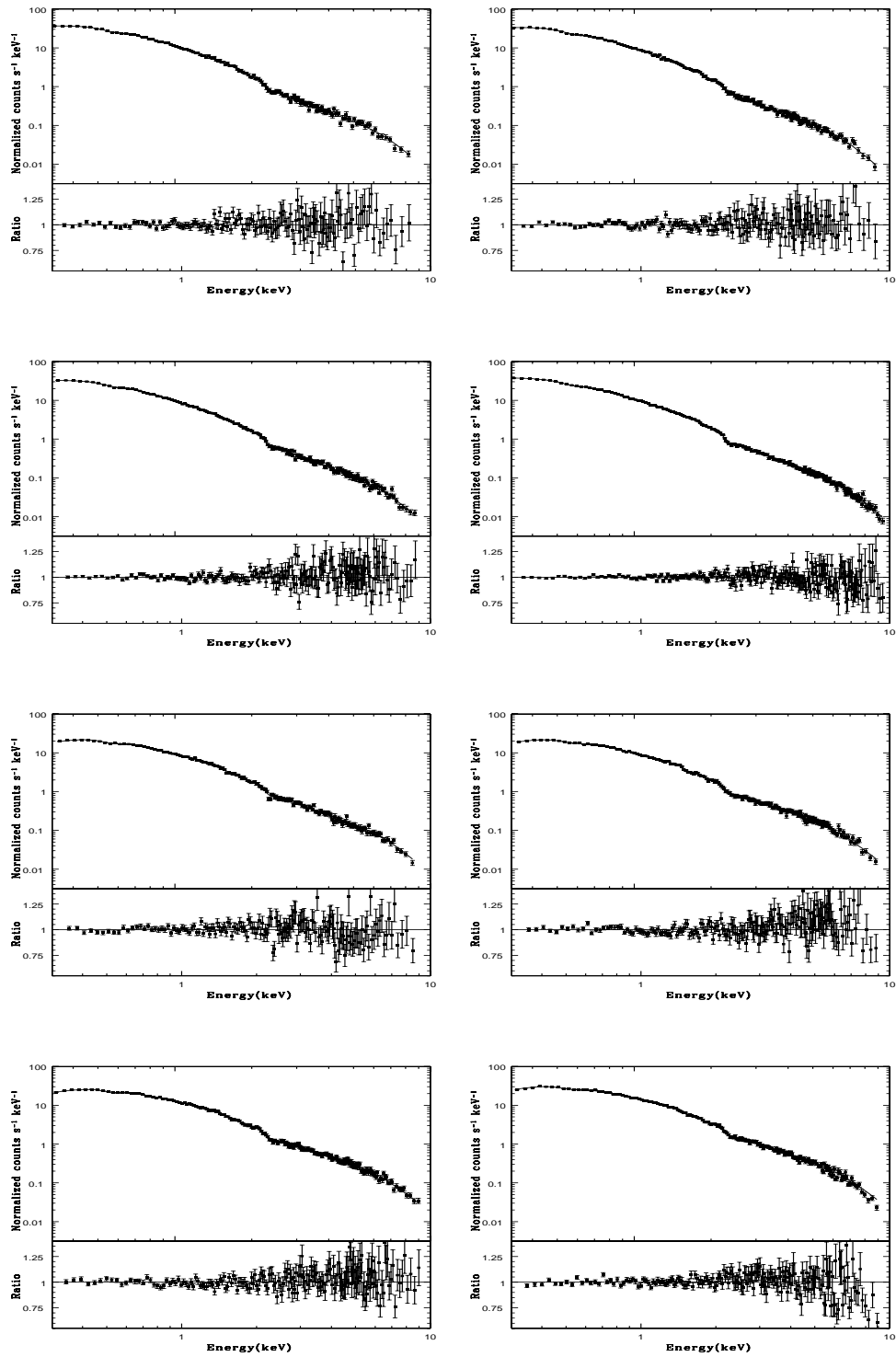


Figure 4.2 The pn count rate spectra corresponding to the various segments of observation ID 0124930501 with best fitting simple power-law models and data-to-model ratios. Top row (left to right) have sub-segment 1(a) & 1(b); second row have 1(c) & 2; third row 3(a)& 3(b) and the last row 3(c)& 3(d).

and better than 99% confidence level ($P_{null} = 3.0 \times 10^{-4}$). Looking the data in more detail, the source flux and spectral index are similar for the first three segments (1a, 1b and 1c), while the spectral index flattens as the 2–10 keV flux increases during segments (2) and (3a). Taken as a whole, the spectral-flux evolution from (1a) to (3) may exhibit a “clockwise trajectory” in the “spectral slope – flux” plane shown in the Fig. 4.3, although the flux and spectral variations are not of very large amplitude. The spectrum shows a strong “hardening” during the strong flux rise towards the end of the observation shown in the Fig. 4.3.

4.4.3 Correlation Analysis

The spectral variations reported in the previous section suggest possible energy delays in the observed flux variations. In order to investigate further the spectral variability of the source, we estimated the Cross-Correlation Function (CCF) between light curves at different energy bands, using light curves with a 100 s bin size. We chose light curves in the energy bands 0.3–0.5, 0.5–2, 2–4 and 4–10 keV. We calculated the sample CCF as in Section 3 of (Brinkmann et al. (2005)), and we estimated the CCF between the 4–10, 2–4, and 0.5–2 keV band light curves versus the 0.3–0.5 keV band light curve. Significant correlation at positive lags means that soft (i.e. the 0.3–0.5 keV) band variations are leading the variations in the “harder” band.

We followed a similar, but simplified, version of the “sliding window ” technique of (Brinkmann et al. (2005)). We calculated the CCFs for 10 ks intervals, which started at different times of the observed light curves. More specifically, we used 10 ks data streams which started at the points $t_{\text{start}} = 0, 500, 1000, \dots$ s since the start of the observation. As a result, we computed the CCF for ~ 170 , 10 ks long segments for the complete light curve. For each CCF, we identified the lag, τ_{max} , at which the CCF was maximum (i.e. CCF_{max}), and calculated the mean time lag, τ_{mean} , as the mean of the time lags of the points with CCF values larger or equal to $0.8 \times \text{CCF}_{\text{max}}$, in the case when: a) the CCF_{max} value was larger or equal to 0.8, and b) there were at least five points with a CCF value larger than 0.8 of CCF_{max} . In other words, we have only considered CCF peaks which are strong, broad and well defined, as opposed to random, narrow

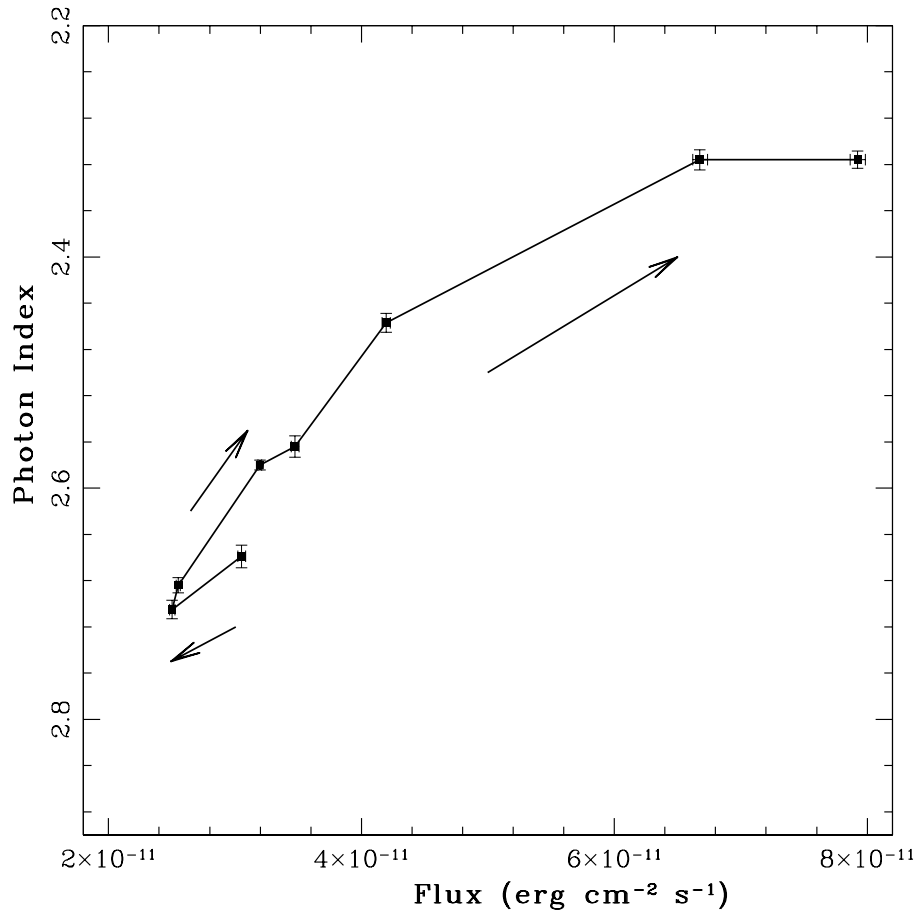


Figure 4.3 Photon-index versus the 2.0-10.0 keV flux plot

peaks in the CCF. Finally, we did not consider light curve segments in the time intervals between 21.7-43 ks and 54.6-76 ks after the start of the observation, as in this case, the light curves would include data during the EPIC/pn filter switches (which affect in a different way the observed count rate in the soft and harder energy bands).

The above procedure allows us to monitor the temporal variation of the time lag between various bands. Our results are plotted in the Fig. 4.4. The top panel of figure shows the 4–10 keV band light curve (which is the most representative of the intrinsic source variations, as this band is less affected by the filter changes). The bottom panel of the figure shows the average time lag between the 0.5–2, 2–4 and 4–10 keV band light curves and the 0.3–0.5 keV band light curve (red filled circles, blue open circles, and black filled circles, respectively). The vertical dashed lines in the top panel indicate the light curve

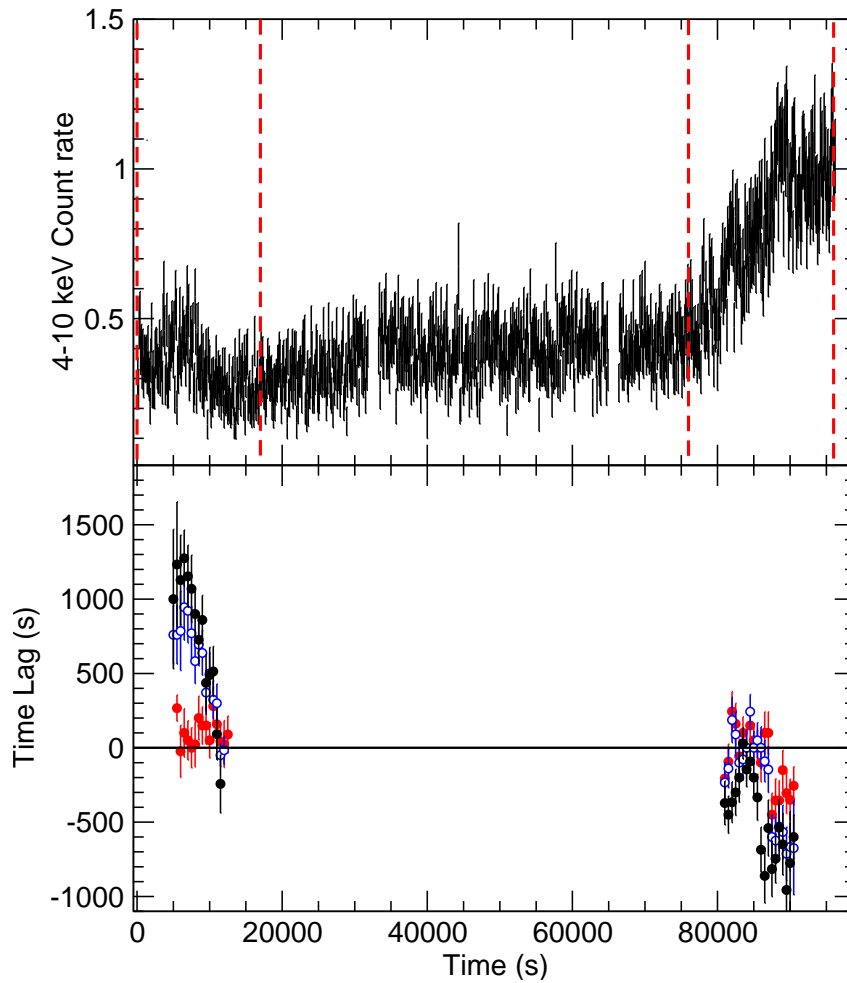


Figure 4.4 4–10 keV band light curve (top panel) together with the temporal variation of the delays between the 0.3–0.5 keV band light curve and the 0.5–2, 2–4 and 4–10 keV band light curves, in the bottom panel (red filled circles, blue open circles and black field circles, respectively).

segments that were used to estimate the mean time lags plotted in the bottom panel. In addition to the intervals that we excluded for the estimation of the CCF, the resulting CCF for the intervals $\sim 17 - 22$ ks and $43 - 55$ ks did not show any significant peaks in them. This is most probably due to the fact that all light curves were relative flat during these periods, with very low amplitude variations, roughly similar to the Poisson noise variations (specially in the high energy bands). Consequently, the sample CCFs are not capable to detect any intrinsic delays in these periods.

Our results indicate that the correlation between the “soft” and “hard” bands is rather complex. In the first part of the observation (the part which corresponds to segments

(1a), (1b) and the first part of segment (1c) the lags are *positive*, i.e. the variations in the 0.3–0.5 keV band are *leading* those in the harder bands (i.e. we observe a *hard lag*). In this case, whatever the characteristic time scales which dominate the observed variations, they must be faster at low energies. Furthermore, the time lags between the highest energy bands (4–10 and 2–10 keV) and 0.3–0.5 keV appear to decrease with time, from ~ 1.5 to ~ 0 ks. At the same time, the 0.5–2 vs 0.3–0.5 keV lags appear to be constant at ~ 100 s.

The reverse situation is observed in the last part of the observation, ~ 80 ks after the start of the observation, during the continuous, large amplitude flux rise. During the flux rise, the time delays between 0.5–2 and 0.3–0.5 keV, as well as between the 2–4 and 0.3–0.5 keV bands are consistent with zero, while the 4–10 keV band variations may be *leading* the soft band variations. When the source flux flattens after ~ 85 ks, the harder band variations are clearly *leading* the soft band variations (i.e. we observe a *soft lag*). The delay is energy dependent: the 0.3–0.5 keV band variations are delayed with respect to the 4–10 and 2–4 keV band variations by ~ 700 s, while the time lag between the 0.5–2 and the 0.3–0.5 keV bands is ~ 300 s.

4.5 Discussion and Conclusions

We have studied the flux and spectral variability of PKS 2155–304 using a ~ 100 ks *XMM-Newton* observation. The flux variability detected in this observation is rather typical of this source; we observe a short flare, decaying and stable flux states, as well as a rapid, large amplitude flux increase towards the end of the observation. We performed a time-resolved spectroscopic analysis, by dividing the data in various segments with different mean flux, and we fitted a simple power-law model to them.

4.5.1 The spectral variability results

In general, X-ray spectra of HSPs are rather steep ($\Gamma > 2$) and continuously steepen with increasing energies (Perlman et al. (2005); Tramacere et al. (2007)). As a result,

X-ray spectra of HSPs follow a convex, or continuously downward-curved, shape. This is a signature of the high energy tail of synchrotron emission that is the outcome of energy dependent particle acceleration and cooling (Massaro et al. (2004)). In the last decade, X-ray observations of PKS 2155–304 by various X-ray telescopes have shown that its spectra normally has a convex shape below 10 keV (Massaro et al. (2008); Foschini et al. (2006); Kataoka et al. (2000); Zhang et al. (2002); Aharonian et al. (2009a)). However, two observations by *XMM-Newton* of this blazar in 2006 were analyzed by (Zhang (2008)) and he reported that the shape of those X-ray spectra were concave.

Our observations indicate that a simple power-law model can describe adequately the source’s spectra during the first part of the observation, when we observe a mini-flare. In the rest of the observation, our analysis indicate that the energy spectra are more complex. We observe a spectral steepening above ~ 3.4 keV, by a factor of $\Delta\Gamma \sim 0.1–0.5$ during segments 2, 3(a) and 3(d), when the flux remains rather constant.

In addition, during the flux rise detected towards the end of the observation (segments 3b and 3c) the X-ray spectra show the opposite behaviour; we observe a spectral hardening, of low amplitude ($\Delta\Gamma \sim 0.1$, above $\sim 1–1.5$ keV). This could be an indication of the low-energy side of the Inverse Compton emission contributing to energies even below 10 keV. A detailed, similar analysis of all the available *XMM-Newton* observations of the source, could provide useful information regarding the spectral hardening/softening (amplitude of $\Delta\Gamma$ and location of E_{break}) and its relation to the flux variations of the source.

When we plotted the spectral index as a function of flux, we found that the typical “flatter when brighter” spectral variability behaviour, in agreement with previous studies (Zhang et al. (2006b); Kapanadze et al. (2014); Zhang et al. (2002)). This anti-correlation between spectral slope and source flux is a signature of spectral flattening with increasing flux, and indicates that the hard X-ray band flux increases more than the soft X-ray band flux as the flux increases. There is an indication of spectral variations along a “clockwise” trajectory on the spectral slope – flux plane, but the evidence is not very strong.

4.5.2 The cross-correlation results

We also performed a detailed cross-correlation analysis of the variations detected, by dividing the light curve into 4 energy bands. We detected both hard lags, as well as soft lags, in the first and last part of the observation, respectively. To the best of our knowledge, this is the first time that both hard and soft lags are detected in a light curve of this source.

In the simplest case scenario, the X-ray emission variation of HSPs is controlled by the energy dependent particle acceleration and cooling mechanisms. The cooling process is well understood but particle acceleration is not well understood yet and could operate in different ways (Katarzyński et al. (2005); Zhang (2002)). Following Zhang (2002), the acceleration timescale, t_{acc} , of the relativistic electrons, and their cooling time scale, t_{cool} , in the observed frame, can be expressed as a function of the observed photon energy E (in keV) as follows:

$$t_{\text{acc}}(E) = 9.65 \times 10^{-2} (1+z)^{3/2} \xi B^{-3/2} \delta^{-3/2} E^{1/2} \text{s}, \quad (4.7)$$

and,

$$t_{\text{cool}}(E) = 3.04 \times 10^3 (1+z)^{1/2} B^{-3/2} \delta^{-1/2} E^{-1/2} \text{s}, \quad (4.8)$$

where z is the source redshift, B is the magnetic field (in Gauss), δ is the Doppler factor of the emitting region, and ξ is a parameter describing how fast the electron can be accelerated.

Equations (4.7) and (4.8) show that both t_{cool} and t_{acc} depend on the observed photon energy but do so in an inverse fashion. The lower energy electrons are radiating low energy photons which cool slower but are accelerated faster than the high energy electrons that are radiating the high energy photons. The relationship between t_{cool} and t_{acc} can in principle give an important clue about the process that dominates the X-ray emission.

If t_{cool} is significantly larger than t_{acc} , the cooling process dominates (Kirk et al. (1998)). In this case, any change in emission will propagate from higher to lower energies so that

higher energy photons will lead lower energy photons (soft lag) and a clockwise loop of spectral index against the flux will be observed. The expected soft lag should be approximately equal to

$$\tau_{\text{soft}} = t_{\text{cool}}(E_l) - t_{\text{cool}}(E_h), \quad (4.9)$$

where τ_{soft} is the observed soft lag, and the values of E_l and E_h are the energy of the lower and higher energy bands in units of keV, respectively.

In contrast, if t_{acc} is comparable to the t_{cool} in the observed energy range, the system is dominated by acceleration processes and any variation in emission propagates from lower to higher energies because it takes a longer time to accelerate a particle to higher energies. In this case there would be a hard lag and an anti-clockwise loop would be observed in spectral index versus flux plot. The time lag in an acceleration dominated system is expressed as,

$$\tau_{\text{hard}} = t_{\text{acc}}(E_h) - t_{\text{acc}}(E_l), \quad (4.10)$$

where τ_{hard} is the observed hard lag between the low and high energy bands, respectively.

4.5.3 Implications of the hard lags

Based on this scenario, the hard lag we observe in the first part of the observation may indicate that the system is dominated by acceleration processes. We observe that $\tau_{\text{hard}}(4 - 10 \text{ vs } 0.3 - 0.5) > \tau_{\text{hard}}(2 - 4 \text{ vs } 0.3 - 0.5) > \tau_{\text{hard}}(0.5 - 2 \text{ vs } 0.3 - 0.5)$, which is easy to understand since the energy separation of these bands increases accordingly. Using equations (4.7) and (4.10), we can show that, in this case, we should expect that

$$B\delta\xi^{-2/3} = 0.21(1+z)E_h^{1/3} \left[\frac{1 - (E_l/E_h)^{1/2}}{\tau_{\text{hard}}} \right]^{2/3}. \quad (4.11)$$

We found that $\tau_{\text{hard}}(4 - 10 \text{ vs } 0.3 - 0.5)$ and $\tau_{\text{hard}}(2 - 4 \text{ vs } 0.3 - 0.5)$ do not remain constant, but rather decrease with time. According to eq. (4.11), this would imply that either B and/or δ increase with time, or that the parameter ξ decreases with time. We also observed that $\tau_{\text{hard}}(0.5 - 2 \text{ vs } 0.3 - 0.5)$ to remain constant in the same period. This result indicates that neither B nor δ should control the variations with time of the

τ_{hard} in the higher energy bands, as in this case we would expect these lags to decrease with time.

One possibility is that the acceleration process dominates the variations above 2 keV, but at lower energies a different variability process dominates the observed variations. This is though highly unlikely, given the very good correlation between the variations below and above 2 keV. Perhaps then, the variability in the first part of the observation is dominated by acceleration process, and that the rate of acceleration, ξ , does not remain constant, but rather decreases with time. In addition, if a variable ξ determines the variability evolution of the system then, apart from being time dependent, it may also be energy dependent, in which case the constant low-energy time lags could also be explained.

The probability of the system to be “acceleration dominated” contradicts the spectral slope - flux evolution in the first part of the observation. Our spectral analysis suggests a clockwise trajectory in the spectral index versus flux plot during the first part of the observation. Arguably the amplitude of this “trajectory” is not very strong, but it is fair to notice that we find no evidence of an “anti-clockwise” evolution, which is what we would expect if the acceleration process dominates the variability evolution of the source. We cannot offer an interpretation at the moment, as to why could be the reason for these seemingly contradictory results.

4.5.4 Implications of the soft lags

On the other hand, the soft lags we observe in the last part of the observation suggest that the system is dominated by cooling processes. We observe again that $\tau_{hard}(4 - 10 \text{ vs } 0.3 - 0.5) > \tau_{hard}(2 - 4 \text{ vs } 0.3 - 0.5) > \tau_{hard}(0.5 - 2 \text{ vs } 0.3 - 0.5)$ (in absolute value), which can be again understood due to the accordingly increasing energy separation of these bands. Using equations (4.8) and (4.9), we expect that, in this case,

$$B\delta^{1/3} = 209.91 \left(\frac{1+z}{E_l} \right)^{1/3} \left[\frac{1 - (E_l/E_h)^{1/2}}{\tau_{soft}} \right]^{2/3}. \quad (4.12)$$

The above equation indicates that the observed time lags should be inversely proportional either to the magnetic field B of the emitting blob ($B \propto \tau^{-2/3}$) and/or to δ ($\delta \propto \tau^{-2/3}$). In the last part of the observation, we observe that all soft lags remain roughly constant. Their absolute mean values at times longer than 85 ks (since the start of the observation) are: $\langle \tau_{soft}(4 - 10 \text{ vs } 0.3 - 0.5) \rangle = 726 \pm 54 \text{ s}$, $\langle \tau_{soft}(2 - 4 \text{ vs } 0.3 - 0.5) \rangle = 625 \pm 25 \text{ s}$, and $\langle \tau_{soft}(0.5 - 2 \text{ vs } 0.3 - 0.5) \rangle = 317 \pm 36 \text{ s}$. Assuming that $\delta t = 10$ and that it remains constant during the observation, then the above values together with eq. (4.12), result in the following estimates for the magnetic field strength: $1.8 \pm 0.2 \text{ G}$, $1.5 \pm 0.05 \text{ G}$, and $1.5 \pm 0.1 \text{ G}$. The weighted mean value is $1.5 \pm 0.05 \text{ G}$, which is similar to the magnetic field values that result from the broad band SED fitting of blazars (Ghisellini et al. (2010)). We note that, according to our results, τ_{soft} is much smaller by a factor of $\sim 5 - 6$ (for all energy bands) during the flux rise (at times $\sim 75 - 85 \text{ ks}$). This would imply an *increased* magnetic field value, by a factor of ~ 3 during the flux rise phase.

Zhang et al. (2006b) have analysed the same observations and done cross correlation analysis in which they divided the each exposure light curve in three energy (e.g., 0.2-0.8 keV (soft), 0.8-2.4 keV (medium) and 2.4-10.0 keV (hard)) bands. In their analysis they have calculated the time lags between soft/medium and soft/hard energy bands. They have found the soft band variations lag behind the medium and hard band by $\sim 450 \pm 300$, $\sim 870 \pm 540$ and $\sim 420 \pm 180$, $\sim 1280 \pm 240$ seconds, respectively in segment 1 and 3 of the light curves. Our results are comparable to these results in segment 3 and opposite in segment 1.

4.5.5 Summary

Our analysis suggest the presence of soft lags in some epochs and hard lags in other epochs, during the 24 May 2002 XMM-Newton observation of PKS 2155 – 304. This result implies that the difference between t_{acc} and t_{cool} of the emitting electrons is changing from epoch to epoch, in agreement with past studies (Zhang et al. (2006b); Zhang et al. (2002); Aharonian et al. (2009a)).

Hard time lags are detected during the first part of the observation. These lags suggest that the flux evolution during this part of the observation is dominated by the acceleration process. These delays may be modulated by variations of the acceleration parameter ξ in time, and perhaps in energy as well. The shock formation process due to collision is the most acceptable reason for particle acceleration (Spada et al. (2001); Mimica et al. (2005)). If real, the variation in the value of ξ indicates that the particle acceleration mechanisms may be time variable. Using the soft time lags observed in the last part of the observation we have estimated the value of the magnetic field, which turns out to be similar to the values that have been reported in the literature, based on the modelling of the full band SEDs of blazars. We also found evidence for the magnetic field variations, during the flux rise phases in the light curve.

The X-ray observations are the most powerful diagnostic tool for blazars which have an ability to provide information about the physical processes taking place in the vicinity of the central engines of these sources. We believe that our results demonstrate that, in order understand the relationship between particle acceleration and cooling, combined spectral and timing studies within the X-ray band can be useful. Future, similar studies of the archival XMM-Newton observations of this source may allow us to understand better the physical processes that control the flux and spectral variations in this source.

Chapter 5

Multi-band Optical Variability of Three TeV Blazars on Diverse Timescales

5.1 Introduction

Miller et al. (1989) found the first clear evidence of optical IDV. Carini (1990) found IDV in more than 80% of blazars when the duration of observations exceeded 8 hrs. Later, Gupta & Joshi (2005) studied a larger sample of AGNs and detected significant IDV in $\sim 10\%$ of radio-quiet Active Galactic Nuclei (RQAGNs), 35–40% of RLAGNs (excluding blazars) when observed for ~ 6 hours while IDV was seen in 80–85% of blazars when observed duration exceeded 6 hours. To understand the complex flux variation phenomenon, both quasi-continuous measurements over single night and longer term photometric monitoring are required. Multi-band variability studies help to reveal the true nature of blazars and provide valuable constraints in the emission models. From long term studies in the optical part of the EM spectra, HBLs are found to be less variable and polarized than LBLs (Jannuzi et al. (1994)). They also found the amplitudes of

¹Work presented in this chapter has been published in Gupta et al. (2016), MNRAS, (ODI: 10.1093/mnras/stw377 in press) (arXiv:1602.04200)

variability to be much smaller in case of HBLs than those for LBLs. Over the past decade, many new high energy, TeV blazars have been discovered, with a recent number reaching 54 (Holder (2012); Holder (2014)), among which 80% (44 out of 54) are found to be HBLs. These TeV HBLs are characterized by strong variability on diverse timescales ranging from a few months down to even a few minutes (e.g. Begelman et al. (2008); Nalewajko et al. (2011); Gaur et al. (2012); Barkov et al. (2012)). Variability studies help us to understand the particle acceleration mechanisms taking place in the relativistic jets and can shed light on the central regions of blazars, accretion processes and the structure of the jets. Rapid variability of TeV blazars at diverse timescales can be more easily observed by virtue of the high bulk Lorentz factors (often ≥ 25) of the knots seen in their relativistic jets.

The key motivation of this chapter is to study flux and colour variability characteristics along with spectral changes of three TeV blazars on diverse timescales to improve our current understanding of blazar variability through optical photometric studies. Here we report the optical photometric observations of the blazars PKS 1510-089, PG 1553+113 and Mrk 501 on diverse timescales using five telescopes, starting in June 2012 and running through September 2014.

5.2 Observations and Data Reductions

The optical photometric observations of our blazar sample were carried out in the B, V, R, and I pass-bands, with two telescopes in India, one in Greece, one in Bulgaria and one in Serbia, all equipped with CCD detectors. The details of these five telescopes, detectors and other parameters used are given in Table 2.5 Over 1495 image frames covering 95 nights between June 2012 and Sept 2014 were taken for three blazars, PKS 1510-089, PG 1553+113 and Mrk 501, to study their flux and spectral characteristics on diverse timescales. Observation logs, including date of observation, number of images acquired in each filter and the telescope used are presented for the three blazars individually in Tables 5.2, 5.3 and 5.4.

Table 5.1 Observation log of optical photometric observations of PKS 1510-089.

Date of Observation (yyyy mm dd)	Telescope	Data Points (B, V, R, I)
2014 04 30	D	0,2,2,2
2014 05 20	D	0,2,2,2
2014 05 21	D	0,2,2,2
2014 05 22	D	0,2,2,2
2014 05 23	D	0,2,2,2
2014 06 15	C	3,3,3,3
2014 07 01	D	0,2,2,2
2014 07 02	D	0,2,2,2
2014 07 03	D	0,2,2,2
2014 07 04	D	0,2,2,2
2014 07 05	D	0,2,2,2
2014 07 06	C	3,3,3,3
2014 07 21	C	3,3,3,3
2014 07 22	C	3,3,3,3
2014 07 25	C	3,3,3,3
2014 07 29	C	3,3,3,3
2014 08 03	D	0,2,2,2
2014 08 18	D	0,2,2,2

5.2.1 Telescopes and Data Reduction

The optical photometric observations of these blazars were carried out using five telescopes around the world among which two telescopes are in India operated by Aryabhata Research Institute of observational sciencES (ARIES), Nainital. One is the 1.04 m Sampuranand telescope having Ritchey-Chretien (RC) optics with a f/13 beam equipped with Johnson UBV and Cousins RI filters. The other is the 1.3-m Devasthal fast optical telescope (DFOT), which is a fast beam f/4 telescope with a modified RC system equipped with broad band Johnson-Cousins B, V, R, I filters. DFOT provides a pointing accuracy better than 10 arcsec RMS (Sagar et al. (2011)). Further details of both telescopes are given in Table 5.1 (telescopes A and B, respectively). We also employed the 1.3m RC telescope of Skinikas Observatory¹, of the University of Crete, Greece. Technical parameters and chip specifications for the cameras used are given in Table 5.1 (Telescope C). All frames were exposed through a set of standard Johnson-Cousins

¹Skinikas Observatory is a collaborative project of the University of Crete, the Foundation for Research and Technology – Hellas, and the Max-Planck-Institut für Extraterrestrische Physik.

Table 5.2 Observation log of optical photometric observations of PG 1553+113.

Date of Observation (yyyy mm dd)	Telescope	Data Points (B, V, R, I)
2013 07 03	E	1,1,1,1
2013 07 08	E	1,1,1,1
2013 07 26	C	3,3,3,3
2013 08 28	C	3,3,3,3
2014 04 09	B	0,1,1,1
2014 04 10	B	1,1,1,1
2014 04 11	B	0,1,5,1
2014 04 22	A	2,2,33,1
2014 04 23	A	1,1,46,1
2014 05 09	B	1,1,65,1
2014 05 11	B	0,16,149,2
2014 05 17	B	1,1,67,1
2014 05 23	A	1,1,172,1
2014 05 23	D	2,2,2,2
2014 05 26	B	1,1,55,1
2014 05 27	E	3,3,3,3
2014 06 15	C	3,3,3,3
2014 07 01	D	2,2,2,2
2014 07 02	D	2,2,2,2
2014 07 03	D	2,2,2,2
2014 07 04	D	2,2,2,2
2014 07 05	D	2,2,2,2
2014 07 06	C	3,3,3,3
2014 07 21	C	3,3,3,3
2014 07 22	C	3,3,3,3
2014 07 25	C	3,3,3,3
2014 07 29	C	3,3,3,3
2014 08 18	D	2,2,2,2
2014 08 26	D	2,2,2,2

filters. In addition to above telescopes, we carried out photometric observations of the blazars using the 60 cm Cassegrain telescope of Belogradchik AO, Bulgaria which was equipped with standard UBVRI filter sets. Instrumental details are summarized in Table 5.1 (Telescope D). Observations were also taken with 60cm Cassegrain telescope, which is located on Vidojevica mountain in South Serbia, through Johnson-Cousins BVRI standard filter set (Telescope E).

Table 5.3 Observation log of optical photometric observations of Mrk 501.

Date of Observation (yyyy mm dd)	Telescope	Data Points (B, V, R, I)
2012 06 02	C	3,3,3,3
2012 06 29	C	3,3,3,3
2012 06 30	C	3,3,3,3
2012 07 01	C	3,3,3,3
2012 07 02	C	3,3,3,3
2012 07 03	C	3,3,3,3
2012 07 04	C	3,3,3,3
2012 07 05	C	3,3,3,3
2013 07 08	E	1,1,1,1
2013 07 13	E	1,1,1,1
2013 07 14	E	1,1,1,1
2013 07 26	C	3,3,3,3
2013 08 28	C	3,3,3,3
2014 03 31	E	3,3,3,3
2014 05 22	D	0,2,2,2
2014 05 23	D	2,2,2,2
2014 05 27	E	2,3,2,3
2014 05 28	E	3,3,3,2
2014 05 28	E	5,4,5,4
2014 06 15	C	3,3,3,3
2014 06 29	E	3,3,3,3
2014 06 30	E	3,3,3,3
2014 07 01	E	3,3,3,2
2014 07 01	D	2,2,2,2
2014 07 02	D	2,2,2,2
2014 07 02	E	3,2,3,2
2014 07 03	D	2,2,2,2
2014 07 03	E	1,2,3,3
2014 07 04	D	2,2,2,2
2014 07 05	D	2,2,2,2
2014 07 05	E	2,3,3,3
2014 07 06	E	3,3,3,1
2014 07 06	C	3,3,3,3
2014 07 21	C	5,5,5,5
2014 07 22	C	5,5,5,5
2014 07 25	C	5,5,5,5
2014 07 28	C	5,5,5,5
2014 07 29	C	5,5,5,5
2014 08 02	D	2,2,2,2
2014 08 03	D	2,2,2,2
2014 08 04	D	2,2,2,2
2014 08 18	D	2,2,2,2
2014 08 19	D	2,2,2,2
2014 08 25	D	2,2,2,2
2014 08 26	D	2,2,2,2
2014 08 31	D	6,6,6,6
2014 09 18	D	2,2,2,2
2014 09 19	D	2,2,2,2

IRAF² package was used for the pre-processing of the raw data following the steps described below. Bias frames were taken for each night at regular intervals. Taking the median of all bias frames acquired during a particular night, a master bias was generated which was subtracted from all twilight flat frames and also from the image frames taken during that night. The next step was to generate a master flat for each filter by median combining all the flat frames in a particular passband. Then each source frame is divided by normalized master flat to remove pixel to pixel inhomogeneity. The final step of image pre-processing is to remove cosmic rays from all source image frames. Every science exposure was bias subtracted, dark subtracted and twilight flat fielded. Further processing was then done using the Dominion Astronomical Observatory Photometry (DAOPHOT II) software (Stetson (1987); Stetson (1992)) to perform concentric circular aperture photometry and some customized scripts written in MATLAB were also used. Aperture photometry for the data obtained from telescope E, was done with MaxIm DL packages. For every night aperture photometry was carried out with four different aperture radii, i.e., $\sim 1 \times \text{FWHM}$, $2 \times \text{FWHM}$, $3 \times \text{FWHM}$ and $4 \times \text{FWHM}$. Aperture radii of $2 \times \text{FWHM}$ were finally adopted for our final results as they provided the best signal to noise ratio S/N. For these blazars we observed three or more comparison stars from the same field as of the source³. We then selected two steady comparison stars based on their proximity in magnitude and colour to the blazar.

5.3 Variability detection criterion

To investigate the IDV properties of blazars we used two statistics, namely the F-test and χ^2 test which helped us to state the statistical significance of the extracted results.

²IRAF is distributed by the National Optical Astronomy Observatories, which are operated by the Association of Universities for Research in Astronomy, Inc., under cooperative agreement with the National Science Foundation.

³<http://www.lsw.uni-heidelberg.de/projects/extragalactic/charts/>

5.3.0.1 F-Test

The F-test is considered to be a proper statistic to determine any changes of variability. F values compare two sample variances and are calculated as (e.g. [Agarwal et al. \(2015\)](#)):

$$F_1 = \frac{\text{Var}(BL - StarA)}{\text{Var}(StarA - StarB)}, F_2 = \frac{\text{Var}(BL - StarB)}{\text{Var}(StarA - StarB)}.$$

Here (BL – Star A), (BL – Star B), and (Star A – Star B) are the differential instrumental magnitudes of blazar and comparison star A, blazar and comparison star B, and star A and star B, respectively, while $\text{Var}(BL - Star A)$, $\text{Var}(BL - Star B)$, and $\text{Var}(Star A - Star B)$ are the variances of those differential instrumental magnitudes.

We take the average of F_1 and F_2 to find a mean observational F value. The F value is then compared with $F_{\nu_{bl}, \nu_*}^{(\alpha)}$, a critical value, where ν_{bl} and ν_* respectively denote the number of degrees of freedom for the blazar and star, while α is the significance level set as 0.1 and 1 percent (i.e. 3σ and 2.6σ) for our analysis. If the mean F value is larger than the critical value, the null hypothesis (i.e., that of no variability) is discarded.

5.3.0.2 χ^2 -test

To examine the presence or absence of IDV we also performed χ^2 -test which is defined as (e.g. [Agarwal & Gupta \(2015\)](#)):

$$\chi^2 = \sum_{i=1}^N \frac{(V_i - \bar{V})^2}{\sigma_i^2}, \quad (5.1)$$

where, \bar{V} is the mean magnitude, and the i th observation yields a magnitude V_i with a corresponding standard error σ_i , which is due to photon noise from the source and sky, CCD read-out and other non-systematic error sources. Exact quantification of such errors by the IRAF reduction package is impractical and it has been found that theoretical errors are smaller than the real errors by a factor of 1.3–1.75 (e.g., [Gopal-Krishna et al. \(2003\)](#)) which for our data is ~ 1.5 , on average. So the errors obtained after data reduction should be multiplied by this factor to get better estimates of the

real photometric errors. This statistic is then compared with a critical value $\chi_{\alpha,\nu}^2$ where α is again the significance level as in case of the F-test while $\nu = N - 1$ is the number of degrees of freedom; $\chi^2 > \chi_{\alpha,\nu}^2$ implies the presence of variability.

5.3.0.3 Percentage amplitude variation

The percentage variation on a given night is calculated by using the variability amplitude parameter A , introduced by [Heidt & Wagner \(1996\)](#), and defined as

$$A = 100 \times \sqrt{(A_{max} - A_{min})^2 - 2\sigma^2}(\%). \quad (5.2)$$

Here, A_{max} and A_{min} are the maximum and minimum values in the calibrated LCs magnitude of the blazar, and σ is the average magnitude measurement error.

5.4 Results

5.4.1 PKS 1510–089

PKS 1510–089 ($\alpha_{2000.0} = 15\text{h } 12\text{m } 50.53\text{s}$, $\delta_{2000.0} = -09^\circ 05' 59''$) is a FSRQ at a redshift of $z = 0.361$ ([Thompson et al. \(1990\)](#)) and is among the highly polarized AGN. [Lu \(1972\)](#) first reported significant optical flux variations over a time span of ~ 5 yr. During a 1948 outburst, PKS 1510–089 showed an extremely large variation of $\Delta B = 5.4$ mag and later faded by ~ 2.2 mag within 9 days ([Liller & Liller \(1975\)](#)). On IDV timescales some very strong variations have been reported in optical bands: ΔR of 0.65 mag in 13 min ([Xie et al. \(2001\)](#)) and of 2.0 mag in 42 min ([Dai et al. \(2001\)](#)), while in V band a change of 1.68 mag in 60 min has been reported ([Xie et al. \(2002\)](#)). It was detected by the EGRET instrument on-board the CGRO in the MeV–GeV energy band ([Hartman et al. \(1992\)](#)) as γ -rays. The synchrotron emission peaks around IR frequencies and IC component seems to dominate the γ -rays. A pronounced UV bump is clearly visible in this source which can be attributed to the thermal emission from the accretion disk around the central region ([Malkan & Moore \(1986\)](#); [Pian & Treves \(1993\)](#)). A rapid γ -ray flare

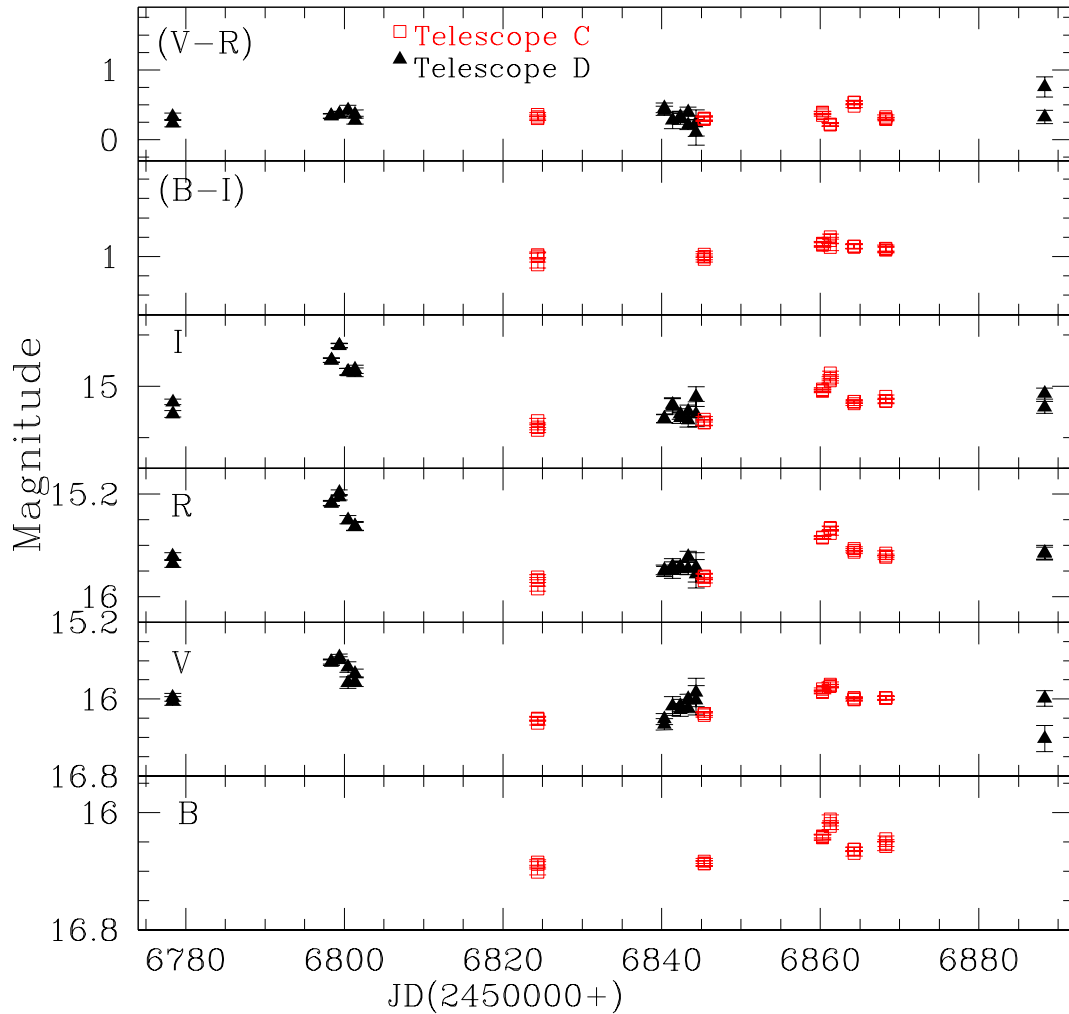


Figure 5.1 Short-term through long-term variability LCs and colour indices of PKS 1510–089 in the B, V, R and I bands and (B-I) and (V-R) colours. Different symbols denote data from different observatories: open red squares, telescope C; filled black triangles, telescope D.

was reported by [D’Ammando et al. \(2009\)](#) in 2008 March using the AGILE satellite, while it was monitored by the Whole Earth Blazar Telescope (WEBT). Later, during the high γ -ray state of this source in 2009 March, [D’Ammando et al. \(2011\)](#) reported detailed analysis of their multifrequency monitoring of this FSRQ using AGILE. They also found noticeable spectral variations in the near-IR through optical bands and also found thermal features in the optical/UV spectrum in the broad-band SED of this source.

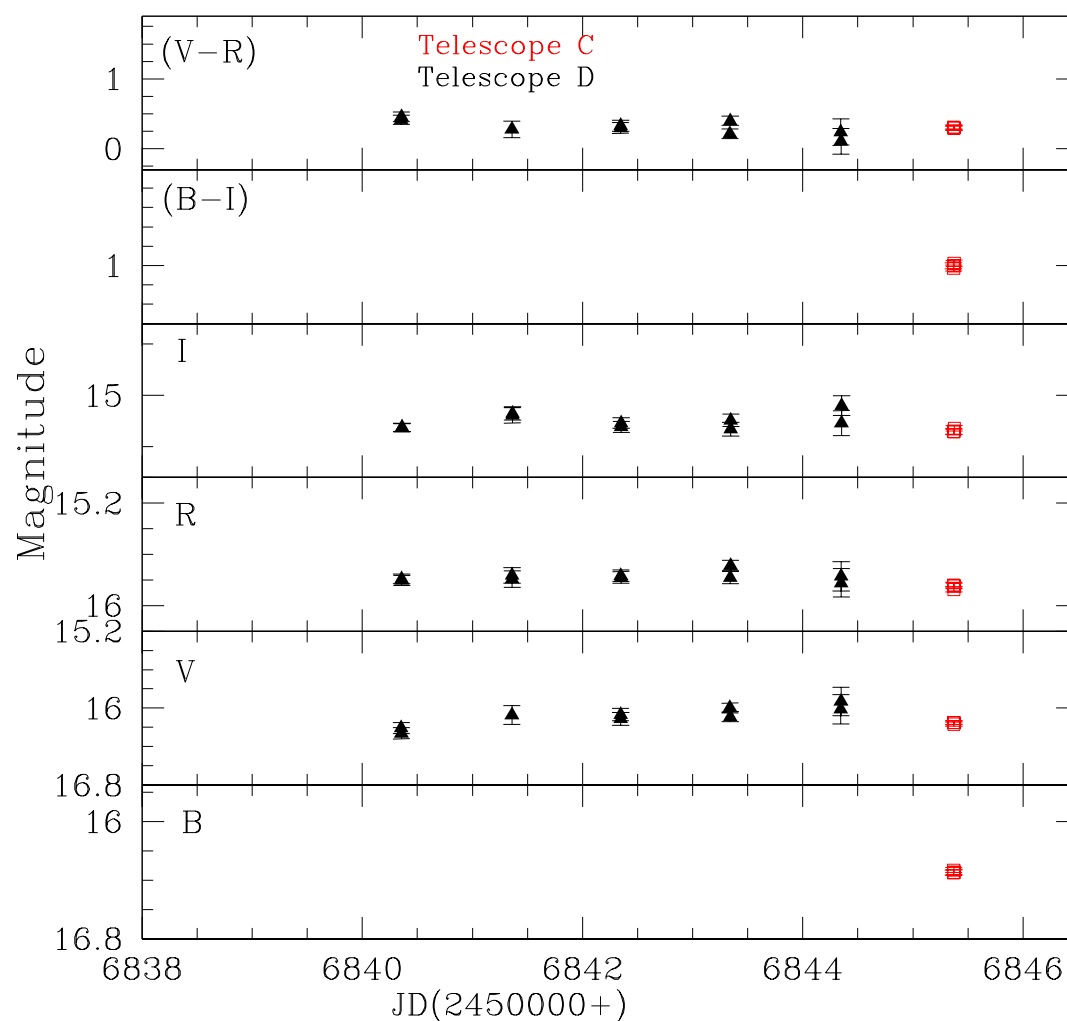


Figure 5.2 As in Figure 5.1, for the limited period around MJD 6840, providing a better view of variability in that period.

5.4.1.1 Flux and colour variability

The ~ 4 months LCs for the blazar PKS 1510-089 in B, V, R, and I passbands are shown in Figure 5.1 along with the colour indices (B-I) and (V-R). Genuine STV was present, but this source exhibited no significant colour variation during the observation span. To provide a better view of the nature of the variability of this source around MJD 6840–6846, we have plotted this same time span on an expanded scale in Figure 5.2.

In the following analysis, we have corrected the calibrated magnitudes for galactic extinction following the extinction map of [Schlegel et al. \(1998\)](#) using the NED extinction calculator⁴ with values in each filter as: $A_B = 0.363$ mag, $A_V = 0.275$ mag, $A_R = 0.217$ mag and $A_I = 0.151$ mag ([Cardelli et al. \(1989\)](#); [Bessell et al. \(1998\)](#)). The bottom panel of Figure 5.1 represents short-term/long-term variability (STV/LTV) LC of PKS 1510–089 in the B passband which includes data from 6 nights using the 1.3m RC telescope in Greece. We monitored the source in the B filter for STV/LTV studies from JD 2456824.37 to JD 2456868.27. The maximum B band magnitude attained by the source was 16.77 on JD 2456824.37 while the brightest level of B = 16.41 magnitude was reached on JD 2456861.27, which is ~ 1.39 magnitude brighter than the faintest level of B = 17.8 as reported by [Liller & Liller \(1975\)](#), thus indicating that the source is not in a low state and could possibly be in a post-outburst state. The corresponding STV/LTV LCs in V, R, and I passbands are displayed in the second, third and fourth panels (from the bottom) of Figure 5.1 using data sets from the 1.3m RC telescope in Greece and the 60 cm Cassegrain telescope in Bulgaria (telescope C & D) covering a time span between JD 2456778.37 to JD 2456888.28. The details of magnitude changes during the whole observation period are listed in Table 5.6 where column 1 is the source name, column 2 is the filter used for observation, Column 3 tells the faintest magnitude attained by the target and its corresponding JD is given in column 4, while the brightest value is given in column 5, the time corresponding to it is given in column 6 and the last column gives the total magnitude range. During the entire monitoring period, the overall magnitude variations were $\Delta B = 0.36$ mag, $\Delta V = 0.85$ mag, $\Delta R = 0.75$ mag, and $\Delta I = 0.83$ mag. The (B-I) and (V-R) colour variations as a function of JD are shown in the top two panels of Figure 5.1. The maximum variation in (B-I) during our observation span was found to be a modest 0.29 mag, between 1.13 mag on JD 245684.38 and 1.42 mag on JD 2456861.27 while that in (V-R) was 0.64 mag, between 0.17 mag on JD 2456844.35 and 0.81 mag on JD 2456888.28. The mean magnitudes in B, V, R, and I are 16.60, 16.25, 15.86, and 15.26 mag, respectively, while the average colour indices are (B-I) = 1.29 mag and (V-R) = 0.40 mag.

⁴<http://ned.ipac.caltech.edu>

5.4.2 PG 1553+113

PG 1553+113 ($\alpha_{2000.0} = 15\text{h } 55\text{m } 43.04\text{s}$, $\delta_{2000.0} = +11^\circ 11' 24.4''$) was discovered in the Palomar-Green (PG) survey of ultraviolet-excess objects as a 15.5 magnitude blue stellar object (Green et al. (1986)). It is a bright optical source with R band magnitude varying from ~ 13 to ~ 15.5 (Miller et al. (1988)) while it has a mean V-band magnitude around 14 (Falomo & Treves (1990); Osterman et al. (2006)). Due to its featureless spectra, the object was suggested to be a BL Lacertae object (Miller & Green (1983)) and its redshift determination has always been a challenge. Based on low resolution UV spectra, Miller & Green (1983) estimated its redshift ~ 0.37 . Based on the detection of strong Ly α + O VI absorbers, Danforth et al. (2010) proposed $z > 0.395$ while $z \leq 0.58$ from statistical arguments. Recently, Kapanadze (2013) found that the upper limit to its redshift should be smaller than that proposed by Danforth et al. (2010). Its classification as a HSP was determined from its SED (Falomo & Treves (1990); Donato et al. (2005)). Falomo et al. (1994) found its optical spectral index to be constant ($\alpha \sim -1$) using observations between 1986 and 1991 while it underwent a variation of $\Delta V = 1.4$. PG 1553+113 has been observed through entire EM spectra from radio through very high energy γ -rays up to 1 TeV (Aharonian et al. (2006); Albert et al. (2007a)). Its $\log(F_{2\text{KeV}}/F_{5\text{GHz}})$ values range from 4.99 to 3.88, where $F_{2\text{KeV}}$ is its 2 keV X-ray flux, while $F_{5\text{GHz}}$ is the radio flux at 5 GHz (Osterman et al. (2006); Rector et al. (2003)).

5.4.2.1 Flux and colour variability

We monitored PG 1553+113 in the R passband on 7 nights for a span of ~ 4 hours on each night to investigate flux variability properties on intra-day timescales. The IDV plots are displayed in Figure 5.3 where observation date and telescope used are mentioned within the plot itself. The observation log is given in Table 5.3. To claim the presence or absence of intra-day variability, we applied the F- and χ^2 - statistical tests, the results of which are presented in Table 5.5. The blazar is said to be variable (V) if the variability conditions for both tests are satisfied for the 0.999 level, while it is marked probably variable (PV) if conditions for either of the two tests are followed at

the 0.99 level; while the it is marked non-variable (NV) if none of these conditions are met. We detected strong IDV on 1 night while it was found to be PV on 5 nights and was clearly NV on only a single night.

The 1.2 year LCs in B, V, R, and I along with (B–I) and (V–R) colour variations for the blazar PKS 1553+113 are shown in Figure 5.4. To study optical properties on short/long timescales, we investigated the target in B, V, R, and I filters observed using all 5 telescopes on 29 nights during the period between JD 2456477.5 and JD 2456896.5. We have corrected the calibrated magnitudes for galactic extinction in each filter with $A_B = 0.188$ mag, $A_V = 0.142$ mag, $A_R = 0.113$ mag and $A_I = 0.078$ mag. The details of the magnitude changes during the whole observation span for each band are listed in Table 5.6. Significant STV was found with moderate colour variations. The minimum R band magnitude attained by our target was of $R = 13.81$ on $JD = 2456759.7$ which is only 0.31 mag fainter than the brightest magnitude of $R = 13.5$ mag as observed earlier by [Osterman et al. \(2006\)](#), when the source was in a flaring state. So it is fair to say that we have also observed this blazar in its flaring state. During our observation time span, the overall magnitude variations were $\Delta B = 0.66$, $\Delta V = 0.54$, $\Delta R = 0.59$, and $\Delta I = 0.41$.

The values of the (B–I) and (V–R) colour indices as a function of JD are shown in top two panels of Figure 5.4. Plots indicate moderate colour variation. The maximum variation noticed in the source for (V–R) during the entire LC was found to be 0.35, between 0.20 mag on JD 2456840.37 and 0.55 mag on JD 2456759.70, while that in (B–I) was 1.39 between its colour range of 0.06 mag on JD 2456824.4 and 1.45 mag on JD 2456533.26. Mean magnitudes in B, V, R, and I are 14.82, 14.43, 14.07, and 13.63, while the average colour indices are (B–I) = 1.20 mag and (V–R) = 0.34 mag.

5.4.3 Mrk 501

Mrk 501 ($\alpha_{2000.0} = 16\text{h } 53\text{m } 52.13\text{s}$, $\delta_{2000.0} = +39^\circ 45' 36.2''$) is the second closest BL Lacertae object after Mrk 421, with $z = 0.034$, and is thus an object of interest across the whole EM spectrum ([Fan & Lin \(1999\)](#); [Kataoka et al. \(1999\)](#); [Sambruna et al.](#)

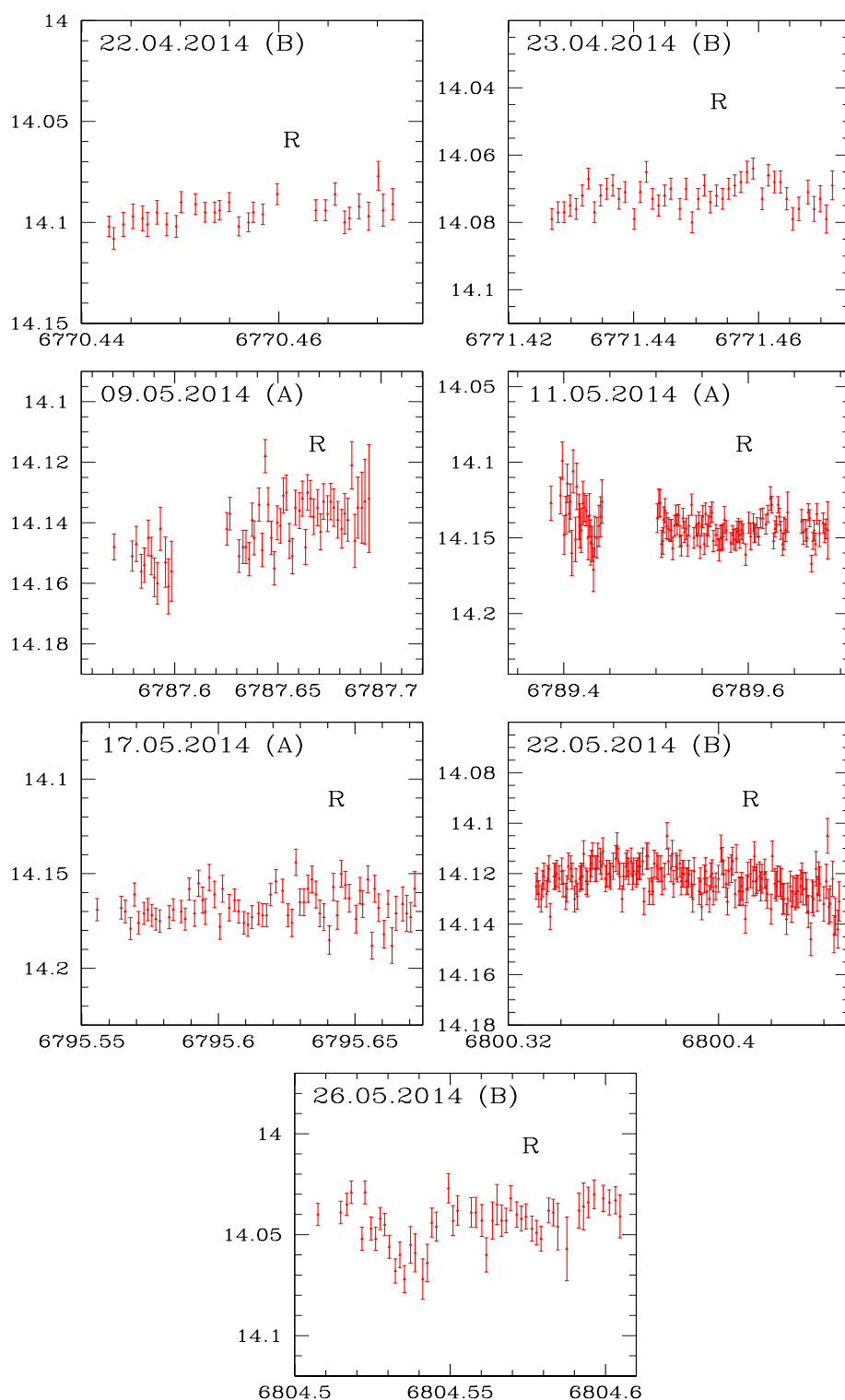


Figure 5.3 Light curves for PG 1553+113. In each panel, the axes are the JD (24590000+) and R-band magnitude; the observation date and the telescope used are indicated.

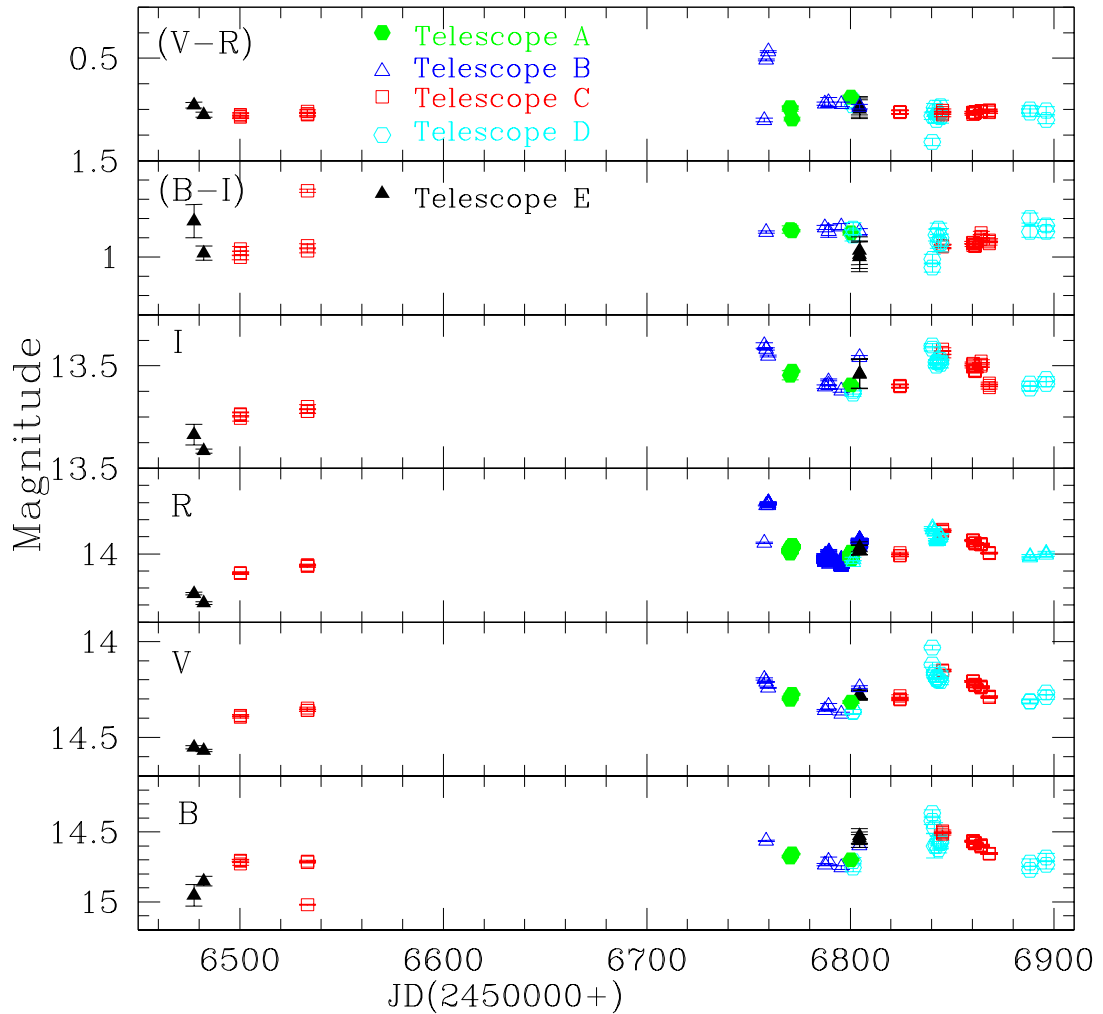


Figure 5.4 Long-term variability LCs and colour indices of PG 1553+113 in the B, V, R and I bands and (B-I) and (V-R) colours. Different symbols denote data from different observatories: filled green circles, telescope A; blue open triangles, telescope B; red open squares, telescope C; cyan open squares, telescope D; black closed triangles, telescope E.

(2000); Xue & Cui (2005); Gliozzi et al. (2006)). The near-IR–optical spectrum of this HBL shows a strong host galaxy signature with host brightness of $\simeq 11.92$ in R band (Nilsson et al. (2007)). The SED of Mrk 501 displays a double-humped structure with peaks occurring at keV and GeV/TeV energies. The physical mechanisms responsible for the production of GeV/TeV hump are still a topic of debate (Ghisellini & Madau (1996); Krawczynski et al. (2004); Cerruti et al. (2012)).

Table 5.4 Results of IDV observations of PG 1553+113.

Date	Band	N	F-test	χ^2 test	Variable	A%
			$F_1, F_2, F, F_c(0.99), F_c(0.999)$	$\chi_1^2, \chi_2^2, \chi_{av}^2, \chi_{0.99}^2, \chi_{0.999}^2$		
22.04.2014	R	30	2.08, 1.49, 1.79, 1.20, 1.27	38.55, 26.45, 32.5, 746.39, 776.91	PV	3.0
23.04.2014	R	45	2.17, 2.63, 2.40, 1.28, 1.39	68.22, 77.19, 72.70, 413.39, 436.37	PV	1.0
09.05.2014	R	56	3.27, 3.23, 3.25, 1.89, 2.34	125.16, 103.19, 114.17, 82.29, 93.17	V	4.2
11.05.2014	R	123	1.41, 1.56, 1.49, 1.53, 1.76	98.46, 110.04, 104.25, 161.25, 176.01	NV	–
17.05.2014	R	67	1.32, 1.30, 1.31, 1.27, 1.38	48.44, 45.80, 47.12, 37.29, 460.90	PV	4.3
22.05.2014	R	170	1.08, 1.00, 1.02, 1.73, 2.08	115.87, 101.75, 108.81, 104.01, 116.09	PV	4.0
26.05.2014	R	50	2.06, 2.18, 2.12, 1.96, 2.46	75.99, 70.10, 73.04, 74.92, 85.35	PV	4.4

Var : Variable, PV : probable variable, NV : Non-Variable

In the optical regime, [Heidt & Wagner \(1996\)](#) reported a flux variation of $\sim 32\%$ in a time span of less than 2 weeks while [Ghosh et al. \(2000\)](#) reported variability in 7 out of 10 nights during March & June 1997. Mrk 501 has been found to display rapid variability on few minutes timescales over the entire EM spectra ([Albert et al. \(2007b\)](#); [Gupta et al. \(2008\)](#)), which can be attributed to relativistically beamed radiation from jets, jet deceleration ([Georganopoulos & Kazanas \(2003\)](#); [Levinson \(2007\)](#)), or other plasma mechanisms (e.g. [Krishan & Wiita \(1994\)](#))

5.4.4 Mrk 501

Mrk 501 ($\alpha_{2000.0} = 16\text{h } 53\text{m } 52.13\text{s}$, $\delta_{2000.0} = +39^\circ 45' 36.2''$) is the second closest BL Lacertae object after Mrk 421, with $z = 0.034$, and is thus an object of interest across the whole EM spectrum ([Fan & Lin \(1999\)](#); [Kataoka et al. \(1999\)](#); [Sambruna et al. \(2000\)](#); [Xue & Cui \(2005\)](#); [Gliozzi et al. \(2006\)](#)). The near-IR–optical spectrum of this HBL shows a strong host galaxy signature with host brightness of $\simeq 11.92$ in R band ([Nilsson et al. \(2007\)](#)). The SED of Mrk 501 displays a double-humped structure with peaks occurring at keV and GeV/TeV energies. The physical mechanisms responsible for the production of GeV/TeV hump are still a topic of debate ([Ghisellini & Madau \(1996\)](#); [Krawczynski et al. \(2004\)](#); [Cerruti et al. \(2012\)](#)). In the optical regime, [Heidt & Wagner \(1996\)](#) reported a flux variation of $\sim 32\%$ in a time span of less than 2 weeks while [Ghosh et al. \(2000\)](#) reported variability in 7 out of 10 nights during March & June 1997. Mrk 501 has been found to display rapid variability on few minutes timescales over the entire EM spectra ([Albert et al. \(2007b\)](#); [Gupta et al. \(2008\)](#)), which can be attributed to relativistically beamed radiation from jets, jet deceleration ([Georganopoulos & Kazanas \(2003\)](#); [Levinson \(2007\)](#)), or other plasma mechanisms (e.g. [Krishan & Wiita \(1994\)](#))

5.4.4.1 Flux and colour variability

The photometric magnitudes extracted during our monitoring campaign are displayed in Figure 5.5 which shows ~ 2.3 year LC for the blazar Mrk 501. The LCs in B, V, R, and I passbands along with (B-I) and (V-R) colour variations are plotted in different

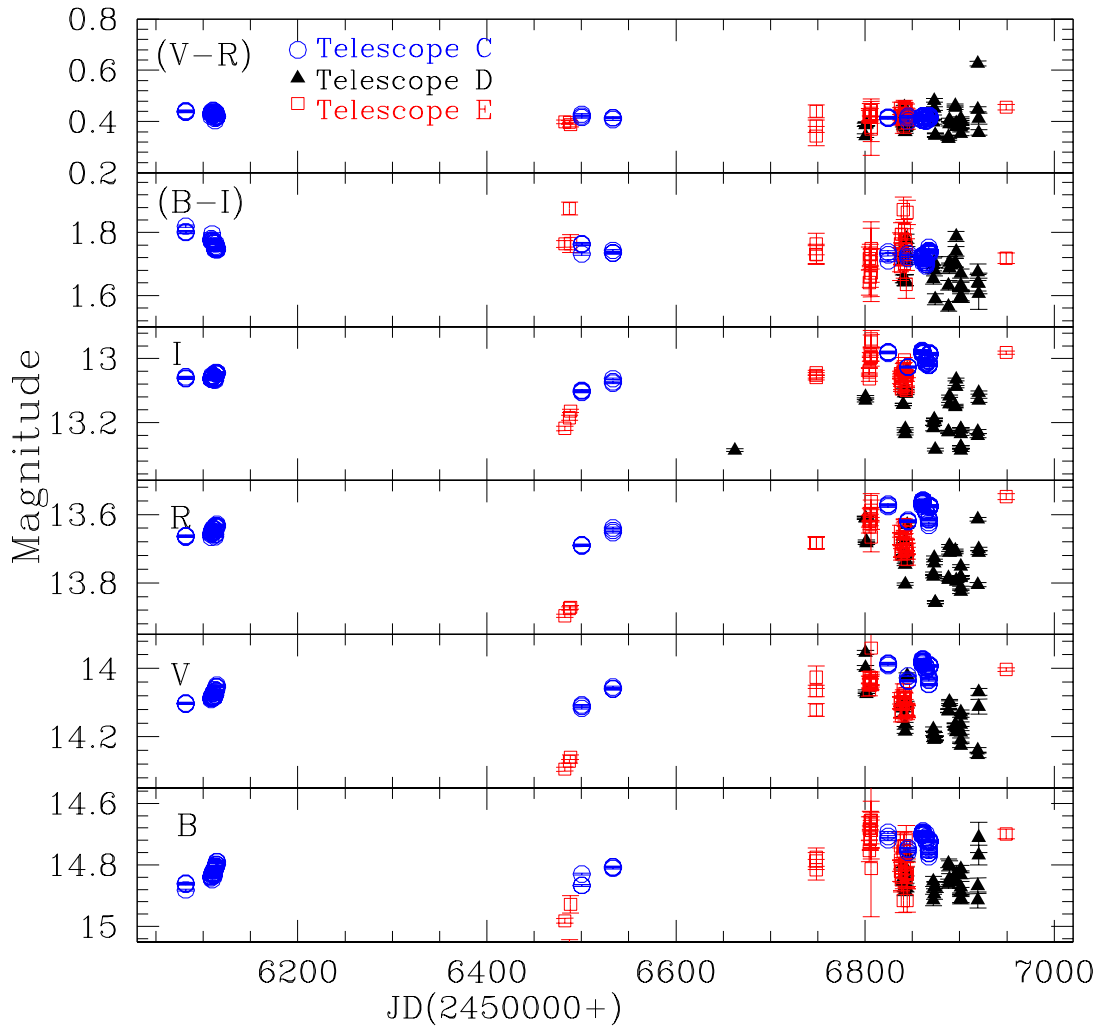


Figure 5.5 Long-term variability LCs and colour indices of Mrk 501 in the B, V, R and I bands and (B-I) and (V-R) colours. Different symbols denote data from different observatories: blue open circles, telescope C; black filled triangles, telescope D; and red open squares, telescope E.

panels of the figure. Figure 5.6 shows the nature of variability in more detail around MJD 6800-7000, when this blazar displays large variability.

The target was observed for 48 nights between 2456081.5 and 2456920.4 using five telescopes whose details are given in Table 5.1. Details about magnitude changes in each band during the whole monitoring period are given in Table 5.6. In the following analysis, we have corrected the calibrated magnitudes for galactic extinction as: $A_B = 0.069$ mag, $A_V = 0.052$ mag, $A_R = 0.041$ mag and $A_I = 0.029$ mag. The flux from the nucleus of the HBL is contaminated by the emissions of its host galaxy. So the observed

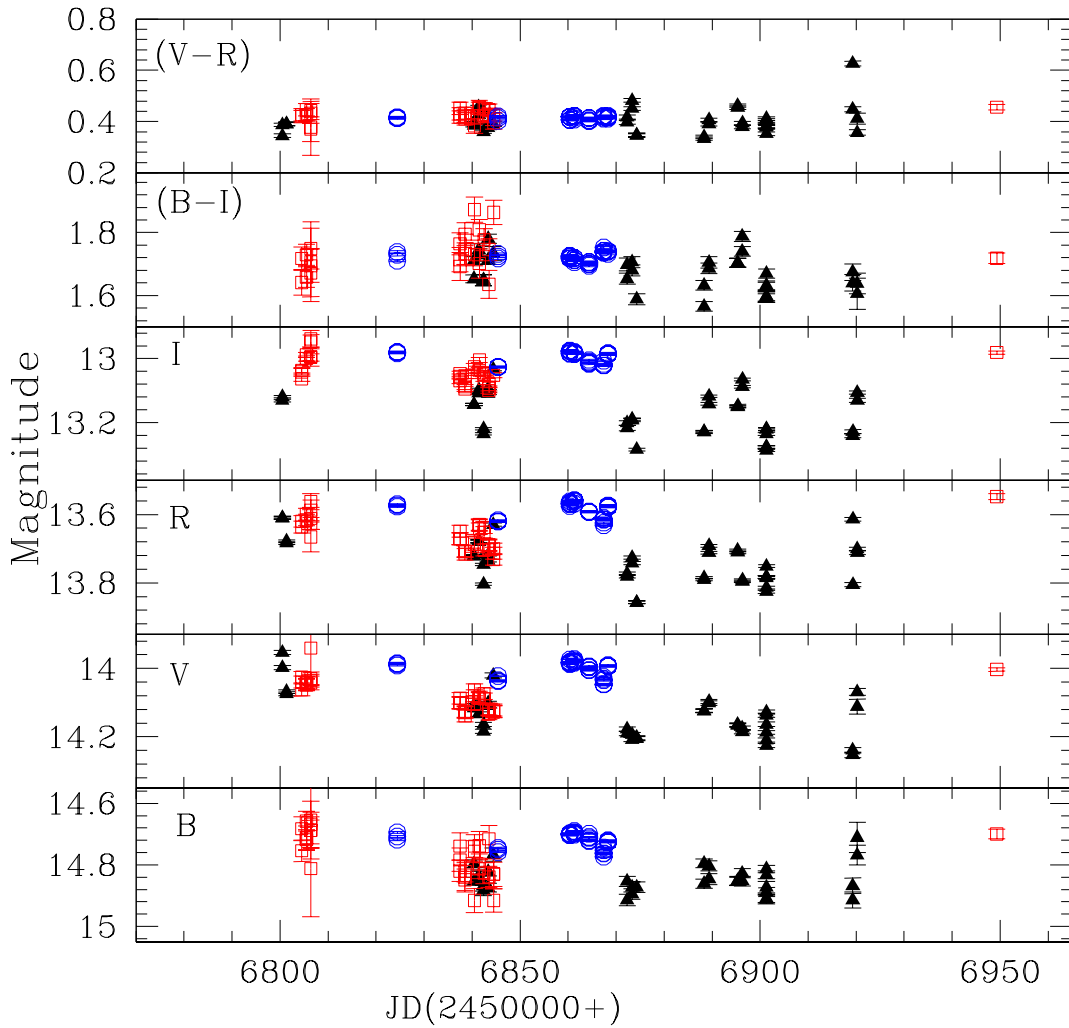


Figure 5.6 Data from Figure 5 expanded around MJD 6800-7000 to better show variability in that period. Symbols as in Fig. 5.

magnitudes in each spectral band have also been corrected for the host galaxy contribution, following the measurements of Nilsson et al. (2007) to calculate the host galaxy contribution in R band which is then used to find the corresponding contributions for the B, V, and I bands (Fukugita et al. (1995)).

During our observation time span, the overall magnitude variations were $\Delta B = 0.41$, $\Delta V = 0.35$, $\Delta R = 0.35$, and $\Delta I = 0.71$. The mean magnitudes in B, V, R, and I are 14.80, 14.09, 13.68, and 13.07, respectively. The short-term and long-term LCs of Mrk 501 in (V-R) and (B-I) colours are shown in the top two panels of Figure 5.5. The average colour indices are $(B-I) = 1.72$ and $(V-R) = 0.41$. The maximum variation noticed in

Table 5.5 Results of STV/LTV studies for magnitude changes in each band.

Source	Band	Faintest Mag	JD (Min)	Brightest Mag	JD (Max)	Δm
PKS 1510–089	B	16.77	2456824.4	16.41	2456861.3	0.36
	V	16.69	2456888.3	15.84	2456799.4	0.85
	R	16.16	2456824.4	15.41	2456799.4	0.75
	I	15.58	2456824.4	14.75	2456799.4	0.83
PG 1553+113	B	15.21	2456533.3	14.55	2456840.4	0.66
	V	14.71	2456482.3	14.17	2456840.4	0.54
	R	14.40	2456482.3	13.81	2456759.7	0.59
	I	13.91	2456482.3	13.50	2456757.7	0.41
Mrk 501	B	15.06	2456487.4	14.65	2456806.4	0.41
	V	14.29	2456482.4	13.94	2456806.4	0.35
	R	13.90	2456482.4	13.55	2456949.3	0.35
	I	13.29	2456901.3	12.58	2456801.4	0.71

the source for the (V-R) colour index during the entire LC was found to be 0.29 (the range was between 0.33 mag on JD 2456888.33 and 0.63 mag on JD 2456919.31), while that in (B-I) was 0.31 (this colour index ranged between 1.56 mag on JD 2456888.33 and 1.88 mag on JD 2456487.40).

5.4.5 Correlated variations between colour and magnitude?

As variations in the optical flux of blazars are accompanied with spectral changes, studying the colour index–magnitude relationship can be an useful tool to understand the origin of variability in blazars. In this section, we investigate the colour–magnitude relationship for all three blazars. Since spectral variations follow any optical flux variations, examining relationships between the corresponding variations in the colour indices such as (B–V), (V–R), (R–I), (B–R) or (B–I) of the three targets with respect to the variation in their brightnesses would be very helpful in understanding the variability characteristics in more detail.

Colour–magnitude (CM) plots on few months timescales for the three sources are shown in Figure 5.7. We have fitted straight lines ($CI = mV + c$) to colour index, CI against V magnitude plots for each source. The fitted values for the slope, m , and intercept c , are listed in Tables 7, 8 and 9 for PKS 1510-089, PG 1553+113 and Mrk 501, respectively,

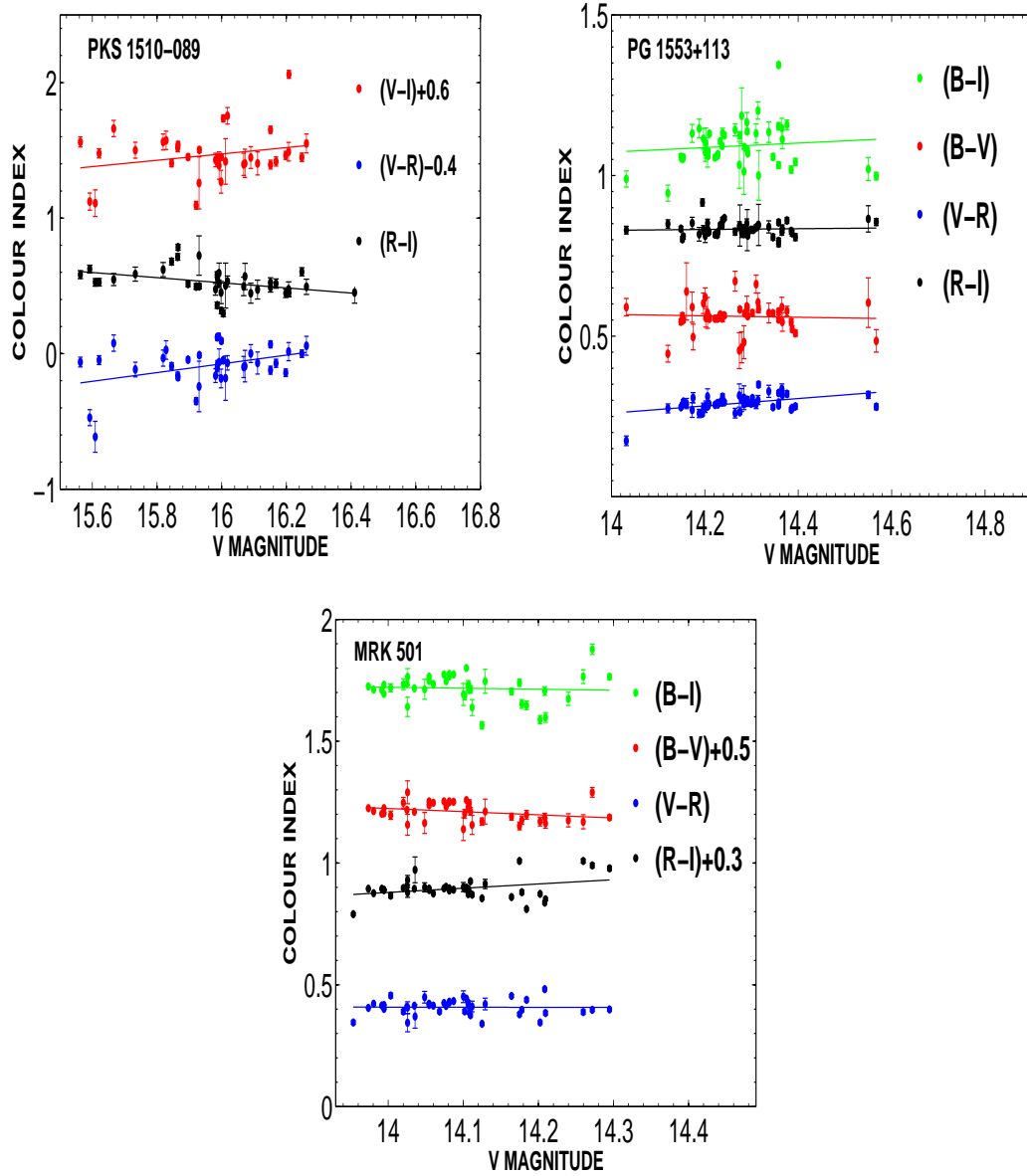


Figure 5.7 Colour magnitude plots on short timescales for all three blazars. The V magnitudes are given on the X-axis and the various labelled colour indices are plotted against them for each labelled source.

Table 5.6 Color–magnitude dependencies and colour–magnitude correlation coefficients on short timescales for PKS 1510-089.

Color Indices	m_1^a	c_1^a	r_1^a	p_1^a
(V-I)	0.234	-2.571	0.250	0.130
(V-R)	0.322	-5.227	0.397	0.015
(R-I)	-0.189	3.554	-0.374	0.021

^a m_1 = slope and c_1 = intercept of CI against V;
 r_1 = Pearson coefficient; p_1 = null hypothesis probability

Table 5.7 Color–magnitude dependencies and colour-magnitude correlation coefficients on short timescales for PG 1553+113.

Color Indices	m_1^a	c_1^a	r_1^a	p_1^a
(B-I)	0.070	0.093	0.102	0.498
(B-V)	-0.022	0.876	-0.048	0.744
(V-R)	0.114	-1.336	0.440	0.0009
(R-I)	0.012	0.660	0.054	0.704

^a m_1 = slope and c_1 = intercept of CI against V;
 r_1 = Pearson coefficient; p_1 = null hypothesis probability

Table 5.8 Color–magnitude dependencies and colour-magnitude correlation coefficients on short timescales for Mrk 501.

Color Indices	m_1^a	c_1^a	r_1^a	p_1^a
(B-I)	-0.040	2.282	-0.057	0.722
(B-V)	-0.130	3.042	-0.287	0.069
(V-R)	-0.003	0.454	-0.009	0.956
(R-I)	0.174	-1.559	0.329	0.033

^a m_1 = slope and c_1 = intercept of CI against V;
 r_1 = Pearson coefficient; p_1 = null hypothesis probability

along with the linear Pearson correlation coefficients, r_1 and the corresponding null hypothesis probabilities, p_1 . A positive slope here means positive correlation between the CI and the brightness of the source. Here we consider the result significant only if the null hypothesis probability is $p_1 \leq 0.01$ and Pearson correlation coefficient, $r \geq 0.5$. A significant positive correlation in these plots would physically imply that the source follows a bluer-when-brighter (BWB), or redder when brighter (RWB) trend, i.e., the source tends to be bluer when its brightness increases, while a negative slope would indicate an opposite correlation between the source magnitude and CI, indicating that the source exhibits redder when its brightness increases.

The correlation analysis results between brightness of the source and the colour indices are also given in Tables 7–9. For these sources we did not find any strong correlation (Pearson correlation coefficient, $r > 0.5$) between V band magnitude and colour indices on several months timescale.

The CM relationship at diverse timescales can help us understand the emission mechanisms responsible for blazar variability and also help to pin down the emitting regions.

Different CM relationship in BL Lacs and FSRQs could be due to the existence of two varying modes, i.e., larger flux variations with lesser spectral changes or vice versa. [Raiteri et al. \(2003\)](#) found at most weak correlations between the source magnitude and the colour indices for the BL Lac object S5 0716+714, that are similar to our results. [Agarwal et al. \(2016\)](#) also found no evidence for the source to display spectral changes with magnitude on either of the timescales even when the BL Lac S5 0716+714 was rapidly variable. The CM relation in blazars has been found to vary among their outburst state, active state, and the faint state ([Sasada et al. \(2010\)](#)). Optical emission from blazars is generally a combination of jet and accretion disk radiation and usually dominated by that from the relativistic jets. However, FSRQs are usually low frequency synchrotron peaked sources, thus having a substantial contribution to the blue-UV continuum arising from thermal contamination from the accretion disk which is expected to produce a slowly and weakly variable bluer emission component. The position of the thermal blue bump and its strength in comparison to the jet emission also affect the spectral behaviour of FSRQs. When relativistically beamed jet synchrotron emission dominates the accretion disk emission, the BWB trend can be explained by acceleration of relativistic particles or due to injection of fresh electrons having even harder energy distribution. [Sun et al. \(2014\)](#) recently proposed a timescale dependent colour variation model, according to which a BWB trend in blazars is strongest for timescales of < 30 days and it eventually weakens with as timescale increases to above 100 days. Our results seem to complement this model. Densely sampled and simultaneous multiband photometric observations will be helpful in understanding the CM relationship in greater detail and in better constraining models.

5.5 Discussion and Conclusion

Blazar variability studies can help us examine the radiation mechanisms in more detail while also provide an insight on the location, size, structure, and dynamics of the emitting regions ([Ciprini et al. \(2003\)](#)). Most mechanisms for variability in RLAGNs are expected to arise within the relativistic jet whose emission is Doppler boosted. The

only significant extrinsic variability in blazars is probably seen in the radio band, where strongly frequency dependent interstellar scintillation is found to be dominant mechanism of variability at low radio frequencies. Intrinsic processes operate across all EM bands, and include directly those causing changes in the jet radio emission. Some of these clearly arise from synchrotron and Compton losses which cause electron energy losses but energy gains can come from the fresh injection of particles with energy distribution higher than that of the previous ones. Both of these processes can co-exist but operate on different timescales.

The initial origin of variability could be located in accretion disk based fluctuations propagating into the jets, or it could start with changes in the outgoing flow, usually related to shocks in the blazar jets. According to the dominant shock-in-jet model, synchrotron and inverse Compton (IC) processes are the most common basic processes (Hughes et al. (2011)). When those intense emitting regions are found in the highly relativistic Doppler boosted jets pointed at very small angles with respect to the line of sight, variations are significantly amplified and frequency shifted owing to relativistic beaming. Changes in the jet geometry due to changing jet direction can cause variations in the bulk Doppler factor of the relativistic blobs traveling along the jet (usually in range 10-30), which in turn can lead to blazar variability at relatively long time-scales (Hovatta et al. (2009); Rani et al. (2011)). The key processes responsible for blazar variability probably are due to a jet not being a stationary object which gives rise to various instabilities, turbulence (e.g. Marscher (2014); Calafut & Wiita (2015)) and developing or decaying shocks. These act on a range of timescales. If δ is the the Doppler factor, since $F_\nu \propto \delta^3$, an increase in δ causes an increase in flux (Villata & Raiteri (1999)) and also in the observed frequency ($\nu \propto \delta$). During their low states, blazar variability can be attributed to accretion disk instabilities since thermal emission from the central region of blazars can dominate over jet emission then. Then the variability can be explained by orbits of hot spots on the accretion disk, including eclipsing of the hot spot by parts of the disk between the individual spot and the observer; this aspect directly depends on the geometry of the accretion disk and also on the viewing angle of the observer. Even though optical band is a narrow part of the complete EM spectrum, it is critical

in determining the presence of additional components other than synchrotron continuum, such as accretion disk emission or host galaxy contribution.

The presence of both BWB and RWB trends in some blazars can be explained by superposition of both blue and red emission components where the redder one is attributed to the synchrotron radiation from the relativistic jet while the blue component could come from the thermal emission from the accretion disk. The BWB trend may indicate that two components, one variable (with a flatter slope, α_{var}) ($f_\nu \propto \nu^{-\alpha}$) and another stable (with $\alpha_{const} > \alpha_{var}$), contribute to the overall emission in the optical regime. It also could be possibly explained with a one component synchrotron model if the more intense the energy release, the higher the particles frequency (Fiorucci et al. (2004)). Then the BWB trend could be explained if the luminosity increase was due to injection of fresh electrons with an energy distribution harder than that of the previously cooled ones (Kirk et al. (1998); Mastichiadis & Kirk (2002)). The BWB trend could also be due to Doppler factor variations in a spectrum slightly deviating from a power law (Villata et al. (2004)). If optical emission is combination of emission from both jet and accretion disk, then as the jet brightens from a low state, the colour of the combined emission gets redder as synchrotron emission from the relativistic jets is intrinsically redder than that of the accretion disk, producing RWB behaviour. However, if even higher energy electrons are injected causing further brightening, then we get a bluer colour (BWB); this is usually dominant during an outburst state. We found a weak BWB trend, i.e., a spectrum becoming flatter when the object is brighter, in two of the sources while the opposite was found dominant in one of them.

In this chapter, we have performed multiband optical photometry for three TeV blazars namely: PKS 1510–089, PG 1553+113 and Mrk 501 between 2012 and 2014 in a total of 95 nights in B, V, R, and I passbands. This allowed us to study flux and colour variability characteristics on diverse timescales. During our 7 nights of observation for IDV for PG 1553+113 we detected clear IDV on a single night using F-statistics and χ^2 -test (at 3σ significance for both). But if we include PV cases (at 2.6σ for either tests) then we can say we found the source to be variable on intraday timescales on 6 out of these 7 nights. Carini (1990) monitored about 20 blazars and found IDV in most of them.

He also noticed that probability of detecting IDV increased to 80% when observed for more than 8 hours. Later, a sample of 34 BL Lacertae objects were observed by [Heidt & Wagner \(1996\)](#) when they found that about 75% of the sample displayed significant variations when observed for < 6 hours. [Carini et al. \(2007\)](#) found that less than 10% of his blazar sample displayed variability on intraday timescales when observed for only ~ 4 -5 hours. Thus, the chances of observing IDV in blazars is greatly improved when observed for more than 6 hours. The results in this study are consistent with these earlier observations. Clearly, IDV results can be further improved by more dense and lengthier observations.

We searched for flux and colour variability on few months to few years timescales and found significant flux variations on these timescales with moderate colour variations for all three TeV blazars. We also studied the correlation between the V magnitude of the source and corresponding variations in the (B-I), (B-V), (R-I), and (V-R) colour indices. Our observations did not reveal the presence of significant correlated spectral variability in these targets on short timescales. Variability studies of larger blazar samples on minutes to years timescales are extremely important since they can provide information on numerous blazar parameters.

Chapter 6

Summary and Future Plan

6.1 Summary

In this dissertation work, we have analysed the long term multi-band (X-ray, UV and optical) observations archival data of the TeV blazar PKS 2155–304 and ground based multi-band optical data of three TeV blazars (PKS 1510–89, PG 1553+113 and Mrk 501). We have studied the following:

1. Long term spectral energy distribution (SED) study of the blazar PKS 2155–304.
2. Study the X-ray spectral behaviour of the blazar PKS 2155–304 on IDV timescale
3. Studies of variability timescales in X-ray, UV and optical bands of TeV blazars.

The summary of the dissertation work is summarized as below :

6.1.1 Long Term SED of the Blazar PKS 2155–304

We have used 20 archival XMM-Newton observations of the TeV blazar PKS 2155–304 in simultaneous X-ray, UV and optical bands to study the long term flux and SED behaviour. We used optical/UV and X-ray data to construct SEDs that span more than three orders of magnitude in frequency and we fitted them with a log-parabolic

model; such model has been applied many times in the past for this, and several other blazars. These fits were poor and so we also examined combined power-law and log-parabolic model to fit the SEDs and it gives better results. Our results from the SEDs fitting of all the observations can be summarized as follows:

- The turn-over frequency correlates *positively* with the model spectral slope, and with the curvature parameter, b . As the turn-over energy increases, the spectra steepens, and the curvature parameter increases.
- Due to the above mentioned correlations, the peak frequency, ν_p and the curvature parameter b are also positively correlated. As ν_p shifts to higher energies, the spectral curvature also increases following the relation: $b \propto \sqrt{\nu_p}$.
- We do not observe a strong correlation between the peak power, S_p , and the peak frequency, ν_p . If there is a relation between these two parameters, it is most probably an anti-correlation, in the sense that as the peak luminosity decreases, the peak frequency shifts to higher energies, roughly according to the relation: $S_p \propto 1/\nu_p$.
- Our long term SEDs fitting results suggest that the optical/UV and X-ray emission in this source may be due to the emission from different lepton populations.

6.1.2 Study X-ray Spectral behaviour of the Blazar PKS 2155–304 on IDV Timescale

We have analysed *XMM-Newton* three nearly continuous observations of the blazar, PKS 2155–304, made on 24 May 2002 in the 0.3 – 10 keV X-ray band. These observations display a mini-flare, a nearly constant flux period and a strong flux increase. We performed a time-resolved spectral study of the data, by dividing the data into eight segments. We fitted the data with a power-law and a broken power-law model, and in some of the segments we found a noticeable spectral flattening of the source’s spectrum below 10 keV. We also performed “time-resolved” cross-correlation analyses. The results come out from the X-ray spectral analysis are summarized below :

- We have found that the spectral slope is anti-correlated with flux i.e the spectra “harden” with increasing flux. The value of correlation coefficient is -0.95 which is significantly better than 99% confidence level ($P_{null}=3.0\times 10^{-4}$).
- We have detected the significant hard and soft lags (*for the first time in a single observation of this source*) during the first and the last part of the observation, respectively. This result implies that the difference between particle acceleration time (t_{acc}) and particle cooling time (t_{cool}) of the emitting electrons is changing from epoch to epoch, which is in agreement with the past studies. The lags between the harder and softer X-ray bands indicate that both the particle acceleration and synchrotron cooling processes make an important contribution to the emission from this TeV blazar.

6.1.3 Studies of Variability Timescales in X-ray, UV and Optical Bands

We have analysed multi-band optical variability of three TeV blazars (PKS 1510–089, PG 1553+113 and Mrk 501) and multi-band (optical/UV and X-ray) variability of the blazar PKS 2155–304 on diverse timescales which are useful in understanding the emission mechanisms of the blazars. Our optical photometric observations of three TeV blazars: PKS 1510-089, PG 1553+113 and Mrk 501 were taken using two telescopes in India, one in Bulgaria, one in Greece and one in Serbia during June 2012 - September 2014. These observations covered a total of 95 nights with a total of 202 B filter frames, 247 in V band, 817 in R band while 229 images were taken in the I filter. We have used XMM-Newton archival data during 2000–2012 for simultaneous multi-wavelength variability study of the blazar PKS 2155–304. The main results of the analysis are summarized below:

- We have found that all blazars are active in over entire period of observation.
- We searched for flux and colour variability on few months to few year timescales and found significant flux variations on these timescales with moderate colour variations for all three TeV blazars observed in optical band.

- We also studied the correlation between the V magnitude of the source and corresponding variations in the (B-I), (B-V), (R-I), and (V-R) colour indices. Our observations did not reveal the presence of significant correlated spectral variability in these targets on short timescales. Variability studies of larger blazar samples on minutes to years timescales are extremely important since they can provide information on numerous blazar parameters.
- Simultaneous multi-wavelength (X-ray, UV and optical) study of the blazar PKS 2155–304 has shown that the source is variable in all bands on timescales of years. The amplitude of the root mean square (rms) variability is of order of $\sim 35\text{--}45\%$ at all bands. We did not observe any extreme activity taking place during these observations. The variability amplitude slightly increases from soft (0.6-2 keV) to the hard (2-10 keV) X-ray band, and decreases from the optical to the UV bands.

6.2 Future Plans

Simultaneous multi-wavelength observations of blazars in entire EM band spectrum for a longer span of time is required to understand the physical processes which are responsible for blazar emission. The cross-correlation analysis between the simultaneous multi-band observations is a strong diagnostic tool which help us to understand the origin of different emission mechanisms in various energy bands. A large number of ground and space (XMM-Newton, Chandra, Kepler, Swift, Maxi, HST, Fermi, INTEGRAL, NuSTAR, ASTROSAT, ASTRO-H, etc.) based observatories are available which jointly cover the whole EM band. With the use of all these available observing facilities with proper planning, we can perform the following studies :

- We can study the spectral energy distributions SEDs properties in a sample of HBLs and LBLs. On the basis of this analysis we can try to explain which emission mechanism is dominated in which class of blazars.
- Using multi-wavelength data, we can perform cross-correlation between high energy (γ -ray, X-ray) bands and low energy (radio, IR, Optical, UV) bands to

predict whether synchrotron photons produced from relativistic electrons and are up-scattered by synchrotron self Compton (SSC) or External Compton (EC) mechanism to higher (GeV/TeV) energy bands. Multi-band correlation analysis is a strong tool which provide the facility to understand the root cause behind the origin of emission mechanism in various EM bands.

- X-ray spectral analysis is a strong diagnostic tool which provide information about the processes (e.g. particle acceleration, synchrotron cooling) which one is dominated in a particular observation of TeV Blazar. We can study the long term X-ray spectral variability of TeV Blazars like PKS 2155–304 and Mrk 421.

Bibliography

- Abdo, A. A., et al. 2010, ApJ, 716, 30
- Agarwal, A., & Gupta, A. C. 2015, MNRAS, 450, 541
- Agarwal, A., et al. 2015, MNRAS, 451, 3882
- Agarwal, A., et al. 2016, MNRAS, 455, 680
- Aharonian, F., et al. 2009a, A&A, 502, 749
- Aharonian, F., et al. 2009b, ApJL, 696, L150
- Aharonian, F., et al. 2006, A&A, 448, L43
- Aharonian, F., et al. 2005, A&A, 442, 895
- Albert, J., et al. 2007a, ApJL, 654, L119
- Albert, J., et al. 2007b, ApJ, 669, 1143
- Aschenbach, B. 2002, in Society of Photo-Optical Instrumentation Engineers (SPIE) Conference Series, Vol. 4496, X-Ray Optics for Astronomy: Telescopes, Multilayers, Spectrometers, and Missions, ed. P. Gorenstein & R. B. Hoover, 8
- Baring, M. G., Ellison, D. C., Reynolds, S. P., Grenier, I. A., & Goret, P. 1999, ApJ, 513, 311
- Barkov, M. V., Aharonian, F. A., Bogovalov, S. V., Kelner, S. R., & Khangulyan, D. 2012, ApJ, 749, 119
- Bednarz, J., & Ostrowski, M. 1998, Physical Review Letters, 80, 3911

- Begelman, M. C., Fabian, A. C., & Rees, M. J. 2008, *MNRAS*, 384, L19
- Bell, A. R. 1978, *MNRAS*, 182, 147
- Bessell, M. S., Castelli, F., & Plez, B. 1998, *A&A*, 333, 231
- Bhagwan, J., Gupta, A. C., Papadakis, I. E., & Wiita, P. J. 2014, *MNRAS*, 444, 3647
- Bhagwan, J., Gupta, A. C., Papadakis, I. E., & Wiita, P. J. 2016, *New Astronomy*, 44, 21
- Blandford, R. D. 1990, in *Active Galactic Nuclei*, ed. R. D. Blandford, H. Netzer, L. Woltjer, T. J.-L. Courvoisier, & M. Mayor, 161
- Blandford, R. D., & Königl, A. 1979, *ApJ*, 232, 34
- Blandford, R. D., & Rees, M. J. 1978, in *BL Lac Objects*, ed. A. M. Wolfe, 328
- Błażejowski, M., Sikora, M., Moderski, R., & Madejski, G. M. 2000, *ApJ*, 545, 107
- Böttcher, M. 2007, *Ap&SS*, 309, 95
- Böttcher, M., & Bloom, S. D. 2000, *AJ*, 119, 469
- Brinkmann, W., et al. 1994, *A&A*, 288
- Brinkmann, W., Papadakis, I. E., Raeth, C., Mimica, P., & Haberl, F. 2005, *A&A*, 443, 397
- Calafut, V., & Wiita, P. J. 2015, *Journal of Astrophysics and Astronomy*, 36, 255
- Camenzind, M., & Krockenberger, M. 1992, *A&A*, 255, 59
- Cardelli, J. A., Clayton, G. C., & Mathis, J. S. 1989, *ApJ*, 345, 245
- Carini, M. T. 1990, Ph.D. thesis, George State University, Atlanta, USA, (1990)
- Carini, M. T., & Miller, H. R. 1992, *ApJ*, 385, 146
- Carini, M. T., Noble, J. C., Taylor, R., & Culler, R. 2007, *AJ*, 133, 303

- Cerruti, M., Zech, A., Boisson, C., & Inoue, S. 2012, in American Institute of Physics Conference Series, Vol. 1505, American Institute of Physics Conference Series, ed. F. A. Aharonian, W. Hofmann, & F. M. Rieger, 635
- Chadwick, P. M., et al. 1999, *ApJ*, 513, 161
- Ciprini, S., Tosti, G., Raiteri, C. M., Villata, M., Ibrahimov, M. A., Nucciarelli, G., & Lanteri, L. 2003, *A&A*, 400, 487
- Courvoisier, T. J.-L., et al. 1995, *ApJ*, 438, 108
- Dai, B. Z., Xie, G. Z., Li, K. H., Zhou, S. B., Liu, W. W., & Jiang, Z. J. 2001, *AJ*, 122, 2901
- D'Ammando, F., et al. 2009, *A&A*, 508, 181
- D'Ammando, F., et al. 2011, *A&A*, 529, A145
- Danforth, C. W., Keeney, B. A., Stocke, J. T., Shull, J. M., & Yao, Y. 2010, *ApJ*, 720, 976
- de Chambure, D., Lainé, R., van Katwijk, K., & Kletzkine, P. 1999, *ESA Bulletin*, 100, 30
- Dermer, C. D., & Schlickeiser, R. 1993, *ApJ*, 416, 458
- Dickey, J. M., & Lockman, F. J. 1990, *ARA&A*, 28, 215
- Dolcini, A., et al. 2007, *A&A*, 469, 503
- Dominici, T. P., Abraham, Z., & Galo, A. L. 2006, *A&A*, 460, 665
- Donato, D., Sambruna, R. M., & Gliozzi, M. 2005, *A&A*, 433, 1163
- Edelson, R., et al. 1995, *ApJ*, 438, 120
- Edelson, R., Turner, T. J., Pounds, K., Vaughan, S., Markowitz, A., Marshall, H., Dobbie, P., & Warwick, R. 2002, *ApJ*, 568, 610
- Edelson, R. A., Krolik, J. H., & Pike, G. F. 1990, *ApJ*, 359, 86

- Ellison, D. C., & Double, G. P. 2004, *Astroparticle Physics*, 22, 323
- Falomo, R., Pesce, J. E., & Treves, A. 1993, *ApJL*, 411, L63
- Falomo, R., Scarpa, R., & Bersanelli, M. 1994, *ApJS*, 93, 125
- Falomo, R., & Treves, A. 1990, *Publications of the ASP*, 102, 1120
- Fan, J. H., & Lin, R. G. 1999, *ApJS*, 121, 131
- Fanaroff, B. L., & Riley, J. M. 1974, *MNRAS*, 167, 31P
- Fiorucci, M., Ciprini, S., & Tosti, G. 2004, *A&A*, 419, 25
- Fordham, J. L. A., Bone, D. A., Oldfield, M. K., Bellis, J. G., & Norton, T. J. 1992, in *ESA Special Publication, Vol. 356, Photon Detectors for Space Instrumentation*, ed. T. D. Guyenne & J. Hunt
- Foschini, L., et al. 2006, *A&A*, 453, 829
- Fossati, G., Maraschi, L., Celotti, A., Comastri, A., & Ghisellini, G. 1998, *MNRAS*, 299, 433
- Fukugita, M., Shimasaku, K., & Ichikawa, T. 1995, *Publications of the ASP*, 107, 945
- Gaur, H., Gupta, A. C., Lachowicz, P., & Wiita, P. J. 2010, *ApJ*, 718, 279
- Gaur, H., Gupta, A. C., & Wiita, P. J. 2012, *AJ*, 143, 23
- Georganopoulos, M., & Kazanas, D. 2003, *ApJL*, 594, L27
- George, I. M., Warwick, R. S., & Bromage, G. E. 1988, *MNRAS*, 232, 793
- Ghisellini, G., & Madau, P. 1996, *MNRAS*, 280, 67
- Ghisellini, G., Tavecchio, F., Foschini, L., Ghirlanda, G., Maraschi, L., & Celotti, A. 2010, *MNRAS*, 402, 497
- Ghisellini, G., et al. 1997, *A&A*, 327, 61
- Ghosh, K. K., Ramsey, B. D., Sadun, A. C., & Soundararajaperumal, S. 2000, *ApJS*, 127, 11

- Giommi, P., Barr, P., Pollock, A. M. T., Garilli, B., & Maccagni, D. 1990, *ApJ*, 356, 432
- Giommi, P., Capalbi, M., Fiocchi, M., Memola, E., Perri, M., Piranomonte, S., Rebecchi, S., & Massaro, E. 2002, in *Blazar Astrophysics with BeppoSAX and Other Observatories*, ed. P. Giommi, E. Massaro, & G. Palumbo, 63
- Giozzi, M., Sambruna, R. M., Jung, I., Krawczynski, H., Horan, D., & Tavecchio, F. 2006, *ApJ*, 646, 61
- Gopal-Krishna, Stalin, C. S., Sagar, R., & Wiita, P. J. 2003, *ApJL*, 586, L25
- Green, R. F., Schmidt, M., & Liebert, J. 1986, *ApJS*, 61, 305
- Gupta, A. C., et al. 2016, *MNRAS*
- Gupta, A. C., Banerjee, D. P. K., Ashok, N. M., & Joshi, U. C. 2004, *A&A*, 422, 505
- Gupta, A. C., Deng, W. G., Joshi, U. C., Bai, J. M., & Lee, M. G. 2008, *New Astronomy*, 13, 375
- Gupta, A. C., & Joshi, U. C. 2005, *A&A*, 440, 855
- Hartman, R. C., et al. 1992, *ApJL*, 385, L1
- Hartman, R. C., et al. 2001, *ApJ*, 553, 683
- Hayashida, M., et al. 2015, *ApJ*, 807, 79
- Heidt, J., & Wagner, S. J. 1996, *A&A*, 305, 42
- H.E.S.S. Collaboration, et al. 2012, *A&A*, 539, A149
- Hewitt, A., & Burbidge, G. 1980, *ApJS*, 43, 57
- Holder, J. 2012, *Astroparticle Physics*, 39, 61
- Holder, J. 2014, *Brazilian Journal of Physics*, 44, 450
- Hovatta, T., Valtaoja, E., Tornikoski, M., & Lähteenmäki, A. 2009, *A&A*, 494, 527
- Hughes, P. A., Aller, M. F., & Aller, H. D. 2011, *ApJ*, 735, 81

- Isobe, T., Feigelson, E. D., Akritas, M. G., & Babu, G. J. 1990, *ApJ*, 364, 104
- Jannuzi, B. T., Smith, P. S., & Elston, R. 1994, *ApJ*, 428, 130
- Jansen, F., et al. 2001, *A&A*, 365, L1
- Kapanadze, B., Romano, P., Vercellone, S., & Kapanadze, S. 2014, *MNRAS*, 444, 1077
- Kapanadze, B. Z. 2013, *AJ*, 145, 31
- Kardashev, N. S., Kuz'min, A. D., & Syrovatskii, S. I. 1962, , 6, 167
- Kastendieck, M. A., Ashley, M. C. B., & Horns, D. 2011, *A&A*, 531, A123
- Kataoka, J., et al. 1999, *ApJ*, 514, 138
- Kataoka, J., Takahashi, T., Makino, F., Inoue, S., Madejski, G. M., Tashiro, M., Urry, C. M., & Kubo, H. 2000, *ApJ*, 528, 243
- Katarzyński, K., Ghisellini, G., Tavecchio, F., Maraschi, L., Fossati, G., & Mastichiadis, A. 2005, *A&A*, 433, 479
- Kato, S., & Fukue, J. 1980, *PASJ*, 32, 377
- Kirk, J. G., Guthmann, A. W., Gallant, Y. A., & Achterberg, A. 2000, *ApJ*, 542, 235
- Kirk, J. G., Rieger, F. M., & Mastichiadis, A. 1998, *A&A*, 333, 452
- Kirk, R. L., et al. 1998, in *Lunar and Planetary Science Conference*, Vol. 29, *Lunar and Planetary Science Conference*
- Kohmura, Y., Makishima, K., Tashiro, M., Ohashi, T., & Urry, C. M. 1994, *PASJ*, 46, 131
- Konigl, A. 1981, *ApJ*, 243, 700
- Krawczynski, H. 2004, *New Astronomy Review*, 48, 367
- Krawczynski, H., et al. 2004, *ApJ*, 601, 151
- Krennrich, F., et al. 1999, *ApJ*, 511, 149

- Krishan, V., & Wiita, P. J. 1994, *ApJ*, 423, 172
- Lachowicz, P., Gupta, A. C., Gaur, H., & Wiita, P. J. 2009, *A&A*, 506, L17
- Landau, R., et al. 1986, *ApJ*, 308, 78
- Levinson, A. 2007, *ApJL*, 671, L29
- Liller, M. H., & Liller, W. 1975, *ApJL*, 199, L133
- Lu, P. K. 1972, *AJ*, 77, 829
- Malkan, M. A., & Moore, R. L. 1986, *ApJ*, 300, 216
- Malkan, M. A., & Sargent, W. L. W. 1982, *ApJ*, 254, 22
- Mangalam, A. V., & Wiita, P. J. 1993, *ApJ*, 406, 420
- Marcha, M. J. M., Browne, I. W. A., Impey, C. D., & Smith, P. S. 1996, *MNRAS*, 281, 425
- Marscher, A. P. 1980, *ApJ*, 235, 386
- Marscher, A. P. 1996, in *Astronomical Society of the Pacific Conference Series*, Vol. 110, *Blazar Continuum Variability*, ed. H. R. Miller, J. R. Webb, & J. C. Noble, 248
- Marscher, A. P. 2009, *ArXiv e-prints*
- Marscher, A. P. 2014, *ApJ*, 780, 87
- Marscher, A. P., & Gear, W. K. 1985, *ApJ*, 298, 114
- Marshall, H. L., Urry, C. M., Sambruna, R. M., & Pesce, J. E. 2001, *ApJ*, 549, 938
- Mason, K. O., et al. 2001, *A&A*, 365, L36
- Massaro, E., Perri, M., Giommi, P., & Nesci, R. 2004, *A&A*, 413, 489
- Massaro, E., Tramacere, A., Perri, M., Giommi, P., & Tosti, G. 2006, *A&A*, 448, 861
- Massaro, F., Tramacere, A., Cavaliere, A., Perri, M., & Giommi, P. 2008, *A&A*, 478, 395

- Mastichiadis, A., & Kirk, J. G. 2002, *Publications of the Astron. Soc. of Australia*, 19, 138
- Miller, H. R., Carini, M. T., Gaston, B. J., & Hutter, D. J. 1988, in *ESA Special Publication*, Vol. 281, *ESA Special Publication*
- Miller, H. R., Carini, M. T., & Goodrich, B. D. 1989, *Nature*, 337, 627
- Miller, H. R., & Green, R. F. 1983, in , Vol. 15, *Bulletin of the American Astronomical Society*, 957
- Miller, L., Peacock, J. A., & Mead, A. R. G. 1990, *MNRAS*, 244, 207
- Mimica, P., Aloy, M. A., Müller, E., & Brinkmann, W. 2005, *A&A*, 441, 103
- Morini, M., Chiappetti, L., Maccagni, D., Maraschi, L., Molteni, D., Tanzi, E. G., Treves, A., & Wolter, A. 1986, *ApJL*, 306, L71
- Mücke, A., Protheroe, R. J., Engel, R., Rachen, J. P., & Stanev, T. 2003, *Astroparticle Physics*, 18, 593
- Mukherjee, R., et al. 1999, *ApJ*, 527, 132
- Nalewajko, K., Giannios, D., Begelman, M. C., Uzdensky, D. A., & Sikora, M. 2011, *MNRAS*, 413, 333
- Nandra, K., George, I. M., Mushotzky, R. F., Turner, T. J., & Yaqoob, T. 1997, *ApJ*, 476, 70
- Nilsson, K., Pasanen, M., Takalo, L. O., Lindfors, E., Berdyugin, A., Ciprini, S., & Pforr, J. 2007, *A&A*, 475, 199
- Nowak, M. A., & Wagoner, R. V. 1992, *ApJ*, 393, 697
- Osterman, M. A., et al. 2006, *AJ*, 132, 873
- Perlman, E. S., et al. 2005, *ApJ*, 625, 727
- Pesce, J. E., et al. 1997, *ApJ*, 486, 770
- Petry, D., et al. 2000, *ApJ*, 536, 742

- Pian, E., & Treves, A. 1993, *ApJ*, 416, 130
- Pian, E., et al. 1997, *ApJ*, 486, 784
- Piner, B. G., Pant, N., & Edwards, P. G. 2008, *ApJ*, 678, 64
- Raino', S., Cavazzuti, E., Colafrancesco, S., Giommi, P., Tramacere, A., & the Fermi-LAT Collaboration. 2009, ArXiv e-prints
- Raiteri, C. M., et al. 2003, *A&A*, 402, 151
- Rani, B., et al. 2011, *MNRAS*, 417, 1881
- Rector, T. A., Gabuzda, D. C., & Stocke, J. T. 2003, *AJ*, 125, 1060
- Rodríguez-Pascual, P. M., et al. 1997, *ApJS*, 110, 9
- Romero, G. E., Cellone, S. A., & Combi, J. A. 1999, *Astronomy and Astrophysics, Supplement*, 135, 477
- Roming, P. W. A., et al. 2009, *ApJ*, 690, 163
- Sagar, R., et al. 2011, *Current Science*, 101, 1020
- Sakamoto, Y., et al. 2008, *ApJ*, 676, 113
- Sambruna, R. M., et al. 2000, *ApJ*, 538, 127
- Sambruna, R. M., Barr, P., Giommi, P., Maraschi, L., Tagliaferri, G., & Treves, A. 1994, *ApJ*, 434, 468
- Sasada, M., et al. 2010, *PASJ*, 62, 645
- Schlafly, E. F., & Finkbeiner, D. P. 2011, *ApJ*, 737, 103
- Schlegel, D. J., Finkbeiner, D. P., & Davis, M. 1998, *ApJ*, 500, 525
- Schwadron, N. A., Lee, M. A., & McComas, D. J. 2008, *ApJ*, 675, 1584
- Schwartz, D. A., Griffiths, R. E., Schwarz, J., Doxsey, R. E., & Johnston, M. D. 1979, *ApJL*, 229, L53

- Sembay, S., Warwick, R. S., Urry, C. M., Sokoloski, J., George, I. M., Makino, F., Ohashi, T., & Tashiro, M. 1993, *ApJ*, 404, 112
- Seyfert, C. K. 1943, *ApJ*, 97, 28
- Shakura, N. I., & Sunyaev, R. A. 1973, *A&A*, 24, 337
- Shimmins, A. J., & Bolton, J. G. 1974, *Australian Journal of Physics Astrophysical Supplement*, 32, 1
- Sikora, M. 1994, *ApJS*, 90, 923
- Spada, M., Ghisellini, G., Lazzati, D., & Celotti, A. 2001, *MNRAS*, 325, 1559
- Stetson, P. B. 1987, *Publications of the ASP*, 99, 191
- Stetson, P. B. 1992, in *Astronomical Society of the Pacific Conference Series*, Vol. 25, *Astronomical Data Analysis Software and Systems I*, ed. D. M. Worrall, C. Biemesderfer, & J. Barnes, 297
- Stocke, J. T., Morris, S. L., Gioia, I. M., Maccacaro, T., Schild, R., Wolter, A., Fleming, T. A., & Henry, J. P. 1991, *ApJS*, 76, 813
- Strüder, L., et al. 2001, *A&A*, 365, L18
- Sun, Y.-H., Wang, J.-X., Chen, X.-Y., & Zheng, Z.-Y. 2014, *ApJ*, 792, 54
- Thompson, D. J., Djorgovski, S., & de Carvalho, R. 1990, *Publications of the ASP*, 102, 1235
- Tramacere, A., et al. 2007, *A&A*, 467, 501
- Tramacere, A., Giommi, P., Perri, M., Verrecchia, F., & Tosti, G. 2009, *A&A*, 501, 879
- Tramacere, A., Massaro, E., & Taylor, A. M. 2011, *ApJ*, 739, 66
- Urry, C. M., et al. 1993, *ApJ*, 411, 614
- Urry, C. M., & Padovani, P. 1995, *Publications of the ASP*, 107, 803
- Urry, C. M., et al. 1997, *ApJ*, 486, 799

- Vaughan, S., Edelson, R., Warwick, R. S., & Uttley, P. 2003, MNRAS, 345, 1271
- Villata, M., & Raiteri, C. M. 1999, A&A, 347, 30
- Villata, M., et al. 2004, A&A, 421, 103
- Wagner, S. J., & Witzel, A. 1995, ARA&A, 33, 163
- Xie, G. Z., Li, K. H., Bai, J. M., Dai, B. Z., Liu, W. W., Zhang, X., & Xing, S. Y. 2001, ApJ, 548, 200
- Xie, G. Z., Zhou, S. B., Dai, B. Z., Liang, E. W., Li, K. H., Bai, J. M., Xing, S. Y., & Liu, W. W. 2002, MNRAS, 329, 689
- Xue, Y., & Cui, W. 2005, ApJ, 622, 160
- Zhang, X.-H., & Bao, G. 1991, A&A, 246, 21
- Zhang, Y. H. 2002, MNRAS, 337, 609
- Zhang, Y. H. 2008, ApJ, 682, 789
- Zhang, Y. H., Bai, J. M., Zhang, S. N., Treves, A., Maraschi, L., & Celotti, A. 2006a, ApJ, 651, 782
- Zhang, Y. H., et al. 2002, ApJ, 572, 762
- Zhang, Y. H., Treves, A., Celotti, A., Qin, Y. P., & Bai, J. M. 2005, ApJ, 629, 686
- Zhang, Y. H., Treves, A., Maraschi, L., Bai, J. M., & Liu, F. K. 2006b, ApJ, 637, 699